Stellar Multiplicity Statistics in APOGEE

by

Christine Mazzola Daher

B.S. Mississippi State University, 2016

M.S. University of Pittsburgh, 2018

Submitted to the Graduate Faculty of

The Dietrich School of Arts and Sciences

in partial fulfillment

of the requirements for the degree of

Doctor of Philosophy

University of Pittsburgh

2022

UNIVERSITY OF PITTSBURGH

DIETRICH SCHOOL OF ARTS AND SCIENCES

This dissertation was presented

by

Christine Mazzola Daher

It was defended on

May 6th 2022

and approved by

Carles Badenes, Department of Physics and Astronomy

Brian Batell, Department of Physics and Astronomy

Peter Freeman, Department of Statistics and Data Science, Carnegie Mellon University

Jeffrey Newman, Department of Physics and Astronomy

Andrew Zentner, Department of Physics and Astronomy

Dissertation Director: Carles Badenes, Department of Physics and Astronomy

Stellar Multiplicity Statistics in APOGEE

Christine Mazzola Daher, PhD

University of Pittsburgh, 2022

Nearly every area of astrophysics is impacted by our knowledge of stellar multiplicity, though perhaps none more so than the life cycles of the stars within close binaries. This dissertation seeks to characterize these effects through statistical analyses of stellar parameters and multi-epoch radial velocities (RV) determined from the high-resolution spectra of the Apache Point Observatory Galactic Evolution Experiment (APOGEE). Given that the majority of APOGEE's stars have sparsely-sampled RV curves, we utilize the maximum shift in the radial velocities, $\Delta\mathrm{RV}_{\mathrm{max}}$, as an indicator for RV variability and the fraction of RV variable systems as a proxy for the close binary fraction.

First, we select a sample of 41 363 dwarf and subgiant stars from APOGEE data release 14 and explore the observed trends across a variety of stellar parameters before focusing on the discovery of a complex anticorrelation between the close binary fraction and Fe, overall α, O, Mg, and Si abundances. The steeper trends between α-process abundances as compared to Fe indicate that dust and ices within protostellar discs are largely responsible for the disks' opacity and likelihood of fragmentation.

Second, we define a sample of 24 496 dwarfs and 2786 giants from APOGEE data release 14 with projected rotation speeds $v \sin i$ determined by our pipeline and ages, distances, and masses taken from the Sanders et al. 2018 catalog. We demonstrate that rapid stellar rotation is overwhelmingly associated with close binaries and that rotation in close binaries diverges significantly from the predictions of gyrochronolgy.

Finally, we expose further insights into low-mass binary formation by separately analyzing samples of G, K, and M dwarfs taken from APOGEE data release 17. Through an analysis of the cumulative distributions of [Fe/H], [M/H], and [α/H], we find that correlations between stellar abundances and the close binary fraction depend on spectral type. These preliminary results suggest that the metallicity-dependent protostellar disc fragmentation crucial to forming K dwarf primaries is less important than mass-dependent disc fragmen-

tation for G dwarf primaries, and that M dwarf binary formation may be more sensitive to disc cooling promoted by gas enriched with dust and icy grains.

Table of Contents

List of Tables

List of Figures

Preface

Completing a Ph.D. has been my childhood dream and now a reality thanks to the tireless support of my amazing family, friends, and colleagues. The greatest thanks goes to Carles Badenes for his endless patience, guidance, enthusiasm, and confidence in my work as my dissertation advisor. Valuable guidance and research suggestions came from the members of my committee: Brian Batell, Peter Freeman, Jeffrey Newman, and Andrew Zentner. I also want to thank Leyla Hirschfeld, Brandi McClain, and the rest of the Pitt astronomy faculty for supporting graduate students during their time at Pitt and preparing them to succeed in their future endeavors.

Collaboration with experts representing most sub-fields of astronomy has been crucial to the scientific discoveries presented in this dissertation. I would like to especially thank Maxwell Moe, Kaitlin Kratter, Sergey Koposov, and Matthew Walker for their invaluable insight and suggestions across my various projects. For the chapter on rotation, thank you especially to Jamie Tayar and Marc Pinsonneault for making that work possible and contributing to the interpretations. To the members of the APOGEE collaboration and RV variability subgroup, especially those who appear as coauthors on my publications, thank you for making my science possible and improving it with your helpful feedback.

Collaboration with fellow graduate students has been a highlight of my time here at Pitt. To Héctor Martinez-Rodriguez, thank you so much for welcoming me into the department and providing excellent advice as my graduate student mentor and close friend. To Brian Flores, thank you for helping me better understand stellar spectral templates, a foundational topic to all the science I do, and for always bringing a smile and quick joke. To Troy Raen and Daniel Perrefort, thank you for including me in the LSST Broker project, which helped broaden my scientific interests. Thank you to Yang Ma, Xinyi Wu, Aditi Nethwewala, Namitha James, and Nafis Karim for the fun conversations and funny memories of my first year of graduate school. To Héctor, Brian, Biprateep Dey, Yasha Kaushal, Jared Hand, and Lorena Menzini, thank you for all the wonderful memories of the wacky antics I faced as DM on our D&D nights. As for the Badenes research group, to Sumit Sarbadhicary and Héctor,

thank you for your helpful guidance as I started my research journey; to Juntong Su, Travis Court, Tori Bonidie, and Jakob Bindas, thank you for the helpful comments and camaraderie that make group meetings each week so much fun. Finally, thank you to all of the students, graduate and undergraduate, that I have mentored throughout the years; mentoring you has been one of my proudest and most enjoyable challenges in graduate school. To all listed here, I truly wish you the best in your future endeavors.

Eternal thanks and love is owed to my husband, Jared Daher, for his patience these six long years; his pride in my accomplishments, even introducing my papers to his hospital co-workers; and his support for wherever life and job opportunities take us next. Thanks is also owed to our puppy, Tasha, for both keeping me company and forcing me outside after too many hours at the computer. To my family, I would like to specifically thank my parents, Michael and Janice Mazzola; paternal grandparents, Vince and Jane Mazzola; aunt and uncle, Lynn and Chris Peters; my sisters and brothers-in-law, Alex and Nathan Gaudin and Kelley and Ethan Seal; and mother-in-law, Brenda Daher, for your love and support throughout the years. To the rest of my incredible family and in-laws, though I may be running short on space, rest assured that I am grateful for each and every one of you.

Finally, I would like to remember those who may no longer be here but whose impacts will forever be felt. Levi Prisock, my dear friend from 8th grade to college, you left this world far too soon, but I know you would be both proud and entirely unsurprised to see me complete this Ph.D. Love and thanks also to her mother, Mary Jane Andol, who continues to visit and reminisce with me despite the Levi-sized hole in our hearts. My maternal grandparents, James and Joan Pingatore, may no longer be with us, but I am deeply proud to have graduated from his alma mater, the University of Pittsburgh. Thank you to my mother, father, and maternal grandfather for fostering my love of STEM from a young age; without you, I would have never believed that I was capable of reaching for and revealing new things about the stars.

1.0 Introduction

The mutual gravitational attraction shared between the two stars in a binary star system produces a host of diametric opposites. The elegant dances of these systems can be either (and sometimes both) regular or chaotic; imprisoning or liberating; fatal attraction or the seeds of new life; and so much more. For example, the lonely trek of wide binaries is incredibly regular and unchanging when compared to the chaotic evolution of interacting binaries. Dynamical interactions with third-parties, a very real risk in dense environments such as globular clusters, can alternatively lead to partner exchanges or to the tightening of close binaries. The difficult search for habitability zones endured by circumbinary planets are matched by the wealth of metals left behind after binaries die, thus seeding new star and planetary systems across the galaxy. Stellar multiplicity, the study of these multi-star systems, has itself been regarded as a window into fascinating astrophysical processes or as a nuisance to other astronomical research fields.

Ambivalent to our opinions, the many consequences of binaries ripple onwards throughout most areas of astrophysics (A. Price-Whelan et al. 2019). Naturally, the most direct impacts can be found within stellar astrophysics. Multiplicity statistics are a natural outcome of star and planet formation and thus a probe for formation physics (i.e., Bate 2019; K. Kratter et al. 2016; Moe, Kaitlin M. Kratter, and Badenes 2019), while the occurrence rates and habitability of circumbinary planets are impacted by their host systems (Jaime et al. 2014; Moe and Kaitlin M Kratter 2021). Stellar evolution in binaries can deviate significantly from the evolutionary pathways of single stars for those close enough to interact through mass transfer (Breivik et al. 2020; Paxton, Marchant, et al. 2015). These interacting systems give rise to a diverse array of astrophysical transients, including novae, all Type Ia and many core-collapse supernovae, cataclysmic variables, low- and high-mass X-ray binaries, post-Common Envelope binaries, and most gravitational wave sources that fall in the LIGO and LISA passbands.

Binaries are no less influential on larger scales. Improper treatment of binaries in stellar population synthesis limits our understanding of resolved and unresolved stellar populations,

particularly the processes of galactic reionization (Doughty et al. 2021) and chemical enrichment (Kobayashi et al. 2006) which both rely upon binary-dependent stellar physics. Dynamical measures of dark matter in dwarf galaxies are skewed by the presence of unidentified binaries (Spencer et al. 2017), and systematics from the progenitors of Type Ia supernovae and gravitational-wave mergers limit our constraints on the Hubble constant (e.g. Mortlock et al. 2019).

The preceding paragraphs, simultaneously succinct and jargon-heavy, are hopefully comprehensive enough to convince most astronomers of the universal value presented by better understanding binaries. An even more succinct summary is thus: **stellar multiplicity presents one of the most fundamental and far-reaching domains of astrophysics research**. There remain many questions in stellar multiplicity that require statistical samples of stars to answer, but we are also inundated by publicly-released astronomical data, such that progress is now limited not by the lack of data, but rather by lack of insight – that is, lack of effective strategies to organize diverse and large data sets and extract relevant physical information.

The goal of this Ph.D. dissertation has been to study close binaries through the design and application of such strategies. Before I present the findings of my research, however, let us briefly review some useful background knowledge.

1.1 Orbital Properties of Binaries

In binary systems, the photometrically brighter star is usually referred to as the primary and the fainter star known as the secondary. A useful diagnostic of the binary is the ratio of the secondary mass (m_2) to the primary (m_1), $q = m_2/m_1$. In most cases, the primary is both the brighter and more massive star, leading to $q \leq 1.0$, but in the case where the secondary is a compact companion, then q can exceed one.

The vast majority of close binaries are too far away and their separations too small for the individual stars to be photometrically-resolved, but a variety of methods leveraging different types of data have been used to identify close binaries. Photometric binaries occur

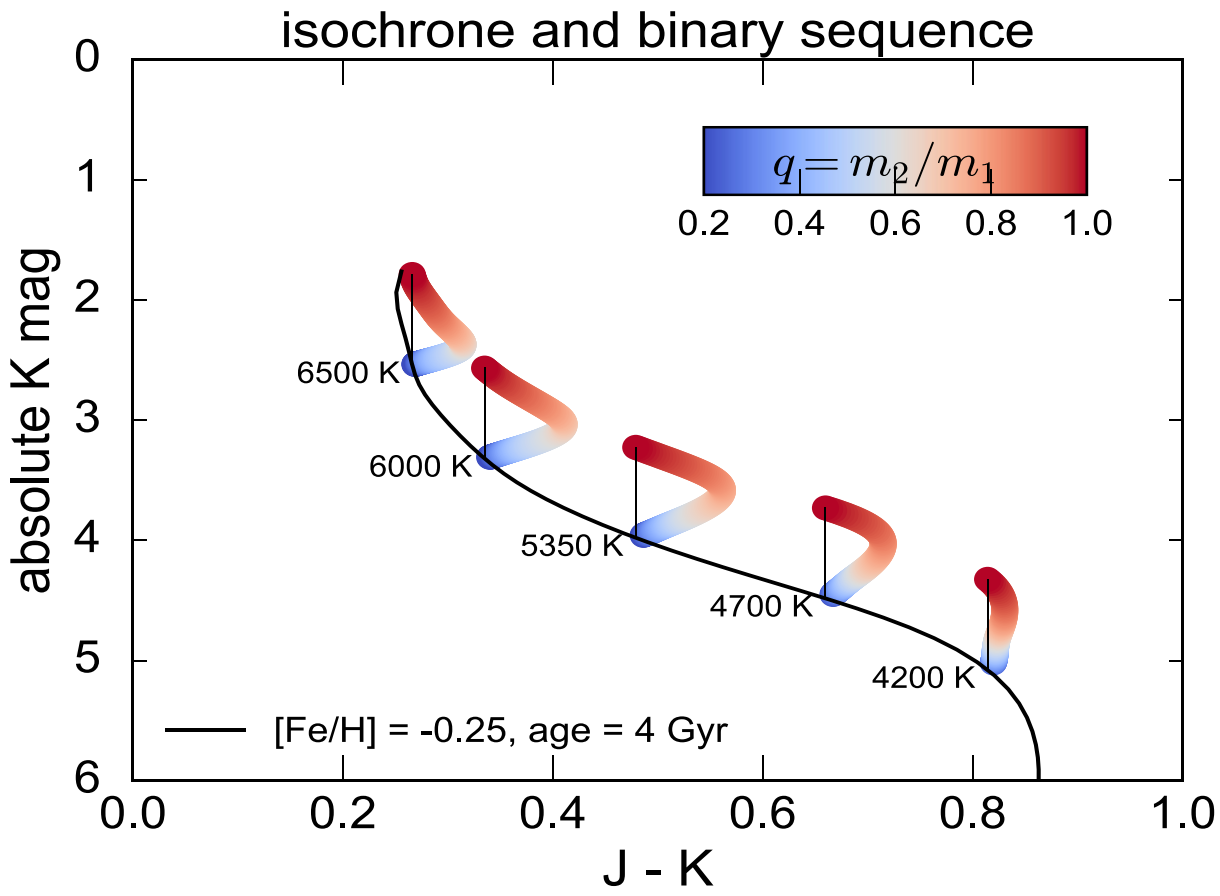

Figure 1: A color-magnitude diagram showing where binaries of a given mass ratio q (colored regions) would appear relative to a MIST isochrone for single stars (black line). Image courtesy of Kareem El-Badry, Ting, et al. 2018, where it is the right panel of Fig. 9.

when the companion has comparable brightness to the primary ($q \gtrsim 0.6$), and because they are brighter than comparable single stars, these systems form a "binary sequence" above the main sequence on Hertzsprung-Russel (HR) and color-magnitude diagrams (CMD), as shown in Fig. 1. Recently, Belokurov et al. 2020 showed that binaries can be identified based on the excess astrometric wobble induced by their orbital motion in *Gaia* DR2 parallaxes. However, spectroscopy remains the best method to probe the short-period systems that are the progenitors of interacting binaries and their resulting astrophysical transients.

Spectroscopic binaries are identified from the periodic Doppler shifts caused by motion directed along our line-of-sight as the binary companions orbit the system's center of mass. Though the redshifts and blueshifts are small, high-resolution spectrographs are easily able to measure them and determine the corresponding velocity. Some literature refers to these as line-of-sight velocities (v_{los}), but the more common term is radial velocity (RV), so named for imagining that the movement is relative to a radius that connects us to the center of mass. Repeat spectra of the binary reveal the periodic variation of the primary's RVs. As an example, consider an equal-mass 1 $M_\odot$ binary; the maximum possible orbital RV amplitude varies from 12 km s^{-1} for a system with an orbital period of 10,000 days ($\approx$ 27 yrs) to as much as 268 km s^{-1} for a period of 1 day.

In many close binaries, only the primary will be bright enough to have distinct spectral line features, producing what are known as single-lined spectroscopic binaries (SB1). A clear example of RV shifts in an SB1 from high-resolution infrared spectra is shown in the top panel of Fig. 2. Like the bottom panel of Fig. 2, however, some systems demonstrate two distinct sets of spectral features and are known as double-lined spectroscopic binaries (SB2). Close binaries form inside the same giant molecular cloud and thus presumably have the same chemical composition, meaning that the secondary is only likely to have distinct spectral lines if it is bright enough to be comparable to the primary. High-q systems are thus oftentimes both photometric binaries and SB2s, with the label depending on the method of identification.

There are a few additional challenges introduced by the enhanced contributions of the secondary. Spectroscopic pipelines usually assume single-star spectral templates, so the secondary's additional light will lead to errors in the measured stellar parameters of both

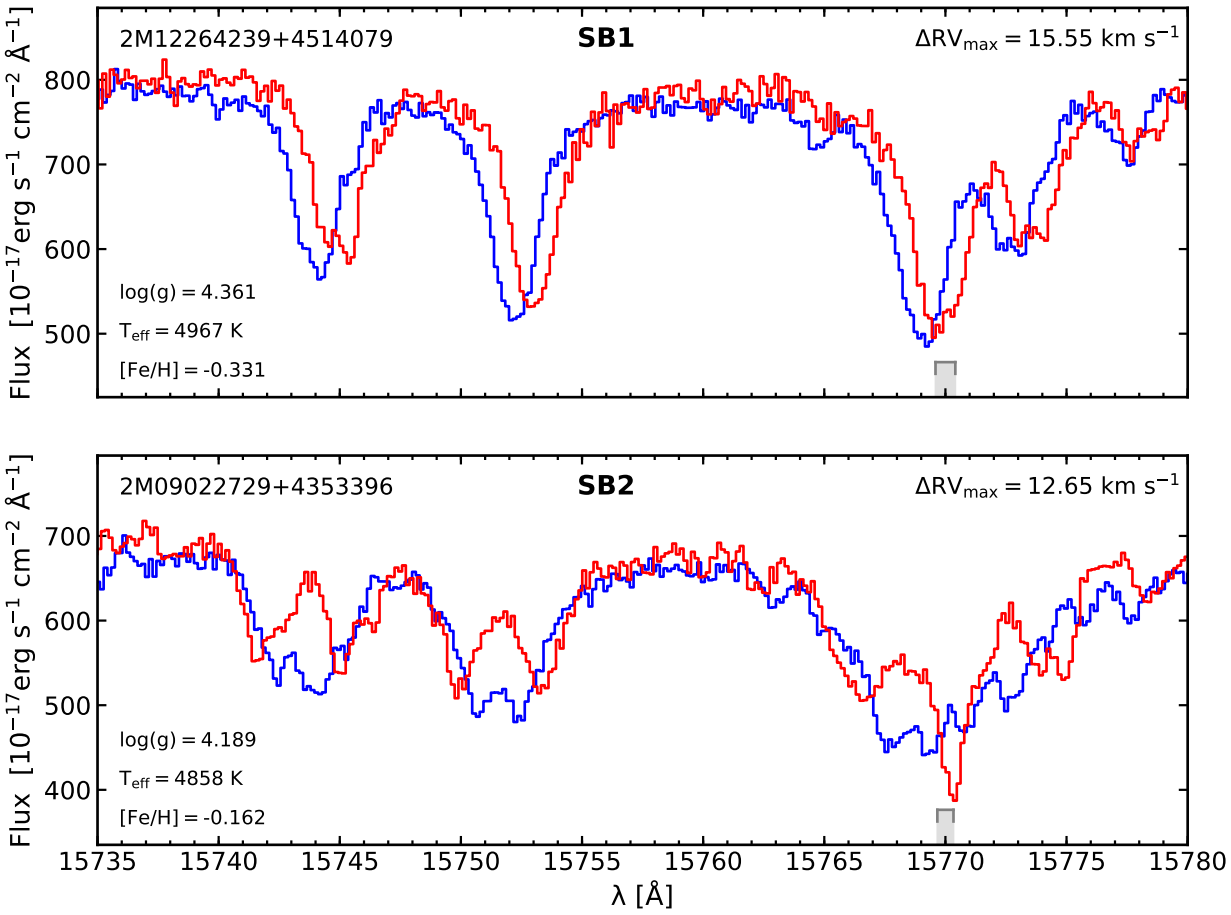

Figure 2: Comparison of visit spectra for two dwarfs with similar mass ($\log(g)$, $T_{\rm eff}$), metallicity [Fe/H], and maximum shift in observed RVs, $\Delta\mathrm{RV_{max}} = |\mathrm{RV_{max}} - \mathrm{RV_{min}}|$. The two panels show the distinction between a binary with only one set of spectral lines (SB1, top panel) and a system with two distinct sets of spectral features (SB2, bottom). To contextualize the expected Doppler shift, the gray ruler at the bottom right in each panel shows the expected shift in wavelength due to each star's $\Delta\mathrm{RV_{max}}$ for a feature centered on $\lambda = 15770$ Å.

photometric binaries and SB2s (K. El-Badry et al. 2018). These pipelines must also choose which spectral feature to use for calculating RVs, which may not correspond to the same star between repeated visits (e.g. Kounkel, K. Covey, et al. 2019; Kounkel, K. R. Covey, et al. 2021). Worse, SB2 spectral lines that overlap across most or all of the visits are difficult to distinguish from line broadening due to intrinsic stellar properties like surface gravity $\log(g)$ or stellar rotation (Simonian, Marc H. Pinsonneault, Terndrup, and Saders 2020). Despite the additional difficulties, there is still a great deal we can learn from comparisons of SB2s and SB1s.

Classifications aside, the RV curves generated from repeat spectroscopy encode information about the extrinsic properties of the binary and the intrinsic properties of the component stars themselves. The RV curve of the primary as a function of time t can be written as

$$\mathrm{RV}_1(t) = K \, \sin i \, (\cos(\nu(t) + \omega) + e \cos \omega \,) \tag{1.1}$$

where e is the orbital eccentricity; K the semi-amplitude; ν the true anomaly, a time-dependent function; i the inclination angle of the orbital plane relative to our line-of-sight; and ω the angle between periapsis[1] and the intersection of the orbital plane and line-of-sight direction, known as the argument of periapsis. From Kepler's Laws, we can write K as

$$K = \frac{2\pi}{\sqrt{1-e^2}} \, \frac{a}{P} \, \frac{q}{1+q} \tag{1.2}$$

where a is the semi-major axis and P is the orbital period.

We can solve for ν through the eccentric anomaly E,

$$\cos \nu = \frac{\cos E - e}{1 - e \cos E} \tag{1.3}$$

except that E is defined as part of a transcendental equation with the mean anomaly M,

$$\begin{aligned} M &= E - e \sin E \\ &= \frac{2\pi}{P} \, (t + s) \end{aligned} \tag{1.4}$$

[1]Note that *periastron* is the point of closest approach between the two companions and is distinct from *periapsis*, the point of closest approach between the primary and the center of mass.

where t is the time of observation and s is a random offset from the time of periapsis. For eccentric orbits, numerical techniques such as the Newton-Raphson method are generally effective at solving for ν at a given time of observation. In the case of a circular orbit, equations 1.3-1.4 simplify to reveal $\nu = M$, causing the RV curve to be a pure sinusoidal function of time.

The traditional approach to characterize stellar multiplicity has been to fit RV curves through a feedback loop of targeted follow-up: each subsequent RV is strategically chosen to tighten the constraints on the orbital parameters until a satisfactory orbital solution is reached. In this fashion, multiplicity surveys have only been able to focus on small samples of a few hundred objects, often in the Solar neighborhood or individual star clusters (e.g., Carney et al. 2003; Duquennoy et al. 1991; Geller, Mathieu, et al. 2008; Matijevič et al. 2011; Raghavan et al. 2010; Sana et al. 2012; with a recent review by Duchêne et al. 2013), though this may become less true in the near future with upcoming data sets such as *Gaia* Data Release 3 significantly increasing the number of binaries with full orbital solutions.

At the time of writing, however, these data sets do not have the statistical power to constrain multiplicity in a complex multivariate space of stellar properties. This is necessary because multiplicity statistics are strong functions of the intrinsic and evolutionary properties of stars, and they are not independent of each other (Moe and Di Stefano 2017). To characterize known trends between stellar multiplicity and properties, discover new ones, and explore their mutual correlations, it is necessary to survey large samples of stars with a wide range of well-calibrated parameters in different dynamical environments.

1.2 Sparsely-Sampled but Still Valuable: the Case for $\Delta\mathbf{RV_{max}}$

Fortunately, the past decades of astronomical surveys have provided a unprecedented treasure trove of publicly-accessible photometric, spectroscopic, and astrometric data. Multiplexed fiber-fed spectrographs have collected large numbers of high resolution spectra of stars within the Milky Way and its dwarf satellites, amassing unique data sets that open a completely new window into stellar multiplicity. Within the fourth installment of the

Sloan Digital Sky Survey (SDSS-IV Blanton et al. 2017; Gunn et al. 2006), the Apache Point Galactic Evolution Experiment (APOGEE, Majewski et al. 2017) survey has collected multi-epoch spectra for hundreds of thousands of stars across every major component of our galaxy using its two high-resolution, multiplexed near-infrared spectrographs located in the northern and southern hemispheres (Wilson et al. 2019). The APOGEE analysis pipelines provide well-calibrated measurements of effective temperatures $T_{\rm eff}$, surface gravities $\log(g)$, detailed chemical abundances, rotation speeds $v \sin i$, and other stellar parameters for each target, which have recently been augmented by the incorporation of parallaxes from *Gaia* (e.g., Sanders et al. 2018). These data sets contain thousands of multiple systems, singled out as SB1s and SB2s from the temporal variation of their RVs.

However, the vast majority of the stars observed by multiplexed spectrographs do not have enough RVs to derive full orbital solutions and will not be prioritized for strategic RV follow-up within the main survey (Badenes, C. Mazzola, et al. 2018; Maoz et al. 2012; A. M. Price-Whelan, Hogg, Rix, Beaton, et al. 2020), as was the traditional approach for stellar multiplicity studies. For example, of the stars in the seventeenth and final data release of APOGEE that pass some basic quality cuts, 76.5% have 3 or fewer good RV measurements. Each individual RV curve may not be particularly informative, but under the right lens, RV curves for hundreds of thousands of stars can provide powerful leverage for exploring stellar multiplicity's dependence on intrinsic and evolutionary stellar parameters and disentangling the parameters' own internal correlations.

Given that so many stars have sparsely-sampled RV curves, we can still identify likely binaries through the maximum shift in each star's RVs, $\Delta\mathrm{RV}_{\rm max} = |\mathrm{RV}_{\rm max} - \mathrm{RV}_{\rm min}|$. We consider a star to be RV variable if its $\Delta\mathrm{RV}_{\rm max}$ exceeds a threshold that is chosen to be significantly larger than the average RV uncertainties. This method has the advantage of only requiring at least two RVs, allowing us to utilize the full size and breadth of the APOGEE samples. Additionally, it enables us to control for the contamination from single stars with large RV uncertainties; we can quickly verify the robustness of our results simply by repeating the analysis with larger or smaller $\Delta\mathrm{RV}_{\rm max}$ thresholds.

The RV variation of very short-period binaries is so dramatic that $\Delta\mathrm{RV}_{\rm max}$ is almost always large even for as few as 2 RVs, including all but the most unfavorable inclinations.

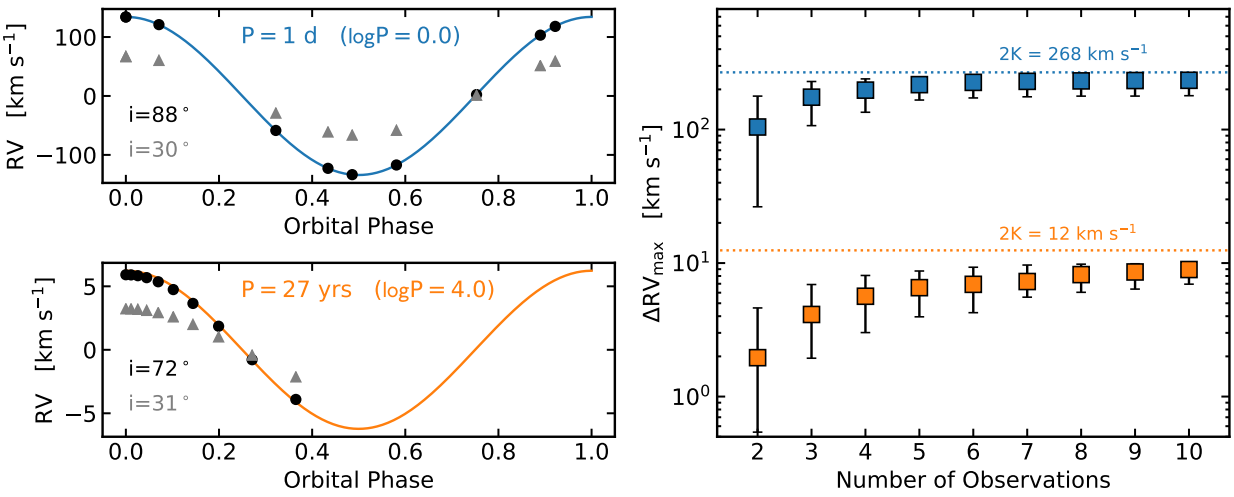

Figure 3: Left panels: Simulated phase-folded RV curves for circular, equal-mass 1 $M_\odot$ close binaries with an extremely short orbital period (P, top) and a longer period (bottom). The solid lines show the theoretical RV curve for a system with an edge-on inclination, i.e. maximum possible RV measurement. The points show simulated observations based on 10 visits logarithmically-evenly-spaced across 10 yrs for a randomly-chosen favorable $\sin i$ (black) and unfavorable (gray). Right: Median calculated $\Delta\mathrm{RV}_{\mathrm{max}}$ values for N_{vis} randomly chosen RVs selected from 10 visits evenly-spaced in log scale across 10 yrs, with upper and lower error bars showing 75% and 25% quantiles respectively. Blue and orange refer to the same periods as the left-hand panels, and the dotted horizontal lines show the maximum possible RV shift (twice the semi-amplitude K).

This becomes less true for systems with longer periods, but the extent of this effect is something we can explore with a simple exercise.

The solid lines in the left-hand panels of Fig. 3 show the phase-folded RV curve for an equal-mass ($q = 1$), circular ($e = 0$), $m_1 = 1$ $M_\odot$ dwarf binary with a very short period ($\log P = 0$) in the top panel and a longer period ($\log P = 4$) in the lower panel, both at the ideal edge-on inclination ($i = 90°$). Note that APOGEE actively took data from 2011-2021, so the survey's maximum baseline is 10 years. With this, I simulated 10 RV observations evenly-spaced in logarithmic scale across 10 years for 1000 identical binary systems. The only difference between each of the 1000 binaries is a randomly assigned orbital inclination (i.e. chosen from a uniform distribution in $\cos i$). An example with high inclination (black circles) and one with low inclination (gray triangles) are shown to highlight the reduction to RV amplitudes from orbital inclination.

The right panel of Fig. 3 demonstrates the effects that the number of RVs and the random distribution of inclinations have upon the reliability of ΔRV_{max}. For each of the 1000 binaries, I randomly selected[2] N_{vis} RVs out of the 10 simulated ones and calculated ΔRV_{max} based solely upon those selected RVs. The squares are plotted at the median ΔRV_{max}, and the upper and lower error bars indicate 75% and 25% quantiles.

As expected, ΔRV_{max} captures a large amount of the short-period binary's RV variability even at $N_{vis} = 2$ RVs, with very little added benefit from $N_{vis} \geq 4$. In the long-period binary, there is again little benefit from $N_{vis} \geq 4$, though ΔRV_{max} performs slightly worse for low N_{vis}, also as expected. Consider, however, that Moe, Kaitlin M. Kratter, and Badenes 2019 used a threshold of $\Delta RV_{max} \geq 1$ km s^{-1} for a sample of APOGEE giants and dwarfs! Even with periods up to $\log P \lesssim 4$, ΔRV_{max} provides a reliable method to identify RV variability in systems with as few as 2 RVs.

With just a few modifications, the simple binary simulator from earlier can be expanded to realistically simulate RV curves for thousands of APOGEE stars. We will simulate $N =$ 100 000 Sun-like main sequences stars ($m = 1$ $M_\odot$, $\log(g) = 4.5$). Each system has a 50% chance to be a binary, in line with the observed binary fraction 0.5 ± 0.04 of solar-type

[2]These were selected without replacement, so no visits were repeated. The values for $N = 10$ reflect ΔRV_{max} calculated using the original 10 simulated RVs.

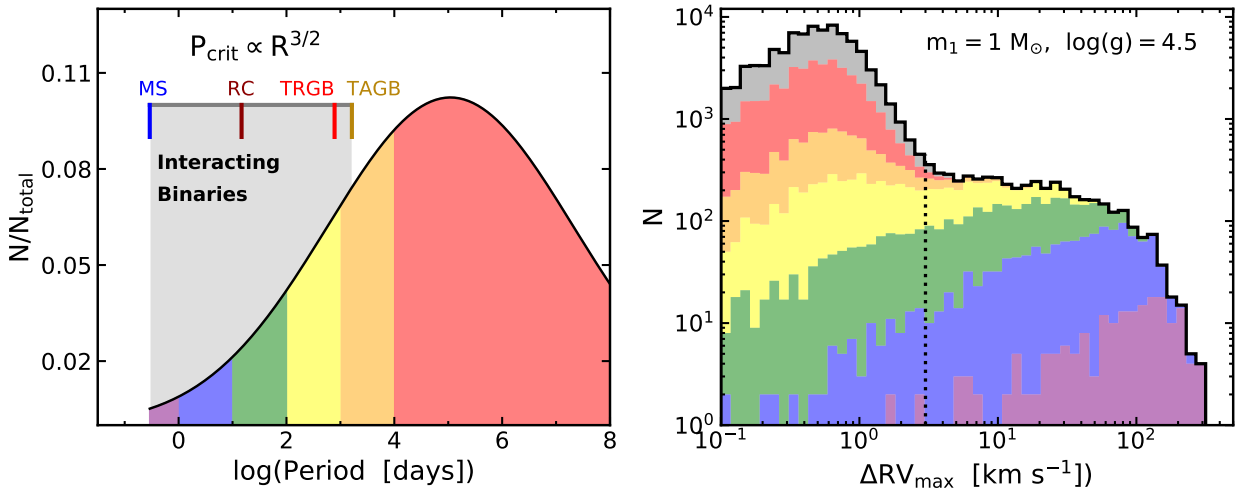

Figure 4: Left panel: Shown in gray is the Raghavan et al. 2010 lognormal period distribution ($\log P = 5.04$, $\sigma_{\log P} = 2.28$), with colored regions denoting various subsamples in orbital period. Binaries in the shaded region will experience mass transfer once $P \approx P_{\rm crit}$, the critical period for Roche lobe overflow, which varies with evolutionary state (labeled tick marks). Right: Stacked histograms of simulated $\Delta {\rm RV}_{\rm max}$ for 100 000 Sun-like main sequence stars, with rainbow colors corresponding to the period subsamples in the left panel and gray representing single stars. The vertical line is drawn at $\Delta {\rm RV}_{\rm max} = 3$ km s^{-1} to highlight the transition from a core dominated by RV errors to a tail of RV variables.

main sequence stars with $\log P < 8$ (Moe and Di Stefano 2017). To mimic real APOGEE observations, all systems, whether binary or single, are randomly assigned the visit history (number of RVs and time lags between observations) of a random star in APOGEE Data Release 14. For every RV observation, a corresponding RV error is drawn from a Student's t distribution with degrees of freedom 3.5, location 0, and scale 0.25.

In order to calculate RVs using equations 1.1-1.4, the binaries are assigned a random orbital inclination, as we did before; a random initial phase; and the primary orbital properties from observational distributions of field solar-type binaries. Chapter 2 discusses the code and distributions in more detail, so I will only briefly summarize the choices used here. Mass ratios are drawn from a flat distribution with $0 < q \leq 1$ (ibid.), and periods are randomly sampled from the Raghavan et al. 2010 lognormal period distribution (left panel of Fig.4). Eccentricities are drawn from a uniform distribution between 0 and the maximum eccentricity allowed by angular momentum conservation (Mazeh 2008; Moe and Di Stefano 2017; Shporer et al. 2016).

Two small exceptions to these prescriptions depend on the assigned period of the system. If the assigned period falls below the critical period for mass transfer via Roche Lobe overflow (P_{crit}), then the code considers the binary to have lost its companion and treats it as being effectively single. Due to its dependence on the primary's radius, P_{crit} also varies with evolutionary changes in a Sun-like star's interior that lead to fluctuations in a star's radius over its lifetime (Badenes, C. Mazzola, et al. 2018). The tick marks in the left panel of Fig. 4 demonstrate this evolution for a 1 $M_\odot$ star passing through the main sequence (MS); tip of the red giant branch (TRGB); core helium burning phase, also known as the red clump (RC); and tip of the asymptotic giant (TAGB). The second exception is for binaries with assigned periods *larger* than P_{crit} but *smaller* than the circularization period (P_{circ}). For a star with $m_1 = 1$ $M_\odot$ and $\log(g) = 4.5$, $P_{circ} = 2.78$ days, considerably longer than the corresponding $P_{crit} = 0.32$ days (calculation taken from ibid., but see also A. M. Price-Whelan and Goodman 2018; Verbunt et al. 1995). Binaries with $P_{crit} < P \leq P_{circ}$ are assumed to have circularized their orbits through tidal interactions and thus assigned $e = 0$.

For the binaries, I sample the projected orbit (equation 1.1) with the assigned visit history and add the random RV errors to the generated RVs. The RVs of the simulated single stars are all zero plus simulated RV errors. This ensures every system will have a non-zero ΔRV_{max} value, a fact that should lead to an important feature in the overall ΔRV_{max} distribution: single stars should have significantly smaller ΔRV_{max} compared to the short-period binaries with large RV amplitudes, but there should also be a transition point where longer period binaries, such as the one shown in the lower panel of Fig. 3, have ΔRV_{max} values *just* larger than the spread caused by random RV uncertainties. Finding this transition point is critical for choosing a ΔRV_{max} threshold that minimizes single star contamination while maximizing the sample size.

The right panel of Fig. 4 shows stacked ΔRV_{max} histograms, with the six different period sub-samples colored in the same way as the left panel and single stars shown in gray. Unsurprisingly, the shortest period binaries (purple and blue) are almost entirely composed of large-ΔRV_{max} systems. More importantly, the low-ΔRV_{max} "core" contains long-period binaries that are indistinguishable from the RV uncertainties of single stars, but this core begins to transition into a "tail" dominated by close binaries displaying genuine RV variabil-

ity roughly at the dotted line shown at $\Delta RV_{max} = 3$ km s^{-1}. Comparisons between observed and simulated ΔRV_{max} distributions can thus inform our choice of a ΔRV_{max} threshold by allowing us to quantify the contamination from single stars and provide a rough estimate for the average RV uncertainties in the observed sample. Numerous observational examples of the ΔRV_{max} distributions will be presented throughout the text and interpreted in this fashion.

So long as we can confidently distinguish the tail of genuine RV variables from single stars with large RV errors, then we are presented with an exciting opportunity. Though we may never have strong constraints on the periods of these stars, ΔRV_{max} still enables us to confidently identify close binaries without surrendering the untapped potential that lays waiting in the hundreds of thousands of APOGEE stars with only a handful of RVs each.

1.3 Dissertation Overview

In Chapter 2, we utilized the synergy of APOGEE DR14 spectroscopy and *Gaia* DR2 astrometry to examine the relationship between stellar multiplicity and a number of stellar parameters for a large sample of APOGEE dwarfs and sub-giants. Our analysis revealed a strong and complex anticorrelation between the close binary fraction and α-process chemical abundances, so the remainder of the chapter is dedicated to characterizing this discovery and considering its implications for binary formation. This work is also available as a peer reviewed publication in C. N. Mazzola et al. 2020.

In Chapter 3, we explored the intersection of stellar evolution, rotation, and multiplicity for a sample of APOGEE DR14 MS and RG stars with rotation speeds $v \sin i$ determined by spectral line broadening. We found that the correlations between $v \sin i$, ΔRV_{max}, and $\log(g)$ are well-fit by theoretical predictions based on simple physical assumptions, and the stellar ages of binaries deviate significantly from the ages predicted by gyrochronology. This work can be accessed as a peer reviewed publication in Daher et al. 2022.

In Chapter 4, we further investigate the formation of binaries by contrasting the observed correlations with chemistry for dwarfs from the spectral types M, K, and G. The

anticorrelations with [Fe/H], [M/H], and [α/H] that we observe for GK dwarfs transition to a mild correlation for M dwarfs at an inflection point of roughly 3800 K (~ 0.5 $M_\odot$). Though preliminary, these results suggest that the importance of different formation channels varies between the M, K, and G-type close binaries in our sample.

Chapter 5 presents our concluding remarks and plans for future work.

2.0 Close Binaries and Stellar Chemistry: a Window into Binary Formation

The accurate characterization of stellar multiplicity remains a key priority in stellar astrophysics. Interacting binaries, defined as those that are close enough to transfer mass and experience significant deviations from single stellar evolution, are responsible for a wide array of phenomena in time-domain astronomy. These include, but are not limited to, cataclysmic variables, novae, all Type Ia and many core-collapse supernovae, high- and low-mass X-ray binaries, and the majority of gravitational wave sources in the LIGO and LISA passbands for a review, see De Marco et al. 2017. The formation rates of these sources in a variety of stellar populations are determined by the initial conditions for stellar multiplicity: the multiplicity fraction, and the distribution of periods, mass ratios, and eccentricities. It is now clear that these fundamental statistics of stellar multiplicity are strong functions of stellar properties like mass and composition, and that they are not independent of each other (see Duchêne et al. 2013; Moe and Di Stefano 2017, for reviews). This realization sets the stage for the challenging observational problem of identifying and characterizing all the relevant correlations between stellar properties and multiplicity statistics in the field.

Fortunately, modern spectroscopic surveys are well suited to this task. The Apache Point Observatory Galactic Evolution Experiment 2 (APOGEE-2, Majewski et al. 2017), one of the constituent surveys in the fourth installment of the Sloan Digital Sky Survey (SDSS-IV, Blanton et al. 2017; Gunn et al. 2006), collected multi-epoch data for 437,485 stars with its high-resolution (R$\sim$22,500) multiplexed infrared spectrograph as part of Data Release 16 (DR16) (Wilson et al. 2019). This constitutes the most comprehensive sample of the detailed compositions of Milky Way stars to date. The APOGEE Stellar Parameter and Chemical Abundances Pipeline (ASPCAP, García Pérez et al. 2016; Jönsson, Holtzman, et al. 2020) has measured reliable stellar parameters for each of these stars, including calibrated abundances of as many as 20 or more elements, and precise radial velocities (RVs, Nidever et al. 2015) for each individual visit spectra. Leveraging the time-domain component of the survey, Badenes, C. Mazzola, et al. 2018 identified a strong anti-correlation between the multiplicity fraction at short periods and stellar metallicity in DR13 of APOGEE (Albareti

et al. 2017) - see also Kareem El-Badry and Rix 2018; Kareem El-Badry, Ting, et al. 2018; Gao, Liu, et al. 2014; Gao, Zhao, et al. 2017; Grether et al. 2007; Liu 2019; Miglio et al. 2021; Pawlak et al. 2019; A. M. Price-Whelan, Hogg, Rix, Beaton, et al. 2020; Raghavan et al. 2010; Yuan et al. 2015. Further analysis by Moe, Kaitlin M. Kratter, and Badenes 2019 established that the metal-poor ([Fe/H]~ -1 dex) dwarfs observed by APOGEE are $\sim$4 times more likely to have short-period ($P \lesssim$30 yr, or $a \lesssim 10$ AU) binary companions than the metal-rich ([Fe/H]$\sim$0.5 dex) dwarfs, and that this trend likely extends to the lower metallicities characteristic of halo stars. This anti-correlation has now been firmly established using large numbers of sparsely sampled RV curves (Badenes, C. Mazzola, et al. 2018; Gao, Liu, et al. 2014; Gao, Zhao, et al. 2017; A. M. Price-Whelan, Hogg, Rix, Beaton, et al. 2020), smaller numbers of systems with known orbital periods (from both complete orbital solutions and eclipses, Moe, Kaitlin M. Kratter, and Badenes 2019), and common-proper-motion binaries with projected separations measured by Gaia (Kareem El-Badry and Rix 2018). This has profound implications for the rates of interacting binaries in the Universe (e.g. De Marco et al. 2017; de Mink et al. 2015; Iben Jr. et al. 1984; Paczynski 1971; A. Price-Whelan et al. 2019; Stanway et al. 2020; Suda et al. 2013) and for the physics of star formation and disk fragmentation (e.g., Duchêne et al. 2013; Kounkel, K. Covey, et al. 2019; Kaitlin M. Kratter, Matzner, et al. 2010; Moe and Di Stefano 2017; Moe and Kaitlin M. Kratter 2018).

Here we continue to explore the relationship between stellar parameters and stellar multiplicity using public data from APOGEE, complemented by Gaia Data Release 2. In order to avoid the details of the interplay between stellar evolution and multiplicity described by Badenes, C. Mazzola, et al. 2018, we restrict our analysis to dwarf and subgiant stars. We examine a wide array of stellar parameters, paying special attention to the abundances of α elements. In Section 2.1, we detail our sample selection and method to account for double-lined spectroscopic binaries (SB2s). Section 2.2.1 describes our completeness corrections. In Section 2.2.2 we describe the broad view of the relationship between stellar multiplicity and stellar parameters in our sample. In Section 2.2.3, we examine in more detail the impact of chemical composition on stellar multiplicity. We discuss our results in Section 2.3 and summarize in Section 2.4.

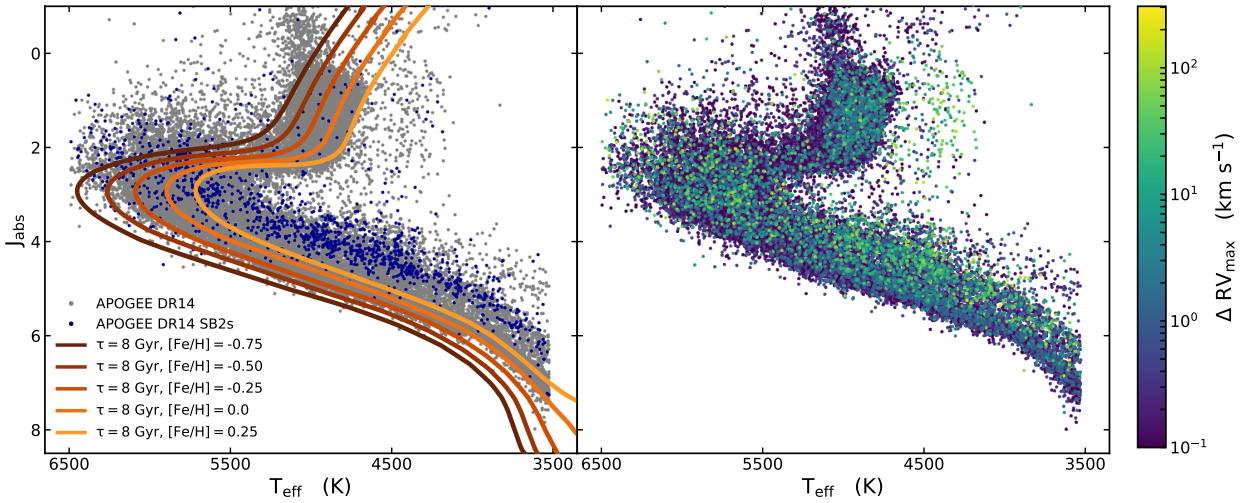

Figure 5: Left panel: An HR diagram for our sample with APOGEE DR14 uncalibrated $T_{\rm eff}$ and the absolute 2MASS J magnitude, calculated using the Sanders et al. 2018 distance estimates. The gray points are for our main sample, and the dark blue are for objects identified as likely SB2s. The colored lines are MIST isochrone tracks for $\tau = 8$ Gyr and various metallicities. Right panel: The same HR diagram but with a colorbar on $\Delta{\rm RV}_{\rm max}$. Points with $\Delta{\rm RV}_{\rm max} \geq 1$ km s^{-1} are plotted on top for clarity.

2.1 Sample Selection

The DR14 version of the APOGEE `allStar` file contains spectral parameters for 277,371 entries (Abolfathi et al. 2018; Holtzman, Hasselquist, et al. 2018; Jönsson, Carlos Allende Prieto, et al. 2018). We first note that there are only 258,475 unique APOGEE IDs amongst these 277,371 entries. The duplicate entries are a result of a star being observed in different fiber plugplates with different field centers, which are not automatically combined by the pipeline. Each `allStar` entry corresponds to a combined spectrum and its measured stellar parameters, and is uniquely described by an APOGEE ID and a field location ID.

From APOGEE DR14, we removed stars with the STAR_BAD flag set in the ASPCAP bitmask (Holtzman, Shetrone, et al. 2015) and those targeted as telluric calibrators (bit 9 in both the apogee_target2 and apogee2_target2 masks; Zasowski, Cohen, et al. 2017; Zasowski, Johnson, et al. 2013). Star cluster members (bit 9 in apogee_target1 and apogee2_target1 and bit 10 in apogee_target2 and apogee2_target2) and commissioning stars (bit 1 in STARFLAG, Holtzman, Shetrone, et al. 2015) were removed as well. Finally, we required acceptable

($\neq -9999$, APOGEE's default for a bad value) uncalibrated effective temperatures ($T_{\rm eff}$) and surface gravities ($\log(g)$) to maximize our ability to distinguish dwarfs from giants in DR14. As noted in Holtzman, Hasselquist, et al. 2018, dwarfs in APOGEE DR14 do not have calibrated $\log(g)$ values, so we do not make cuts on the calibrated parameters. In order to estimate the dereddened JHK_s magnitudes, we used the value of $A_{\rm K}$ adopted for targeting purposes (AK_TARG, Zasowski, Cohen, et al. 2017; Zasowski, Johnson, et al. 2013).

For each APOGEE ID/location ID combination, we identified the individual visits from the `allVisit` file that were included in its combined APOGEE spectrum (the VISITS_PK indices, Holtzman, Shetrone, et al. 2015; Nidever et al. 2015). We imposed an additional quality cut, requiring two or more of these visits to have a S/N$\geq$ 40. If a star had duplicate APOGEE IDs, all of the acceptable visit RVs from its various plugplate fields were concatenated. This meant that objects with at least one acceptable visit in two or more fields could be included. For these stars, we averaged any duplicate stellar parameters with valid values from the pipeline.

Both the APOGEE data reduction pipeline (Nidever et al. 2015) and ASPCAP (García Pérez et al. 2016) assume that each source can be modeled by a single stellar spectrum. Stellar companions within the range of mass ratios $q = M_2/M_1$ that can make a significant contribution to the observed flux (double-lined spectroscopic binaries or SB2s) can therefore introduce biases in the spectral fits; see K. El-Badry et al. 2018 for a discussion. To identify these stars, we examined the APOGEE cross-correlation functions (CCFs), following the procedure described in Kounkel, K. Covey, et al. 2019. Two approaches were considered: using CCFs that APOGEE provides natively in its data releases, and recalculating the CCFs by cross-matching the spectra with the best-fit PHOENIX synthetic spectrum (Husser et al. 2013), using the reported RV_TEFF and RV_LOGG parameters. In most cases, the deconvolution of multiple components from the CCFs occurred in the same sources, with comparable RVs. In this way, we identified 3656 likely SB2s within APOGEE DR14, of which 1512 were in our quality-cut sample. From the CCFs for these stars, we determined the RV of the highest peak at each epoch and used this as a more reliable estimate for the RV of the photometric primary. After applying our quality cuts, we were left with 1495 likely SB2s, which we kept in our sample with spectral parameters from APOGEE/ASPCAP and RVs

from our CCF analysis. Details about the downloadable tables of these SB2s are available in Appendix 2.7.

In a final step, we restricted our sample to $\log(g/\mathrm{cm\ s^{-2}}) \geq 3.25$, [Fe/H] ≥ -1.0 dex. This simple cut in $\log(g)$ will not purely select dwarfs, but it is sufficient for our purposes in eliminating most stars on the red giant branch. We also imposed an additional requirement of acceptable values ($\neq -9999$) for [α/Fe], [α/H], [O/H], [Mg/H], and [Si/H]. This left us with 41,363 unique APOGEE targets, 1278 of which were identified as SB2s, and 3896 (131 SB2s, 3765 non-SB2s) had duplicate entries and so their stellar parameters were averaged. The fraction of SB2s in this sample is 1278/41,363 = 3.1 $\pm$ 0.1 per cent, consistent with the 2.8 $\pm$ 0.2 per cent value measured in young stellar objects by Kounkel, K. Covey, et al. 2019.

Unlike ibid., which focused primarily on the young stellar objects, most of the sources deconvolved as SB2s in this work are main sequence stars, and their CCFs are not affected by variability due to star spots. Therefore, it is possible to reliably include sources with quality flag 3 in addition to 4 in the list of likely SB2s (see Table 5 and Section 4.1 in ibid. for an explanation of these flags). Thus, we caution against blindly comparing these fractions. Kareem El-Badry, Ting, et al. 2018 used a more sophisticated method based on *The Payne* (Ting et al. 2019), to identify SB2s from RV shifts among dwarf stars in APOGEE DR12. Their measured SB2 fraction from this method is 663/20,142 = 3.3 $\pm$ 0.1 per cent, which is consistent with our results. These authors also found SB2s by making multi-component spectral fits, and found a higher SB2 fraction of 2645/20,142 = 13.1 $\pm$ 0.2 per cent. However, many of the systems identified by this method had small or negligible RV shifts and therefore this higher SB2 fraction is hard to compare with what we measure in our RV-selected sample.

We cross-matched our final sample of APOGEE targets with the catalog from Sanders et al. 2018, who calculated Bayesian posteriors on distance d, mass M, and age τ, by fitting PARSEC isochrones to a combination of Gaia DR2 parallaxes, broadband photometry, and the spectral parameters derived by ASPCAP. ibid. give non-NAN values of d, M and τ for the vast majority (41,014, or 99 per cent) of the stars in our sample. We use these distance estimates to plot absolute 2MASS magnitudes J_{abs} vs. uncalibrated APOGEE T_{eff} in Fig. 5. The left panel shows the bulk of our sample in gray with the SB2s over-plotted in dark blue.

Isochrones from the MESA Isochrone and Stellar Tracks Collaboration (MIST; Choi et al. 2016; Dotter 2016; Paxton, Bildsten, et al. 2011; Paxton, Cantiello, et al. 2013; Paxton, Marchant, et al. 2015) are shown for $\tau = 8$ Gyr and a range of representative metallicities. According to Sanders et al. 2018, the age distribution in our sample peaks around 8 Gyr, which is in good agreement with the main sequence turn-off point shown in Fig. 5. The majority of the SB2s lie above the single star isochrone tracks, as expected for systems with a measurable flux contribution from both components. The right panel shows the same HR diagram colored by the maximum shift in the RVs, $\Delta\mathrm{RV}_{\mathrm{max}}$ (see Badenes and Maoz 2012; Badenes, C. Mazzola, et al. 2018; Maoz et al. 2012; Moe, Kaitlin M. Kratter, and Badenes 2019), with stars that have $\Delta\mathrm{RV}_{\mathrm{max}} \geq 1$ km s^{-1} plotted on top for clarity. Here too we find a significant excess of objects with large RV variability to have locations above the single-star isochrones.

2.2 Results

2.2.1 Stellar multiplicity, $\Delta\mathrm{RV}_{\mathrm{max}}$ distributions, and completeness corrections

Following Badenes and Maoz 2012, Maoz et al. 2012, and Badenes, C. Mazzola, et al. 2018, we use $\Delta\mathrm{RV}_{\mathrm{max}}$ as a figure of merit to evaluate the sparsely sampled RV curves from APOGEE. Most (42.9 per cent) of the stars in our sample have 3 visits, with 36.4 per cent having 2 and the rest having 4 or more. While this is not enough to define a full orbital solution for most stars (see A. M. Price-Whelan, Hogg, Rix, Beaton, et al. 2020; A. M. Price-Whelan, Hogg, Rix, N. D. Lee, et al. 2018, for discussions), values of $\Delta\mathrm{RV}_{\mathrm{max}}$ above a certain threshold can securely identify large numbers of short-period binaries. In Fig. 6, we show the distribution of $\Delta\mathrm{RV}_{\mathrm{max}}$ in two groups of $N \sim 2000$ stars with constant [Fe/H] and [Mg/H]. This example illustrates the two main features of $\Delta\mathrm{RV}_{\mathrm{max}}$ distributions derived from high quality data: a core of low $\Delta\mathrm{RV}_{\mathrm{max}}$ values dominated by measurement errors and an extended tail of high $\Delta\mathrm{RV}_{\mathrm{max}}$ values dominated by stars with companions in short-period orbits, clearly defined and cleanly separated from the core. We refer the reader

to the discussions in Badenes, C. Mazzola, et al. 2018 for the role of measurement errors, metallicity, and RV jitter in the APOGEE ΔRV_{max} distributions. Here we focus on two closely related issues: the completeness corrections and the threshold value of ΔRV_{max} to single out multiple systems.

We estimate completeness corrections on these ΔRV_{max} distributions with a Monte Carlo sampler similar to that used by Moe, Kaitlin M. Kratter, and Badenes 2019. Our sampler simulates a population of N systems, with the fraction of systems in binaries determined by a free parameter called the multiplicity fraction f_m. Each system is assigned a visit history (number of visits and time lags between visits) from a random star in our APOGEE DR14 dwarf/subgiant sample. For each simulated binary, we draw the main orbital parameters (period and eccentricity) from the observational distributions measured for field solar-type binaries (period, Raghavan et al. 2010; eccentricity, Moe and Di Stefano 2017), select a random orbital inclination and initial phase, and generate RVs by sampling the projected orbit with the visit history, adding RV errors from a user-specified distribution. For each simulated single star, we set all RVs to zero and add errors from the same distribution. The code is described in more detail in Badenes, C. Mazzola, et al. 2018 – here we list the specific choices made for the present work. We simulate $N = 50,000$ stars with $f_m = 0.5$. Each star is assigned $\log(g/\mathrm{cm\ s^{-2}}) = 4.25$, the median value for our sample, which corresponds to a critical Roche Lobe Overflow period of $P_{\mathrm{crit}} = 0.49$ days in a 1 $M_\odot$ binary with $q = 1$. The primary mass M is randomly drawn from the distribution of Sanders et al. 2018 mass estimates for our sample (shown in the second diagonal panel of Fig. 8). For the mass ratio q, we assume a flat distribution with a twin excess fraction of 25 per cent for systems with $0.95 \leq q \leq 1.0$ (Moe and Di Stefano 2017). The RV errors are drawn from a Student's t distribution (scipy.stats.t) with degrees of freedom 3.5, location 0 and scale 0.25. Appendix 2.5 discusses these choices and their effects on the completeness corrections in more detail.

In Table 1 and the left panel of Fig. 7, we show the cumulative fraction of systems with ΔRV_{max} above a given value in several period ranges in our Monte Carlo simulation. Assuming the underlying period and eccentricity distributions are not too different from the assumed ones, the completeness correction that needs to be applied to recover the total

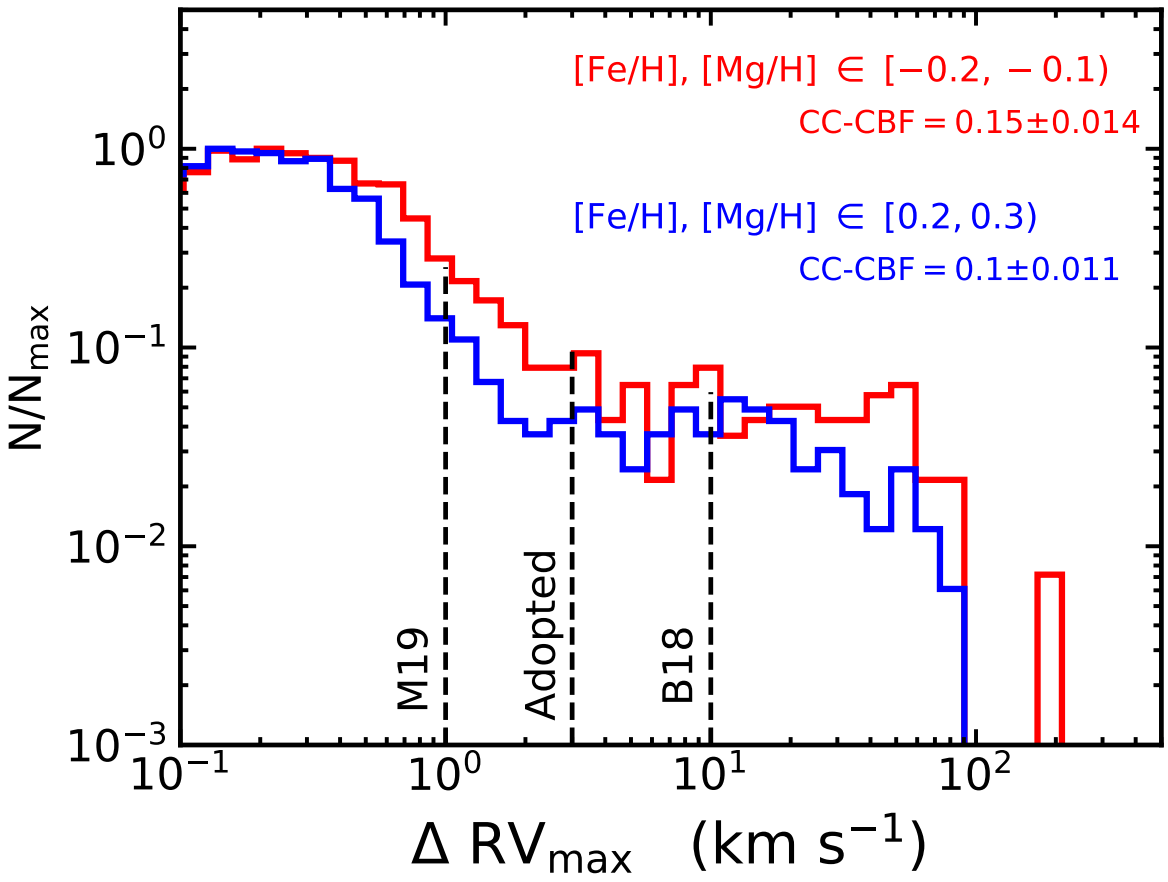

Figure 6: Normalized distributions of ΔRV_{max} for two boxes with $N \sim 2000$ in [Fe/H]-[Mg/H] space from Fig. 8. The ΔRV_{max} thresholds from Moe, Kaitlin M. Kratter, and Badenes 2019, Badenes, C. Mazzola, et al. 2018, and the present work are shown as dashed lines.

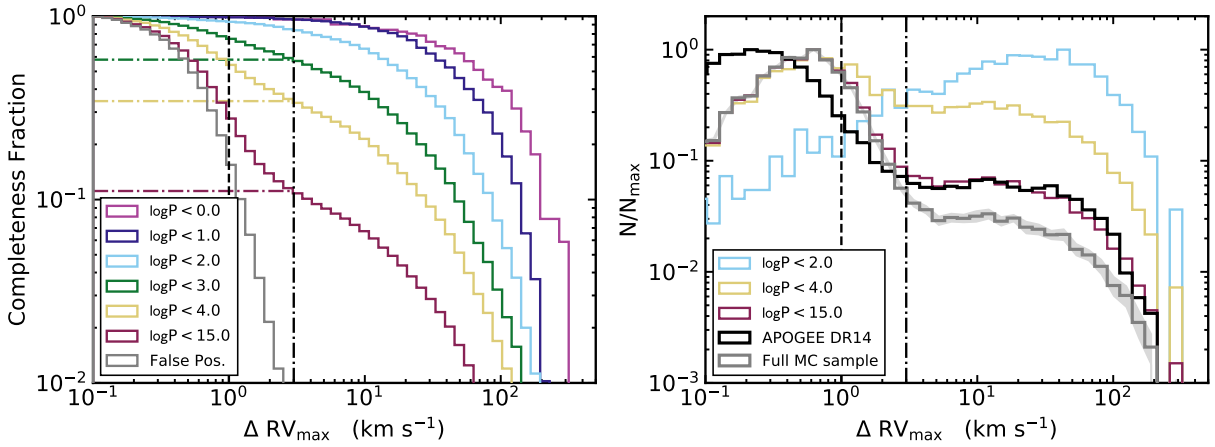

Figure 7: Left panel: Completeness fraction versus $\Delta\mathrm{RV}_{\mathrm{max}}$ for Monte Carlo generated samples at various period limits, using the APOGEE DR14 time lags from our sample. The horizontal dot-dashed lines are the completeness fractions for the relevant $\log(P/\mathrm{days})$ samples given a threshold $\Delta\mathrm{RV}_{\mathrm{max}} \geq 3$ km s^{-1}. The vertical dashed line is at $\Delta\mathrm{RV}_{\mathrm{max}} = 1$ km s^{-1} for comparison. The gray histogram shows the completeness fraction for false positives–systems that are not binaries but show some RV variation due to simulated RV error. Right panel: normalized $\Delta\mathrm{RV}_{\mathrm{max}}$ distributions for MC data. The fainter lines are for several $\log(P/\mathrm{days})$ samples, color-coded as in the left panel. The gray histogram is for the full MC sample (binaries and non-binaries included), with shading indicating 1σ intervals from bootstrapping the sample ($N_{\mathrm{boots}} = 25$). The black histogram is for our APOGEE DR14 sample.

Table 1: Completeness fractions for selected $\log(P/\text{days})$ and $\Delta\text{RV}_{\text{max}}$ thresholds.

$\log(P/\text{days})$ threshold	$\Delta\text{RV}_{\text{max}} \geq 1$ km s^{-1}	$\Delta\text{RV}_{\text{max}} \geq 3$ km s^{-1}	$\Delta\text{RV}_{\text{max}} \geq 10$ km s^{-1}
$\log P \leq 0.0$	1.00	0.96	0.88
$\log P \leq 2.0$	0.93	0.84	0.66
$\log P \leq 4.0$, this work	0.55	0.34	0.21
$\log P \leq 4.0$, from Moe, Kaitlin M. Kratter, and Badenes 2019	0.57	0.40	0.24
$\log P \leq 15.0$	0.29	0.11	0.07
False Positives	0.17	0.005	0.00

number of binaries with periods below a certain value is the inverse of these cumulative fractions. Our results are consistent with those of Moe, Kaitlin M. Kratter, and Badenes 2019 (included in Table 1), who applied a similar approach to a sample of APOGEE DR13 dwarfs. The gray and red histograms in Fig. 7 show the cumulative fractions for all non-binary and binary systems, respectively. The false positive rate for binaries in a given period range at a given value of $\Delta\mathrm{RV}_{\mathrm{max}}$ is the ratio between the relevant cumulative fraction and the gray histogram at that value of $\Delta\mathrm{RV}_{\mathrm{max}}$.

These curves inform our choice of $\Delta\mathrm{RV}_{\mathrm{max}}$ threshold value. A conservative value like the 10 km s^{-1} chosen by Badenes, C. Mazzola, et al. 2018 is virtually free of false positives, but results in low detection efficiencies and correspondingly large completeness corrections, which can lead to issues when dealing with small samples of systems with a specific set of stellar parameters. For the dwarf and subgiant stars that we examine here, which have low RV jitter (Hekker et al. 2008) and relatively narrow $\Delta\mathrm{RV}_{\mathrm{max}}$ distribution cores (Badenes, C. Mazzola, et al. 2018), we propose a more reasonable value of 3 km s^{-1}. Using the uncertainties reported by the APOGEE data reduction pipeline, the median RV uncertainty for our sample is $\sigma_{RV} \sim 0.04$ km s^{-1}, though these uncertainties are almost certainly underestimated (see discussions in Badenes, C. Mazzola, et al. 2018; Holtzman, Hasselquist, et al. 2018, and sources within). We can instead consider a more reasonable value of $\sigma_{RV} \sim 0.2$ km s^{-1}, obtained from roughly fitting the observed $\Delta\mathrm{RV}_{\mathrm{max}}$ distribution core to those simulated by our MC with Gaussian error distributions with mean of 0 and varying spreads (similar to APOGEE DR13, see Fig. 9 of Badenes, C. Mazzola, et al. 2018). Regardless, our threshold remains far larger than what can be explained with typical RV uncertainties alone. This threshold yields a detection efficiency of ≈ 34 per cent for systems with $\log(P/\mathrm{days}) \leq 4.0$ and ≈ 84 per cent for $\log(P/\mathrm{days}) \leq 2.0$, with an overall false positive rate of ≈ 0.1 per cent. Compared to Moe, Kaitlin M. Kratter, and Badenes 2019, who chose a threshold value of $\Delta\mathrm{RV}_{\mathrm{max}} \geq 1$ km s^{-1}, we expect a false positive rate about 30x lower, with only a modest loss of ≈ 20 per cent in detection efficiency.

In the context of our APOGEE sample, completeness corrections for systems with $\log(P/\mathrm{days}) > 4$ ($a > 10$ AU) are unwarranted for several reasons. These long-period binaries will rarely produce detectable RV variability in APOGEE, and are often difficult

to characterize using sparsely sampled RV curves. Moreover, the anti-correlation between stellar multiplicity and [Fe/H] weakens beyond $a > 50$ AU and disappears beyond $a > 200$ AU (Kareem El-Badry and Rix 2018; Moe, Kaitlin M. Kratter, and Badenes 2019), and this might apply to other stellar parameters. Therefore, in the remainder of this work we will quote completeness-corrected binary fractions for systems with $\log(P/\mathrm{days}) \leq 4$, which we identify as 'close binaries'. For reference, a 1 $M_\odot$ star of solar composition at the tip of the red giant branch has a critical period for Roche Lobe overflow of $\log(P/\mathrm{days}) \sim 2.8$.

In the right panel of Fig. 7 we compare the simulated $\Delta\mathrm{RV}_{\mathrm{max}}$ distribution from our MC run to the observed distribution in the APOGEE sample. We estimate 1σ intervals on the simulated distribution (shown as the gray shading) by bootstrapping the sample with $N_{\mathrm{boot}} = 25$, $N_{\mathrm{sys}} = 40,000$. We also show the $\Delta\mathrm{RV}_{\mathrm{max}}$ distributions in three different subsets of simulated systems: those with $\log(P/\mathrm{days}) < 15$ (all binaries), $\log(P/\mathrm{days}) < 4$ (all close binaries), and $\log(P/\mathrm{days}) < 2$. We do not attempt to provide an accurate match to the observed $\Delta\mathrm{RV}_{\mathrm{max}}$ distribution, as this would require a complete characterization of the correlations between stellar properties, multiplicity, and RV errors, but we note that the shape and extent of the tail in our simulation is very similar to what we see in the APOGEE sample. We also note that our choice of RV error distribution is conservative, as shown by the comparison between the simulated and observed core shapes.

Binaries in general, and twins in particular, can be detected further away than single stars in magnitude-limited samples due to Malmquist bias (see Fig. 5). Conversely, it is more difficult to detect RV variability of twin SB2s if their absorption features are significantly blended (but see Kareem El-Badry, Ting, et al. 2018, for an alternative approach). In their analysis, Moe, Kaitlin M. Kratter, and Badenes 2019 estimated that these two effects bias the close binary fraction measured by APOGEE by ≈ 30 per cent in opposite directions and therefore approximately cancel each other. However, they relied solely on the APOGEE pipeline RV measurements, while we applied a CCF method to identify SB2s and more accurately measure their RVs. Our Malmquist bias in favor of detecting twin binaries should therefore be slightly greater than our inefficiency in the detection of RV variability in SB2s. We compensate for this by reducing our completeness-corrected close binary fractions by 10 per cent to make the reported values more representative of volume-limited samples. This

results in an estimated detection efficiency of 0.38 for $\Delta\mathrm{RV}_{\mathrm{max}} \geq 3$ km s^{-1} and $\log(P/\mathrm{days}) \leq 4$, which we adopt for the remainder of this work. Using this completeness correction, the close binary fractions we recover from the $\Delta\mathrm{RV}_{\mathrm{max}}$ distributions shown in Fig. 6 are 0.15 ± 0.014 and 0.1 ± 0.011.

2.2.2 The Impact of Stellar Parameters on the Close Binary Fraction

We are now in a position to examine the impact of stellar parameters on the completeness-corrected close binary fractions measured in our sample of APOGEE dwarfs and subgiants. To do this, we choose a few representative parameters among those measured by APOGEE and Sanders et al. 2018: T_{eff}, M, [Fe/H], [Mg/H], [Si/H], τ, the vertical action J_z, and the galactocentric radial velocity v_R. The vertical action is defined as

$$J_z = \frac{1}{2\pi} \oint dz v_z \tag{2.1}$$

where z and v_z are the position and galactocentric vertical velocity for the star along its orbit. As an indicator of a star's vertical displacement, J_z is unaffected by orbital phase as compared to z or v_z, and it is a tracer of the birth location of stars in the Milky Way disk that is more robust to radial migration than galactocentric radius (Vera-Ciro et al. 2014).

Several of these parameters are precisely determined by APOGEE (T_{eff}, chemistry), whereas others represent fundamental stellar properties (M, τ) or are related to galactic dynamics that may prove interesting (J_z, v_R). Of course many of these parameters, like τ and [Fe/H], have substantial internal correlations that cannot be properly examined without a multivariate analysis. Moreover, we are restricted to the parameter ranges covered by APOGEE, which are very broad for some parameters like [Fe/H], but quite narrow for others that are of high interest for stellar multiplicity, like M. Finally, not all these parameters are equally well constrained by the observations. Stellar ages, for example, are notoriously hard to estimate without asteroseismic data (e.g., see Ness et al. 2016; Marc H. Pinsonneault et al. 2018). We also note that both ASPCAP and Sanders et al. 2018 *assume* single star models, which can introduce biases in some parameters (see K. El-Badry et al. 2018, for a discussion).

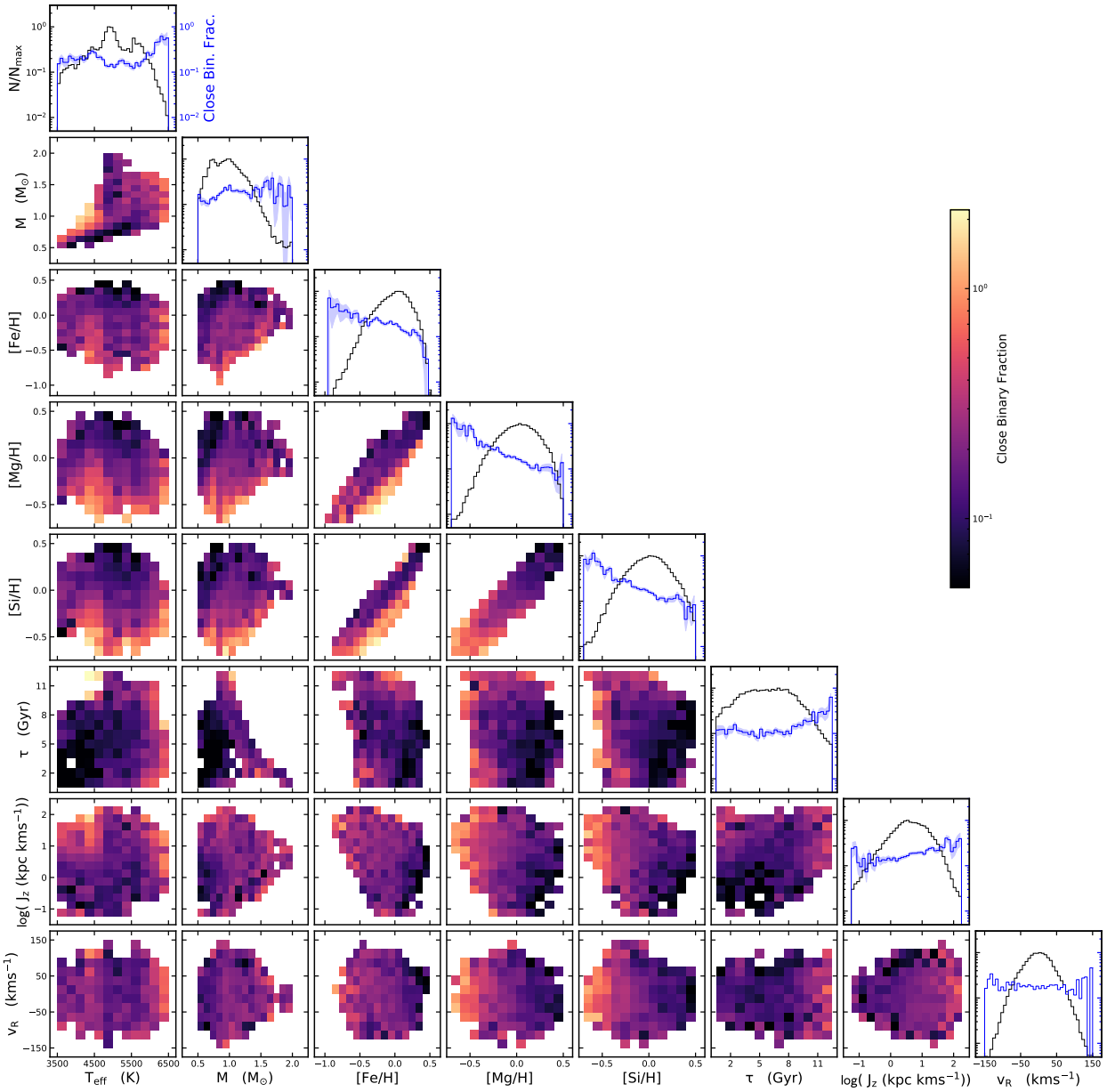

Figure 8: Two-dimensional histograms showing the completeness-corrected close binary fraction as a function of many of the parameters considered in this work. Along the diagonal, the black lines are the normalized histograms of each parameter, and shown in blue is the completeness-corrected close binary fraction as a function of that parameter alone. The blue shaded region shows the uncertainties on the completeness-corrected close binary fraction (equation 2.2).

Table 2: Fit parameters and the number of σ (estimated via bootstrapping) for the parameter to be consistent with 0.

	$\log f_m = b + aX$		$\log f_m = c + bX + aX^2$			
	b	a	c	b	a	$\chi^2_{\rm lin}/\chi^2_{\rm quad}$
$T_{\rm eff}$ (K)	-1.595	1.9e-7	3.318	-0.002	1.9e-7	2.7
		2.7σ		5.4σ	5.8σ	
M ($M_\odot$)	-0.815	0.11	-1.329	0.993	-0.34	1.5
		2.1σ		3.1σ	2.5σ	
[Fe/H] (dex)	-0.787	-0.595	-0.782	-0.436	0.196	0.98
		8.6σ		4.7σ	1.2σ	
[Mg/H] (dex)	-0.806	-1.32	-0.752	-0.851	0.627	3.5
		13.0σ		6.6σ	2.7σ	
[Si/H] (dex)	-0.77	-1.15	-0.755	-1.011	0.187	1.3
		9.1σ		3.6σ	0.5σ	
τ (Gyr)	-1.355	0.077	-0.696	-0.127	0.013	4.7
		2.8σ		3.5σ	4.4σ	
$\log(J_z/\text{kpc km s}^{-1})$	-0.76	0.142	-0.783	0.045	0.062	1.4
		5.0σ		1.1σ	2.7σ	
v_R (km s^{-1})	-0.662	1.0e-5	-0.757	1.0e-4	1.0e-5	1.1
		0.1σ		0.4σ	2.4σ	

With all these caveats in mind, we present our view of the impact of stellar parameters on the close binary fraction in Fig. 8. This triangle plot shows the completeness-corrected close binary fraction as a two-dimensional histogram mapped on each pairwise combination of parameters. The one-dimensional terminal plots show the full distribution of each parameter in the APOGEE sample (black histograms) and the completeness-corrected close binary fraction as a function of that parameter alone (blue histograms with shaded error bars). We required a minimum of ten objects per bin in order to extend our measurements through the sample's full range of parameter space. Uncertainties are not shown in the 2D histograms, but they scale as σ_f/c, where $c = 0.38$ is the completeness-correction discussed in Section 2.2.1, and σ_f is the uncertainty from the binomial process on each measurement,

$$\sigma_f = \sqrt{\frac{f(1-f)}{N}} \tag{2.2}$$

where f is the fraction of systems with $\Delta\mathrm{RV}_{\mathrm{max}} \geq 3$ km s^{-1}, and N is the total number of systems in that bin. Measurements made with small-N samples will be noisy due to the $\sqrt{1/N}$ factor, but the RV variable fraction f also introduces a $\sqrt{f(1-f)}$ factor. For a bin with $N = 10$, we can consider two cases: (1) $f = 0.2$ and (2) $f = 0.8$. In both instances, the binomial process uncertainty is $\sigma_f/c = 0.33$. The completeness-corrected close binary fractions are (1) $f_m = 0.52 \pm 0.33$ and (2) $f_m = 2.09 \pm 0.33$, showing that it is possible to measure variations in the close binary fraction even in bins with N as small as 10.

Note also that our completeness-correction can result in close binary fractions that are in excess of 100 per cent, and we indeed see bins with values of $f_m \sim 2.0$ in Fig. 8. We assumed the same period distribution for the entire simulated sample, and this assumption is most likely not valid across our diverse APOGEE sample. From the ASAS-SN Catalog of Variable Stars, Jayasinghe et al. 2021 found that metal-poor eclipsing binaries were skewed towards shorter periods than metal-rich systems at fixed temperature. A shift towards shorter periods for metal-poor stars results in an over-correction from the completeness estimate, leading to our excessively large close binary fractions. Future studies of the period distribution as a function of chemistry and metallicity will be useful for addressing this issue.

The salient features of Fig. 8 can be summarized as follows:

1. The parameters related to chemical composition ([Fe/H], [Mg/H], and [Si/H]) emerge as the dominant drivers of stellar multiplicity in our sample. The completeness-corrected close binary fractions as a function of these parameters (blue 1D histograms in the diagonal panels) show clear monotonic downward trends, with dynamic ranges in excess of an order of magnitude, that are distinctly larger than for any other parameters. The gradients due to this downward trend are the most striking feature in all the 2D histograms that include chemical composition parameters. While the trends are uniform and monotonic in the 1D histograms, the 2D histograms reveal a great deal of complexity in the relationship between stellar multiplicity and chemical composition, which we examine in further detail in Section 2.2.3.
2. Even though stellar mass (and by proxy, $T_{\rm eff}$) is known to have a strong effect on the close binary fraction of field dwarfs (Duchêne et al. 2013; Lada 2006; Moe and Di Stefano 2017), this is not clear in the APOGEE sample. The close binary fraction ($\log(P/\text{days}) \lesssim 4$) for Solar-mass stars scales as $M^{0.5}$ (Moe and Di Stefano 2017), so we expect the close binary fraction to increase by a factor of 2 across the sample's mass range. From the 1D histogram, we observe the close binary fraction increasing by a factor of ~ 1.5. However, the close binary fraction measurements in the high-M bins are noisy, and the mass estimates themselves are poorly constrained compared to APOGEE $T_{\rm eff}$, so our measurement alone cannot be considered to be at odds with previous work. We do detect a noticeably higher close binary fraction for the hottest ($T_{\rm eff} \gtrsim 6000$ K) stars, which A. M. Price-Whelan, Hogg, Rix, Beaton, et al. 2020 also found in a sample of binaries in APOGEE DR16. While this spike may be due to larger primary masses, the correlation at lower temperatures seem weaker. This might be due to the overlap between dwarfs and subgiants below 6000 K (apparent in Fig.5). In the $T_{\rm eff}$-M 2D histogram, there appears to be a region of increased binaries around 4000 K and 1 $M_\odot$, though this is more likely to be a result of erroneous mass estimates, given the temperature and mass values.
3. Stellar age shows a modest upward trend, though this is hard to interpret. Stellar ages are poorly constrained in general, and age estimates for SB2s are particularly prone to errors: SB2 systems may be mis-classified as overly young (100s Myr) or overly old (> 10

Gyr), because stars that are offset from the MS, like the high-ΔRV_{max} objects in Fig. 5, may be classified along stellar pre-MS or post-MS tracks. This could account for the apparent increase in multiplicity fraction for $\tau > 8$ Gyr. There is also a well established (though complex) correlation between [α/Fe], [Fe/H], and age (J Ted Mackereth et al. 2019, 2017, and sources within), which is often used in studies of galactic dynamical evolution. A more complete treatment of these correlations is required before we can comment on any trends between age and the close binary fraction.

4. The 1D histogram for $\log J_z$ shows a significant correlation with the completeness-corrected close binary fraction, but this could simply be due to the fact that the outer disk is more metal-poor (e.g., in APOGEE Hayden et al. 2015; Weinberg et al. 2019, and sources within).
5. The galactocentric radial velocity shows the flattest distribution of the parameters studied here. In the 1D histogram, the bins at either edge in parameter space appear to have an increased binary fraction, but they are consistent with a flat distribution given their large uncertainties.

To quantify the impact of each parameter on the multiplicity fraction, we fit linear and quadratic functions to each of the blue histograms along the diagonals of Fig. 8. The best fit parameters and the ratio between the χ^2 are given in Table 2. None of the distributions are necessarily expected to follow a linear or quadratic function, but these are simple, easily-fit functions that provide an estimate of the slopes of the distributions. We then bootstrapped ($N_{\rm boot} = 500$) the fits to estimate uncertainties on the fit parameters. We can then calculate the number of σ required for the first and second derivatives to be consistent with zero. These values are listed in the second row for each parameter in Table 2, with significant values ($n > 2$) in purple and highly significant values ($n > 5$) in blue. From these values, we conclude that the chemical composition parameters show the most significant correlations with close binary fraction in our sample, though there are also clear trends with stellar age, mass, $T_{\rm eff}$, and vertical action. We recover the strong anti-correlation between [Fe/H] and the completeness-corrected close binary fraction previously reported by various authors, and identify for the first time a similar effect in both sign and strength for α-process elements Mg and Si. Characterizing these correlations is the subject of the remainder of this paper.

2.2.3 Chemical Composition and the Close Binary Fraction

The completeness-corrected close ($\log(P/\text{days}) \leq 4.0$) binary fraction as a function of [Fe/H] alone is shown in Fig. 9. We divided our sample into eight bins in [Fe/H], chosen to contain approximately 5200 stars each. A linear fit to these data shows that the close binary fraction decreases by a factor of ~ 2.4 from [Fe/H] $= -0.5$ dex to [Fe/H] $= 0.25$ dex. As we have seen, however, the relationship between chemical composition and stellar multiplicity is complex, and it cannot be characterized by metallicity alone. Here we consider in detail four parameters related to the abundance of α-process elements: [Mg/H] and [Si/H] (already discussed in Section 2.2.2), plus [α/H] and [O/H]. The measurements of [C/H] and [N/H] for APOGEE DR14 dwarfs are not reliable (Holtzman, Hasselquist, et al. 2018), so we did not include them in our analysis.

We begin by revisiting the two-dimensional histograms of completeness-corrected close binary fraction. Each panel in Fig. 10 shows an α-process abundance measurement a function of [Fe/H], similar to the 2D histograms of Fig. 8, but with a lower minimum count of five stars per bin to maximize parameter space coverage. The close binary fraction again exceeds 100 per cent in multiple bins, though this still may due to the degeneracies present in our RV variability fraction method discussed in Sec. 2.2.2. The anti-correlation between close binary fraction and [Fe/H] is apparent as the trend along the diagonal, and it is present for all six α abundances. The additional anti-correlation with α abundance is clear when looking along lines of constant [Fe/H], manifesting as two distinct sequences: α-poor with large close binary fractions, and α-rich with smaller close binary fractions. The weakest effect is seen in [O/H], but the anti-correlation is obvious for [α/H], [Mg/H], [Mg/Fe], and Si. However, especially around solar metallicity, [α/H], [O/H], and [Si/H] show increased close binary fractions at low *and* high values when looking along lines of constant [Fe/H].

To study these effects in a regime that is not prone to numerical noise due to small numbers of stars, we use the same bins as those shown in Fig. 9 ($N \sim 5200$ each). The gray squares in the first column of Figs. 11-12 are plotted at the median [Fe/H] and α abundance for each bin, with each row showing one of the four α abundance measurements from earlier, plus [α/Fe]. Within each [Fe/H] bin we define "low-X" and "high-X" subsamples, with X

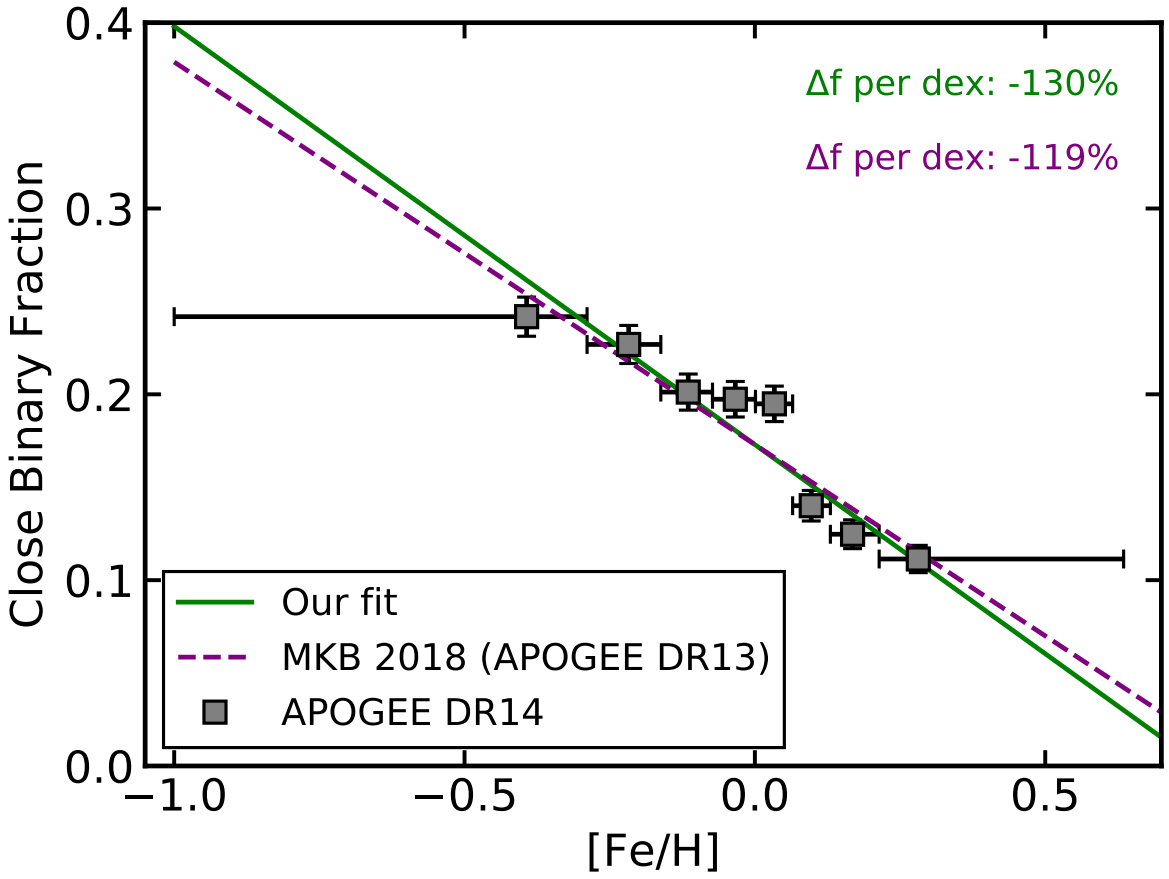

Figure 9: Completeness-corrected close binary fraction for each [Fe/H] bin. The horizontal error bars show the [Fe/H] range of each bin, and the vertical error bars show the completeness-adjusted uncertainty, σ_f/c. The results of Moe, Kaitlin M. Kratter, and Badenes 2019 are over-plotted alongside a linear fit to our data in order to find the difference in the close binary fraction per dex of [Fe/H].

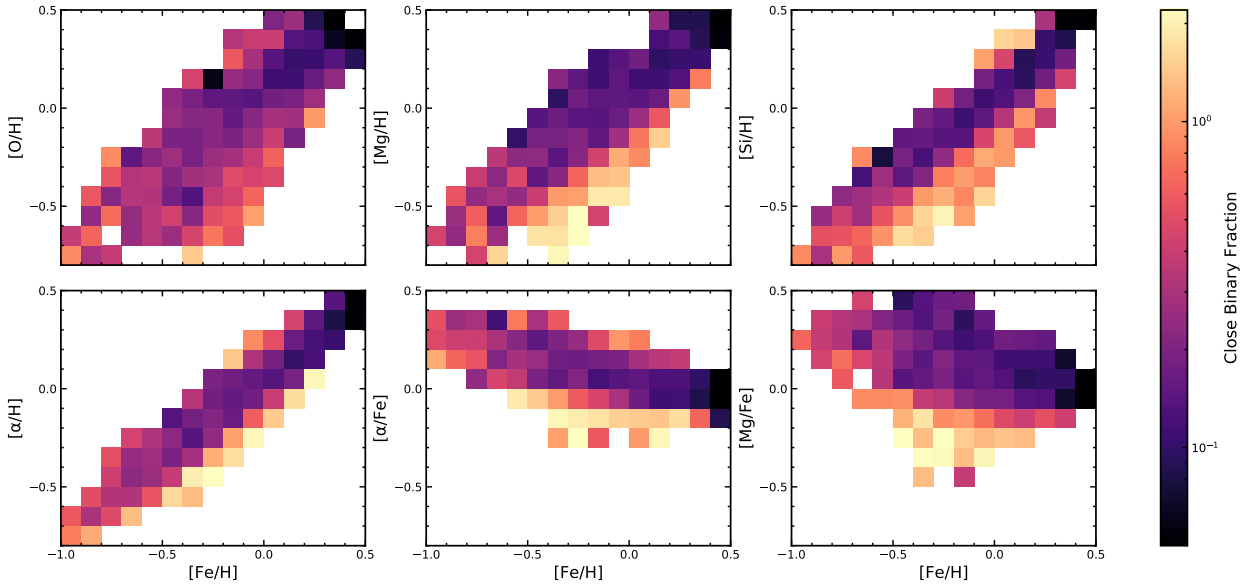

Figure 10: Two-dimensional histogram showing the completeness-corrected close binary fraction as a function of [Fe/H] and various α abundances.

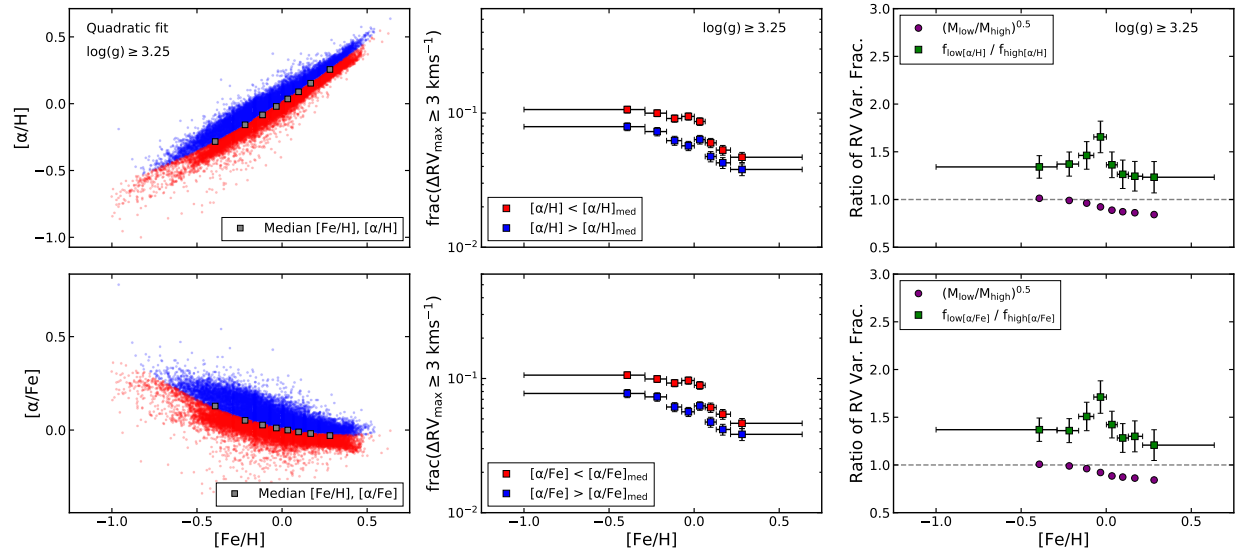

Figure 11: First row: [left] distribution of [α/H] and [Fe/H], with the gray points placed at the median [Fe/H]/[α/H] of each bin and the red points showing the "low-[α/H]" subsample and blue the "high-[α/H]" subsample; [center] the fraction of systems with $\Delta RV_{max} \geq 3$ km s^{-1} for the low- and high-[α/H] subsamples, with the horizontal error bars showing the range of [Fe/H] in each bin and the vertical error bars showing the uncertainty, equation (2.2); and [right] the ratio of the low-α to high-α bins' RV variability fraction alongside the ratio of median masses between the low-α and high-α bins. The second row is the same but for [α/Fe].

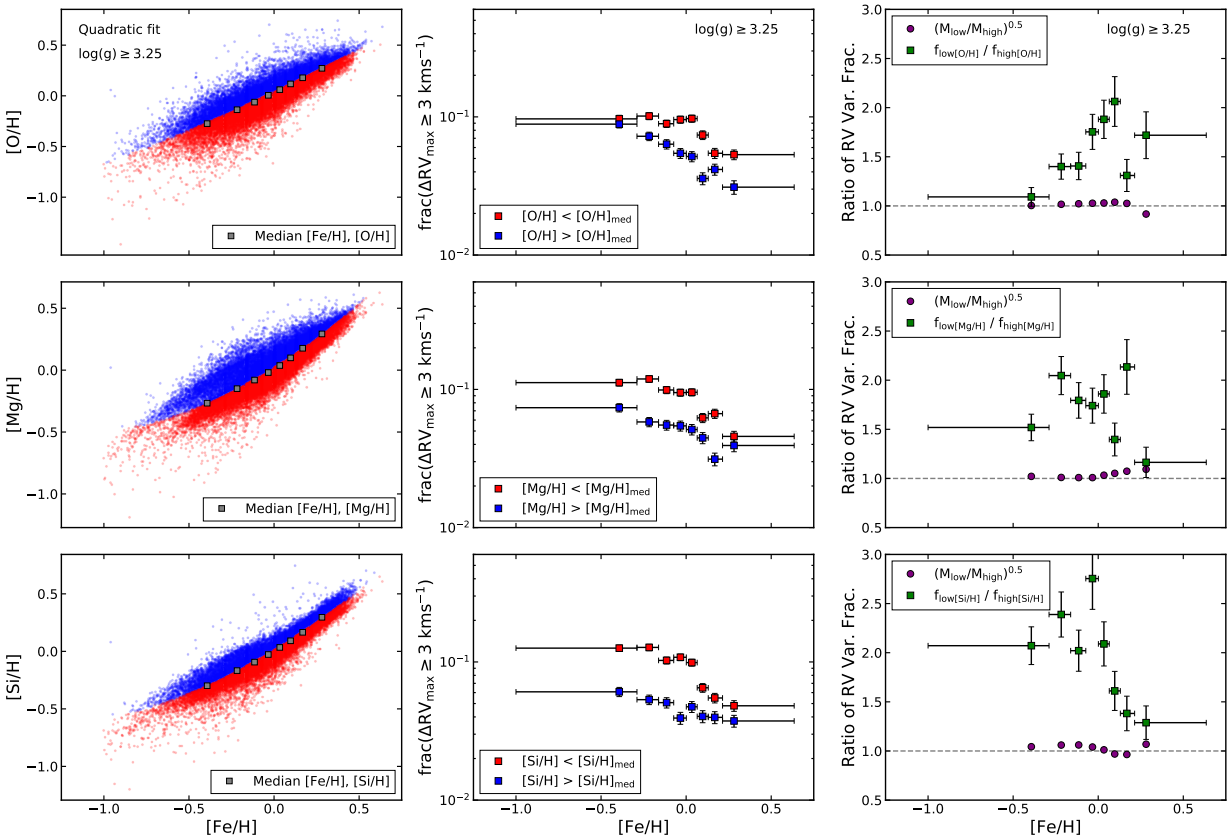

Figure 12: Same as Fig. 11, but for [O/H], [Mg/H], and [Si/H].

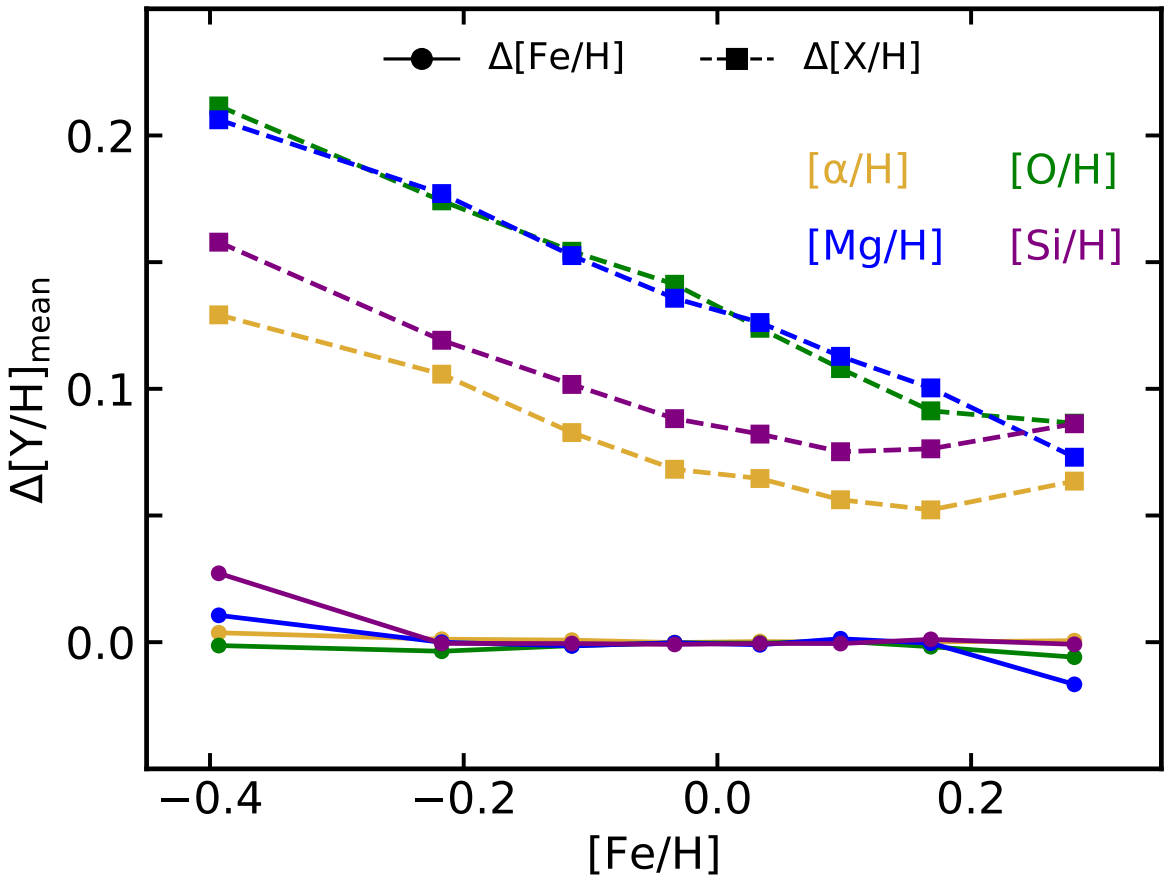

Figure 13: Differences in the mean [Y/H] for each sample, with $\Delta[\mathrm{Y/H}]_{\mathrm{mean}}$ = mean($[\mathrm{Y/H}]_{\mathrm{high}}$) − mean($[\mathrm{Y/H}]_{\mathrm{low}}$).

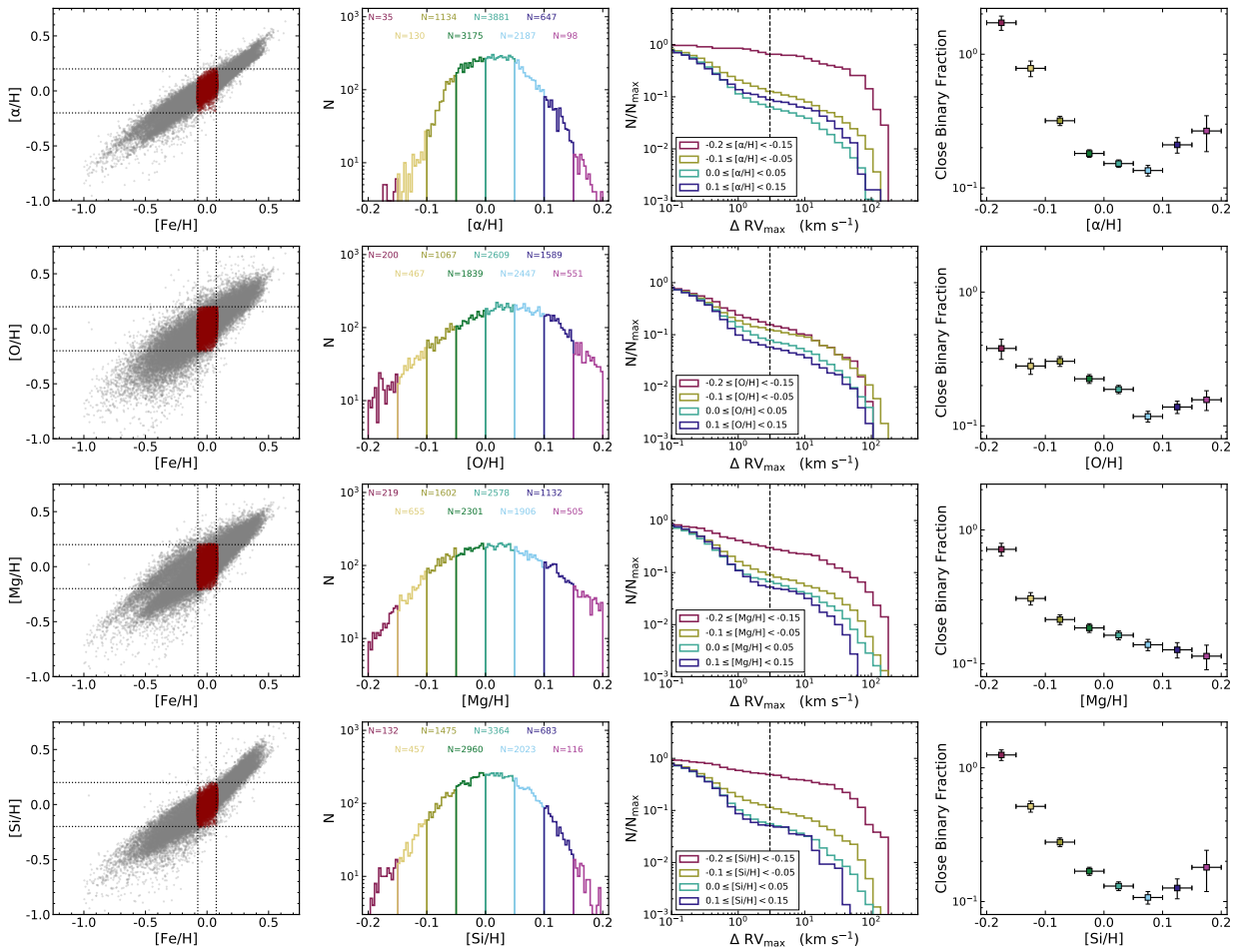

Figure 14: Various distributions for a selection of data in a narrow range around solar [Fe/H]. First row: [far left] [α/H] versus [Fe/H], where the entire sample is shown in gray and the chosen subsample is shown in dark red (boundaries $-0.075 \leq$ [Fe/H] ≤ 0.075 and $-0.2 \leq$ [α/H] ≤ 0.2); [center left] histograms for the selected data, split into eight equally spaced bins across [α/H]; [center right] selected cumulative $\Delta \mathrm{RV}_{\mathrm{max}}$ histograms; and [far right] the close binary fraction as a function of [α/H] for the selected data, color-coded by its [α/H] bin. The horizontal error bars show the [α/H] range of each bin, and the vertical error bars show the completeness-adjusted uncertainty, σ_f/c. The remaining rows are the same but for [O/H], [Mg/H], and [Si/H].

standing for each of the five parameters we study, shown in red and blue. The dividing line between low- and high-X samples is drawn using a quadratic fit to the median with a finer grid of thirty-five bins in [Fe/H]. The second column of Figs. 11-12 shows the fraction of systems with $\Delta \mathrm{RV}_{\mathrm{max}} \geq 3$ km s^{-1} for each of the low- and high-X subsamples as a function of [Fe/H]. Horizontal error bars indicate the extent of the [Fe/H] bins, and vertical error bars represent the binomial process uncertainty, σ_f (equation 2.2). The anti-correlation between [Fe/H] and close binary fraction is again present, but there is a significant gap between the low- and high-X subsamples in all five parameters we study. The green points in the third column of Figs. 11-12 display the ratio of RV variability fractions between the low- and high-X abundance subsamples, with horizontal error bars again indicating the extent of the [Fe/H] bins and vertical error bars denoting the uncertainty obtained via error propagation. This ratio is greater than one across every [Fe/H] bin and for every abundance considered here. The ratios generally increase with [Fe/H] for O, but the opposite appears to be true for Mg and Si.

These results reinforce our finding that α element abundances have a strong impact on the close binary fraction. To further investigate to what extent this effect is separate from the [Fe/H] effect, we calculated the difference in subsample means for four of the abundance measurements, defined as

$$\Delta[\mathrm{Y/H}]_{\mathrm{mean}} = \mathrm{mean}([\mathrm{Y/H}]_{\mathrm{high}}) - \mathrm{mean}([\mathrm{Y/H}]_{\mathrm{low}}) \tag{2.3}$$

where Y can be Fe or one of the α-process abundances. We plot these differences in Fig. 13, which shows that the differences in mean [Fe/H] are essentially 0 for all of the bins except the first and eighth, while the differences in mean [X/H] for α, O, Mg, and Si remain substantial, although they do decrease as [Fe/H] increases. In other words, while some systematic differences in [Fe/H] exist between the high-X and low-X samples that we have defined for the α element abundances, they are too small to account for the effect that we see. Of course, our high-X and low-X samples are not exactly comparable in every aspect, but the effect we observe is too large to be due to other (i.e., non-chemistry related) factors. To illustrate this, we also show in the third column of Figs. 11-12 the magnitude of the effect due to systematic differences in the stellar mass measured by Sanders et al. 2018 between

the high-X and low-X samples as a function of [Fe/H]. These systematic differences, while present, are again too small to explain the disparity in RV variability fraction between the low- and high-α subsamples.

Another way to disentangle the [Fe/H] and α effects is to examine trends with α abundances in a narrow range of [Fe/H] (Fig. 14). For each α abundance, we select a subset of the full sample that spans $-0.075 \leq$ [Fe/H] ≤ 0.075 and $-0.2 \leq$ [X/H] ≤ 0.2, shown in dark red in the first column of Fig. 14. We then divide this subsample into eight bins across the relevant α abundance, with histograms for each bin shown in the second column and the number of objects in each bin listed in the colored text. Cumulative $\Delta\mathrm{RV}_{\mathrm{max}}$ histograms for four of these bins are shown in the third column. The fourth column displays the completeness-corrected close binary fraction as a function of each α-process abundance measurement, with the horizontal error bars indicating the edges of the bins and the vertical error bars representing the completeness-adjusted uncertainty, σ_f/c. This analysis reveals that the close binary fraction in this narrow [Fe/H] range is clearly anti-correlated with Mg. For the other three abundances, there is a general downward trend, but the detailed behavior is more complex. For [α/H], O, and Si, it appears to reach a minimum around 0.075 dex, and then steadily increases once again. This turnaround is weakly present in O, but it is clear in [α/H] and Si. Similar to the third panel of Figs. 11-12, we compared the ratio of the median mass for each bin against the bin with the minimum close binary fraction. Across all abundances, the difference in median mass between bins is insignificant compared to the difference in observed RV variability.

We repeated this analysis for other narrow ranges of [Fe/H]. Each subsample spanned a width of Δ[Fe/H] = 0.15 dex ($\pm$0.075 from the central value) and Δ[X/H] = 0.4 dex ($\pm$0.2 from the central value). The central values we compared, in pairs of ([Fe/H], [X/H]), were (-0.4, -0.3); (-0.2, -0.2); and (0.2, 0.2) - the figures for each set are included in Appendix 2.6. The turnaround that we see in the solar [Fe/H] sample was present in some, but not all the [Fe/H] bins. These results confirm the trends seen in Fig. 10 with larger sample sizes, and show that the multiplicity statistics for stars with a specific chemistry can be quite extreme - see for instance the prominent tail in the $\Delta\mathrm{RV}_{\mathrm{max}}$ distributions corresponding to the lowest α abundances in Fig. 14. In these extreme cases, it is possible

that our assumed underlying period distribution is incorrect, which would make our derived values of the completeness corrected close binary fractions incorrect. However, our reported high fractions of RV variability are robust, and clearly require a high frequency of close binary companions, regardless of the underlying period distribution.

Finally, we note that when looking along lines of constant α abundance in Fig. 10, the binary fraction is often *positively* correlated with [Fe/H]. To verify that this is a real effect and not just a result of binning and small number statistics, we examined the cumulative chemistry distributions for both our entire sample and just the objects with $\Delta RV_{max} \geq 3$ km s^{-1}. For every α abundance measurement, the cumulative [X/H] distributions across each of the eight [Fe/H] bins used in Figs. 11-12 reveal that the RV variables are always shifted towards lower α abundances compared to the total population. Again, this confirms the general anti-correlation between close binary fraction and α abundances. We then plotted the cumulative [Fe/H] distributions for six bins of equal width across $-0.8 \leq$ [X/H] < 0.4. For the first three bins ($-0.8 \leq$ [X/H] < -0.2), the RV variables are shifted towards *higher* [Fe/H] abundances than the total population. This is true for all α abundances considered here. However, the cumulative metallicity distributions for the two bins between $-0.2 \leq$ [X/H] < 0.2 generally show a weakening of this trend, and the bin for $0.2 \leq$ [X/H] < 0.4 shows a reversal–i.e., the RV variables are shifted towards *lower* [Fe/H] than the greater population. These results lend support for a inflection point in the close binary fraction as a function of α abundances around 0.1 dex.

To summarize our findings, we find a robust anti-correlation between α abundances and close binary fraction, similar in strength but separate from the already established anti-correlation with [Fe/H]. The general trend of increasing α abundances to decrease the close binary fraction is robust, but the details are complex, and it is likely that the effect is not completely independent from [Fe/H], at least in some regimes. Because of this, it might not be possible to provide a simple quantitative description of the full relationship between stellar chemistry and close binary fraction in the APOGEE sample.

2.3 Discussion

In Section 2.2 we have shown that the relationship between stellar multiplicity and stellar parameters is quite complex. A robust physical interpretation of the observed anti-correlation between α-process abundances and close binary fraction thus requires careful consideration of potential systematics and internal correlations. In this section, we address two such effects that were not discussed in Sections 2.2.2 and 2.2.3, and we consider the implications that our results have for star formation.

2.3.1 Potential Systematics

Visit Histories Most of our targets have sparsely sampled RV curves. Among the non-SB2s, 36 per cent of objects have only two visits, and 43 per cent have three. For the suspected SB2s, 43 per cent, 35 per cent, and 22 per cent having 2, 3, and 4+ visits, respectively. This is expected; as discussed in Sec. 2.1, fitting a single stellar template to an SB2 can bias the fit parameters (K. El-Badry et al. 2018) and also result in poorer fits overall, which are then flagged in the various APOGEE bitmasks. Because we make quality cuts on these bitmasks, we expect that fewer SB2 visits might pass our quality cuts than the overall sample, though we emphasize that our stringent cuts in S/N are still in place. In both cases, objects with duplicate `allStar` entries (as discussed in the first paragraph of Sec. 2.1) are biased towards more visits ($\sim$65 per cent with 4+ visits) and longer baselines than non-duplicated APOGEE IDs. For each [Fe/H] bin used in Figs. 11-12, we compared the low- and high-α subsamples across histograms of the baselines, $\mathrm{JD}_N - \mathrm{JD}_1$; the median of the time lags between visits for each star, $\mathrm{median}(\mathrm{JD}_{i+1} - \mathrm{JD}_i)$; and the mean of the time lags between visits for each star, $\mathrm{mean}(\mathrm{JD}_{i+1} - \mathrm{JD}_i)$, where JD is the Julian date of each observation for a star with N total visits. There does not appear to be any significant variation in these parameters with [Fe/H] or α abundances. The fractions of stars with 2, 3, and 4+ visits for each [Fe/H] bin and low- and high-α subsample are also consistent with those for the entire sample.

White Dwarf Pollution Some portion of our sample may be post-common envelope

systems with white dwarf companions, rather than two MS stars or a subgiant-MS pair. The fraction of these systems will vary with the age of the stellar population, but for short-period ($\log(P/\text{days}) \leq 4$), it is $\sim$ 15 per cent at 1 Gyr and $\sim$ 30 per cent at 10 Gyr (Moe and Di Stefano 2017, see their Section 8.3 and Fig. 29). Considering our median sample age $\tau \sim 8$ Gyr, we expect a fraction of roughly 25 per cent white dwarf companions in our sample. This fraction will also depend upon the metallicity of the stars, but it cannot explain the factor of 1.5-2 difference we see in the close binary fractions of high-α and low-α samples.

2.3.2 Implications for Binary Star Formation

Close binaries ($a < 10$ au) likely formed via fragmentation, accretion, and inward migration in the disk, whereas wide binaries ($a > 200$ au) probably formed via fragmentation of molecular cores (Fisher 2004; K. Kratter et al. 2016; Moe and Di Stefano 2017; Tokovinin 2017; Tokovinin and Moe 2020). Fragmentation of molecular cores is relatively insensitive to opacity (Bate 2014), explaining why both the initial mass function (Kroupa et al. 2013) and wide binary fraction beyond a ¿ 200 au (Kareem El-Badry and Rix 2018; Moe, Kaitlin M. Kratter, and Badenes 2019) are metallicity invariant across -1.0 ¡ [Fe/H] ¡ 0.5. A natural consequence of such a model is that the close binary fraction increases with primary mass because massive protostellar disks are more prone to fragmentation (Kaitlin M. Kratter and Matzner 2006). Analytical models and hydrodynamic simulations also show that the propensity for disk fragmentation decreases with metallicity due to two compounding effects (Machida et al. 2009; Moe, Kaitlin M. Kratter, and Badenes 2019; Tanaka et al. 2014). First, optically thin cores on large spatial scales radiate via molecular transitions, and so metal-poor cores are systematically hotter and must achieve higher masses in order to collapse into disks. The systematically higher core masses toward lower metallicities do however lead to higher accretion rates onto the disks, promoting gravitational instability (Machida et al. 2009). Second, for solar abundances, protostellar disks massive enough to undergo gravitational instability are optically thick (Clarke 2009; Kaitlin M. Kratter, Murray-Clay, et al. 2010; Rafikov 2005). Decreasing the disk's metallicity decreases its optical depth, allowing the mid-plane to radiate and cool more effectively, stimulating disk fragmentation (Moe,

Kaitlin M. Kratter, and Badenes 2019; Tanaka et al. 2014). Note that Bate 2019 has posited a more complex explanation for the increased close binary fraction at low metallicity. While some increase in disk fragmentation is observed in the simulations, ibid. also observes that metal poor cores fragment on very small scales, where the gas is also optically thick. Moreover, due to the very high rate of dynamical interactions observed in these simulations, far more interchanges between core fragmentation and disk fragmentation binaries are observed. The initial conditions in such simulations may not be representative of lower density star clusters in the solar neighborhood.

We confirm that the close binary fraction decreases with [Fe/H], consistent with previous observational surveys and theoretical models. Moreover, we demonstrate for the first time that the close binary fraction decreases more rapidly with α than Fe for $[\alpha/\mathrm{Fe}] < 0.05$ dex, consistent with expectations from the two compounding effects described above. For example, optically thin cores radiate mainly through molecular CO transitions, and so the infall rates onto the disk are mainly set by α abundances. In the cold ($T < 150K$) midplane of disks prone to fragmentation, opacities are dominated by dust and in particular ice covered grains, which can comprise roughly 60 per cent of the solid particles volume; refractory organics are the second most important contributor in this regime (Semenov et al. 2003). While the optical properties of grains still depend on the distribution and topology of Fe, the changing abundances of O and Si will play a larger role in the bulk opacity. The disk's temperature profile and probability of fragmentation is therefore more dependent on α abundances, explaining why the close binary fraction is anti-correlated with O and Si to a larger degree than with Fe.

For $[\alpha/\mathrm{Fe}] > 0.05$ dex, a different picture emerges whereby the close binary fraction within $a < 10$ au flattens to 10 per cent, independent of chemical abundance. This "floor" of a 10 per cent close binary fraction appears to be universal. For example, although the close binary fraction increases from 15 per cent for K-dwarfs to 30 per cent for A-dwarfs, the close binary fraction of both M-dwarfs and brown dwarfs is 10 per cent, relatively constant across $M_1 = 0.05$ - $0.6\,\mathrm{M}_\odot$ (Joergens 2008; Moe 2019; Moe and Di Stefano 2017; Murphy et al. 2018; Winters et al. 2019). One possible explanation is that at least 10 per cent of protostellar disks become massive or cool enough to fragment early in their accretion evolution, regardless of

their chemical composition or the final primary mass. Another possibility is that metal-rich and/or low-mass disks are entirely unsusceptible to fragmentation, and the floor of a 10 per cent close binary fraction is actually due to the small fraction of cores that fragment on large scales and subsequently decay to $a < 10$ au via dynamical friction or exchange interactions (Bate 2019; A. T. Lee et al. 2019). In the future, measurements of how the close binary fraction of M-dwarfs changes with Fe and α will help differentiate between these two scenarios.

Another consequence of these metallicity trends is that the overall companion distribution becomes skewed towards shorter separations with decreasing metallicity (see Fig. 19 in Moe, Kaitlin M. Kratter, and Badenes 2019). However, based on the DR13 sample of SDSS-APOGEE RV variables and *Kepler* eclipsing binaries, ibid. found that the separation distribution of solar-type binaries across $a = 0.02$ - 10 au does not vary with metallicity at a statistically significant level. With our larger DR14 sample of SDSS-APOGEE RV variables, we find that α-poor binaries are skewed toward larger $\Delta \mathrm{RV}_{\mathrm{max}}$ and thus shorter separations. With decreasing metallicity, models suggest that disks are not only more likely to fragment, but that disk fragmentation occurs at smaller separations (Machida et al. 2009; Moe, Kaitlin M. Kratter, and Badenes 2019). For example, Fig. 10 of Machida et al. 2009 shows that fragmentation occurs near 200 au at solar-metallicity but near 1 au for Population III stars. Similarly, according to Fig. 20 of Moe, Kaitlin M. Kratter, and Badenes 2019, disks with solar-metallicity are stable within $a < 30$ au, but metal-poor disks with $\mathrm{Z} = 10^{-3}$ $\mathrm{Z}_{\odot}$ are capable of fragmentation near $a = 8$ au. Our measurements are qualitatively consistent with these models, demonstrating that α-poor stars not only have a higher close binary fraction, but that those close binaries are skewed toward shorter separations. Note that at very low metallicities, one might expect the relative importance of Fe vs α elements to shift; if fragmentation is pushed to closer separations and correspondingly higher temperatures, the relative importance of ices and organics decreases, and the overall iron abundance might become more important (Semenov et al. 2003).

2.4 Conclusions

We have presented an analysis of the complex relationship between stellar multiplicity and stellar parameters, with an emphasis on the trends for various α-process abundances. We defined a sample of 41,363 dwarf and subgiant stars from APOGEE DR14 with well-measured stellar parameters and at least 2 RV measurements. Because most objects in our sample have sparsely-sampled RV curves, we applied a threshold on the maximum RV shift, $\Delta\mathrm{RV}_{\mathrm{max}} \geq 3$ km s^{-1}, to calculate a fraction of RV variables. This fraction is a tracer for the close binary fraction, modulo a completeness correction that can be estimated for the APOGEE observing epochs using a Monte Carlo method with an assumed period distribution. We analyzed these completeness-corrected close binary fractions alongside a variety of stellar parameters: T_{eff}, M, [Fe/H], [Mg/H], [Si/H], τ, J_z, and v_R. We report a strong anti-correlation between the close binary fraction and Mg and Si abundances, similar in strength but separate from the known anti-correlation with [Fe/H]. Other stellar parameters like T_{eff} and M also have an impact on the close binary fraction, but chemical composition is clearly the main driver of multiplicity trends in our APOGEE sample.

We further investigated the relationship between [Fe/H], α-process abundances, and stellar multiplicity, measuring a slightly steeper anti-correlation between [Fe/H] and the close binary fraction across the narrower interval $-0.4 \leq$ [Fe/H] ≤ 0.3 than the average slope across $-1.0 \leq$ [Fe/H] ≤ 0.5 reported by Moe, Kaitlin M. Kratter, and Badenes 2019, similar to the trend found by Kareem El-Badry and Rix 2018. The observed anti-correlations between the close binary fraction and α-process abundances (α, O, Mg, Si) are [Fe/H]- and abundance-dependent in strength and consistency. Mg and Si in particular showed exceptionally large close binary fractions and remarkable $\Delta\mathrm{RV}_{\mathrm{max}}$ distributions, where the cores almost disappeared entirely. We also find evidence for a correlation *and* anti-correlation between the close binary fraction and [α/H] and [Si/H] with a narrow range of our parameter space. The anti-correlation between stellar composition and close multiplicity fraction has a basis in stellar formation theory. However, low-α binaries are also expected to be skewed towards shorter separations, which would also result in an excess of RV variables independent of an increase in the close binary fraction. Future studies of the period distribution as a

function of metallicity and chemistry will help clarify the magnitude of these two effects within our measurements.

2.5 Choices for the Monte Carlo Simulation

We altered several of the choices listed in Sec. 2.2.1 to gauge their effects on the completeness estimate. The first is our choice of $\log(g)$; it only affects the calculations for the critical period $P_{\rm crit}$ and circularization period $P_{\rm circ}$ (Badenes, C. Mazzola, et al. 2018). The critical period is calculated using

$$P_{\rm crit} = \frac{2\pi}{\sqrt{R^3(q)(1+q)}}\Big(\frac{GM}{g^3}\Big)^{1/4} \tag{2.4}$$

where M is the mass of the primary in grams, g is the primary's surface gravity in cm s^{-2}, q is the system's mass ratio, and $R(q)$ is the ratio between the radius of the Roche Lobe and the orbital separation (Eggleton 1983). The circularization period is calculated for $\log(g/\text{cm s}^{-2})= 4.25$, $M = 1.0\text{M}_\odot$, and [Fe/H]=0.0 dex. For $1M_\odot$ and $\log(g/\text{cm s}^{-2})= 4.25$, we calculate $\log(P_{\rm circ}/\text{days}) = 0.888$ and $\log(P_{\rm crit}/\text{days}) = -0.313$. Running the MC with 2x and 0.5x these values resulted in no significant change to the completeness estimate, which is expected; given the Raghavan et al. 2010 period distribution, very few stars will be at short enough periods to be affected by shifts of this magnitude in either of these parameters.

We implemented a 25 per cent increase in twins ($0.95 \geq q \geq 1.0$) motivated by the results of Moe and Di Stefano 2017. Reducing this fraction, even to 0 per cent, did not significantly change our completeness estimate.

Fully characterizing the observed RV uncertainty distribution is a difficult task, especially given the diverse nature of our sample. Consequently, our choice for a simulated RV error distribution is not motivated by physical intuition; rather, we have tried a variety of possible distributions and distribution parameters in order to roughly reproduce the shape of the observed $\Delta\text{RV}_{\rm max}$ distribution. We have found the Student's t distribution to reproduce the relative shape of the core and tail for a variety of $\log(g)$ values, and so we chose to use it in the completeness estimate described in Section 2.2.1. This choice does not significantly

affect our completeness estimates, however. Table 3 gives completeness fractions given two $\Delta\mathrm{RV}_{\mathrm{max}}$ thresholds for three RV error distributions:

1. a Student's t (scipy.stats.t) with degrees of freedom 3.5, $\mu = 0.0$, $\sigma = 0.25$ km s^{-1} (the same used in Section 2.2)
2. a Gaussian (scipy.stats.norm) with $\mu = 0.0$, $\sigma = 0.25$ km s^{-1}
3. a constant RV error of $\sigma_{\mathrm{RV}} = 0.25$ km s^{-1} applied to every simulated RV

The simulated $\Delta\mathrm{RV}_{\mathrm{max}}$ distribution for each choice are shown alongside the observed distribution in Fig. 15. The completeness fractions are nearly identical between the Student's t and the Gaussian, and while the Student's t has a larger percentage of false positives, it is still a modest increase. The constant RV uncertainty has very similar detection efficiencies to the other two at the low-P end, where the RV variability is the largest. As expected, it diverges for larger periods, where it fails to distinguish between a core and tail in the $\Delta\mathrm{RV}_{\mathrm{max}}$ distribution, apparent in Fig. 15. Between the Student's t and Gaussian, the $\Delta\mathrm{RV}_{\mathrm{max}}$ distributions are qualitatively similar. The Gaussian is slightly narrower with a sharper transition between the core and tail, whereas the Student's t has a slightly better match to the overall shape of our observed $\Delta\mathrm{RV}_{\mathrm{max}}$ distribution. For this reason, we chose the Student's t, though we note that this reason is purely qualitative and our choice does not significantly affect the completeness fractions. Future work to better understand the RV uncertainties may favor one distribution over another, but that is beyond the scope of this work.

From theoretical predictions (see Section 2.3.2) and recent observations of eclipsing binaries (Jayasinghe et al. 2021), the period distribution for solar-type binaries may depend on chemistry. We briefly explored this scenario by implementing a three-component period distribution. Motivated by Fig. 19 of Moe, Kaitlin M. Kratter, and Badenes 2019, we simulated a sample of $N = 50,000$ stars using three chemistry-dependent log-normal period distributions:

1. $-1 \leq [\mathrm{Fe/H}] \leq -0.2$: $\{\mu_{\log(P/\mathrm{days})} = 4.0, \sigma_{\log(P/\mathrm{days})} = 1.5\}$
2. $-0.2 \leq [\mathrm{Fe/H}] \leq 0.2$: $\{\mu = 5.0, \sigma = 2.0\}$
3. $[\mathrm{Fe/H}] \geq 0.2$: $\{\mu = 6.0, \sigma = 2.5\}$

Table 3: Completeness and false positive fractions for selected $\log(P/\text{days})$ and $\Delta\text{RV}_{\text{max}}$ thresholds, given three RV error distributions all with $\sigma = 0.25$ km s^{-1}.

	$\Delta\text{RV}_{\text{max}} \geq 1$ km s^{-1}			$\Delta\text{RV}_{\text{max}} \geq 3$ km s^{-1}		
$\log(P/\text{days})$ threshold	t3.5	Gaussian	Constant	t3.5	Gaussian	Constant
$\log P \leq 0.0$	1.00	1.00	1.00	0.96	0.97	1.00
$\log P \leq 2.0$	0.93	0.94	0.93	0.84	0.84	0.85
$\log P \leq 4.0$	0.55	0.50	0.64	0.34	0.34	0.47
False Positive Fraction	2.68%	1.20%	0.0%	0.10%	0.0%	0.0%

where [Fe/H] values are given in dex. We simulated $N_1 = 6,250$, $N_2 = 37,500$, $N_3 = 6,250$, which is proportional to the number of stars in our sample within those [Fe/H] ranges. The calculated completeness fractions for each MC subsample do not vary significantly from those shown in Table 1, and when we combine the subsamples into a single $N = 50,000$ sample, the calculated completeness fractions also do not vary significantly. Changing the subsample sizes to $(15,000; 20,000; 15,000)$ also did not result in significantly different completeness fractions.

2.6 Additional Figures

2.7 Format of Data Products

Here, we make available the likely SB2s identified by two methods as discussed in Sec. 2.1. Table 4 describes the column structure, and Tables 5-6 provide the results from each method. Each entry in Tables 5-6 is for an individual visit spectrum; the table from re-analyzing APOGEE CCFs has 13,970 total entries, and the table from re-calculating the CCFs has 12,044. There are 2832 and 2238 unique APOGEE IDs in each table, respectively.

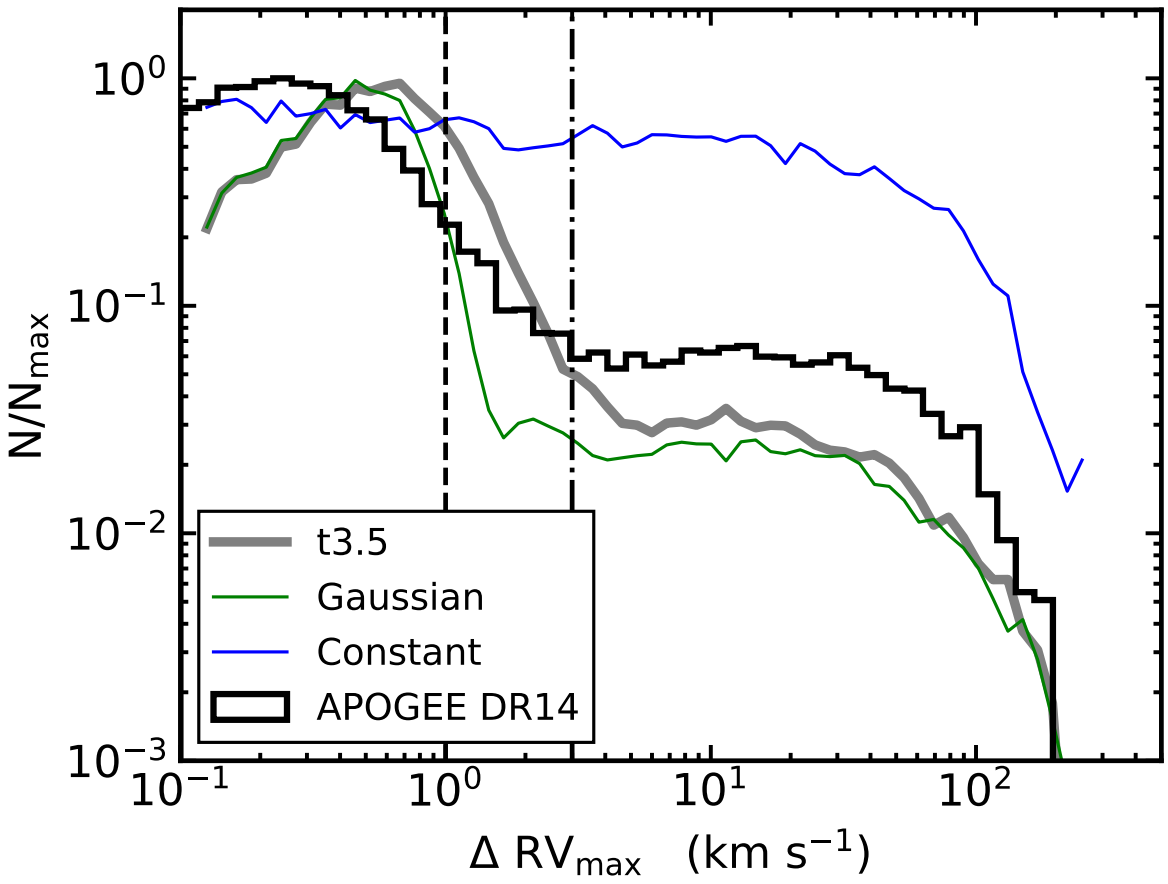

Figure 15: Distributions of ΔRV_{max} from our APOGEE DR14 sample (black) and simulated by our MC with three RV error distributions. All three RV error distributions have $\sigma = 0.25$ km s^{-1}, and the Gaussian and Student's t with degrees of freedom 3.5 (t3.5) both have $\mu = 0$.

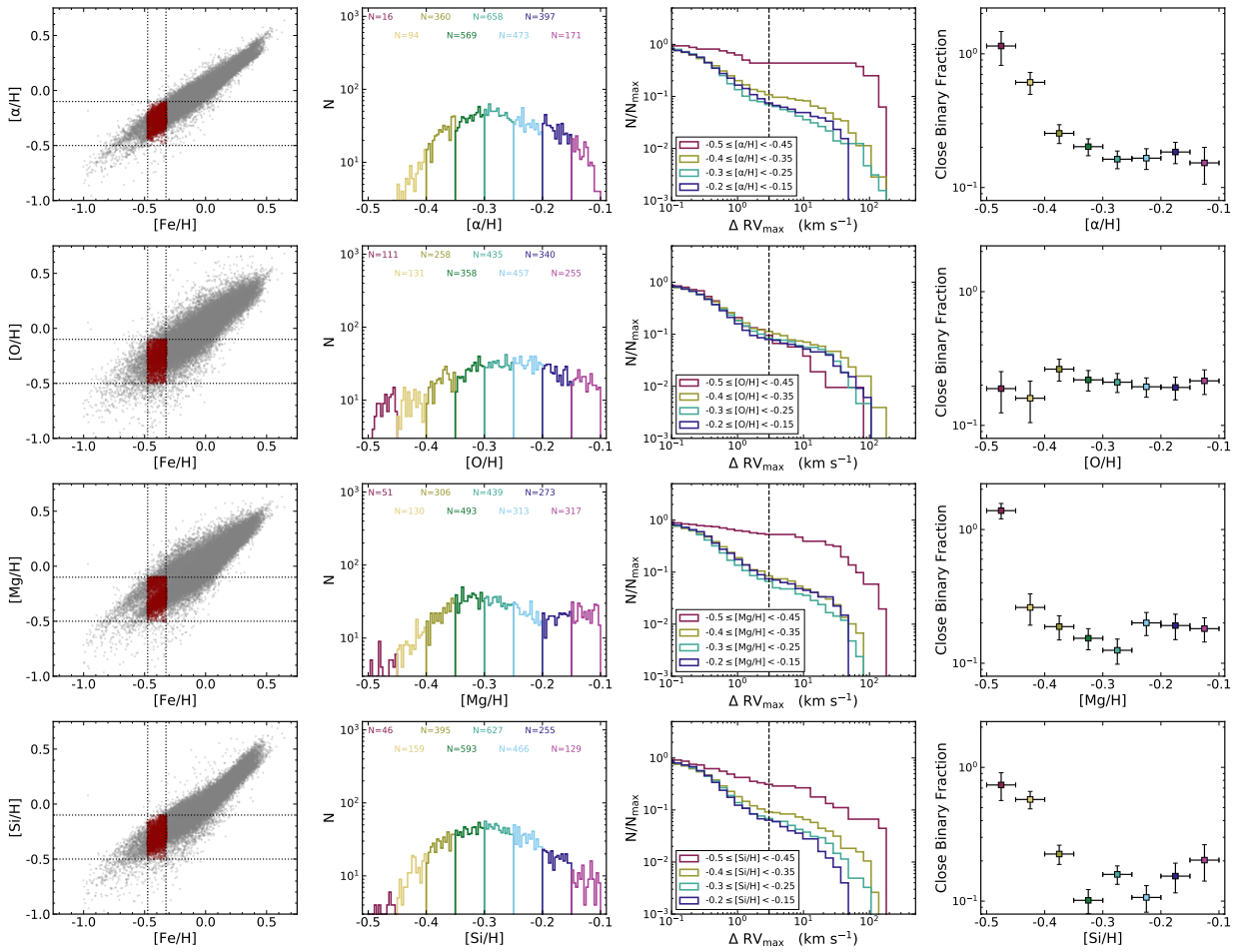

Figure 16: Identical to Fig. 14 but with boundaries $-0.475 \leq$ [Fe/H] ≤ -0.325 and $-0.5 \leq$ X ≤ -0.1.

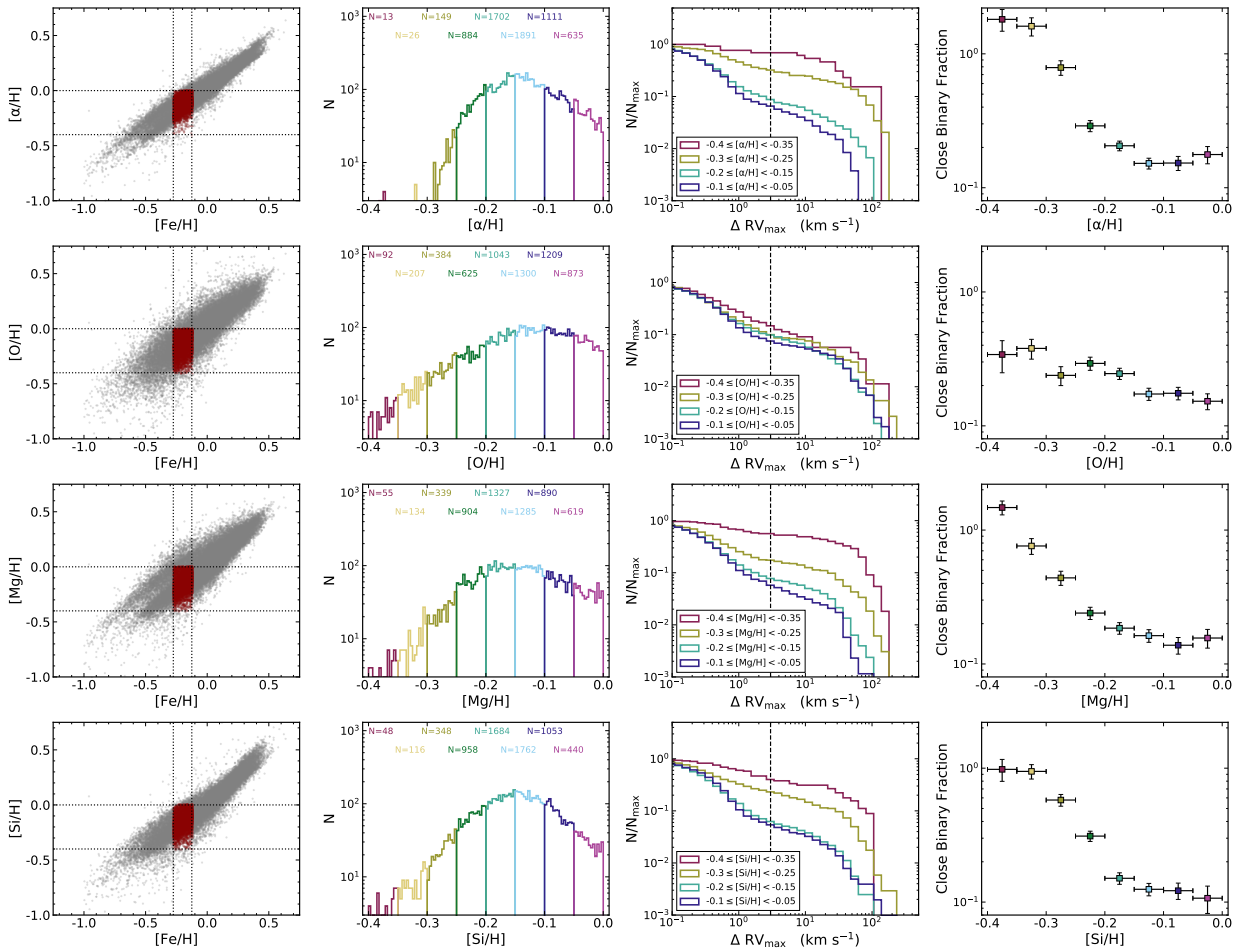

Figure 17: Identical to Fig. 14 but with boundaries $-0.275 \leq$ [Fe/H] ≤ -0.125 and $-0.4 \leq$ X ≤ 0.0.

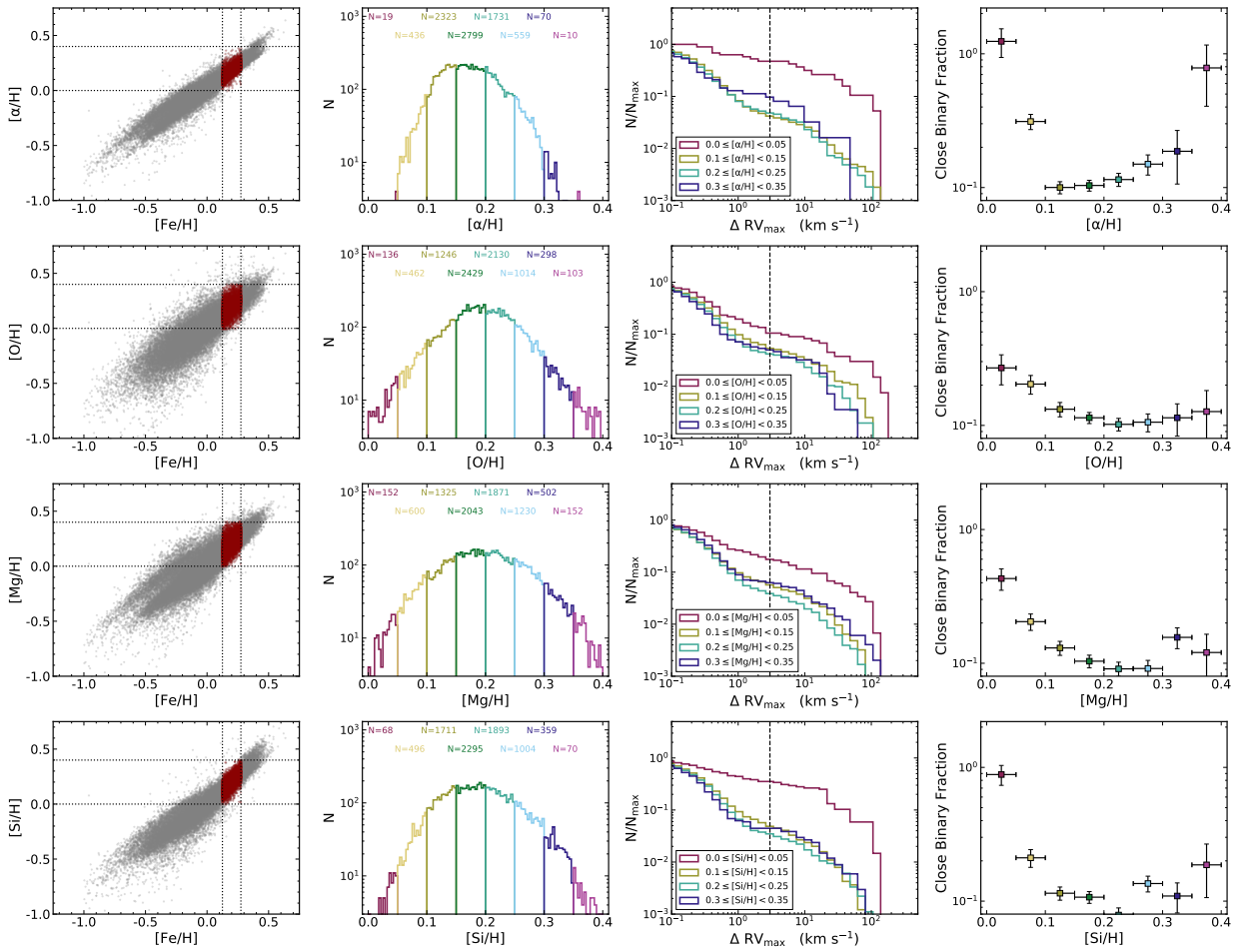

Figure 18: Identical to Fig. 14 but with boundaries $0.125 \leq$ [Fe/H] ≤ 0.275 and $0.0 \leq$ X ≤ 0.4.

Table 4: Format of provided SB2 catalogs. Listed below are the name of each column with a description and any applicable units. For each entry that is given by an array, the array has 8 elements.

Name	Description	Units
OBJID	identifier in the APOGEE catalog	—
PLATE	APOGEE visit plate ID	—
FIBER	APOGEE visit fiber ID	—
MJD	Modified Julian Date of APOGEE visit	—
N	number of deconvolved components	—
FLAG	array of integer quality flags, from 1.0 to 4.0	—
POS	array of RVs for each component, ordered by amplitude	km s^{-1}
AMP	array of amplitudes	—
FWH	array of full widths at half maximum	km s^{-1}
EPOS	array of RV uncertainties	km s^{-1}
EAMP	array of amplitude uncertainties	—
EFWH	array of full width at half maximum uncertainties	km s^{-1}

Table 5: Table of likely SB2s identified by re-analyzing the APOGEE CCFs. This table is available in its entirety (with parameters for 13,970 visits with 2832 unique APOGEE IDs) in machine-readable form.

OBJID	PLATE	FIBER	MJD	N	FLAG	POS	AMP	FWH	EPOS	EAMP	EFWH
2M00023036+8524194	7950	224	57295	1	4.0 ... 0.0	−4.5720005 ... nan	0.5707569 ... nan	49.42374 ... nan	0.57283086 ... nan	0.013487913 ... nan	1.3489138 ... nan
2M00023036+8524194	9084	224	57556	2	4.0 ... 0.0	−71.81711 ... nan	0.37271407 ... nan	34.15913 ... nan	0.546208 ... nan	0.012155449 ... nan	1.2862214 ... nan
2M00023179+1521164	6560	77	56584	2	4.0 ... 0.0	20.618723 ... nan	0.49165606 ... nan	54.235355 ... nan	1.8823811 ... nan	0.014511261 ... nan	3.0066836 ... nan
2M00023179+1521164	6560	89	56588	1	4.0 ... 0.0	3.9876366 ... nan	0.54505944 ... nan	62.63368 ... nan	0.6144675 ... nan	0.010904319 ... nan	1.4469602 ... nan
...	...	...	...	...	...	...	...	...	...	...	...

Table 6: Table of likely SB2s identified by calculating our own CCFs. This table is available in its entirety (with parameters for 12,044 visits with 2238 unique APOGEE IDs) in machine-readable form.

OBJID	PLATE	FIBER	MJD	N	FLAG	POS	AMP	FWH	EPOS	EAMP	EFWH
2M00023036+8524194	5095	233	55821	2	4.0 ... 0.0	50.38858 ... nan	0.3384734 ... nan	33.308804 ... nan	0.51698554 ... nan	0.010713303 ... nan	1.217408 ... nan
2M00023036+8524194	5095	230	55824	2	4.0 ... 0.0	−74.34177 ... nan	0.32860735 ... nan	31.727573 ... nan	0.54551804 ... nan	0.011521589 ... nan	1.2845968 ... nan
2M00023036+8524194	5095	230	55840	2	4.0 ... 0.0	66.387726 ... nan	0.29461184 ... nan	20.609297 ... nan	0.94517577 ... nan	0.027554285 ... nan	2.2257187 ... nan
2M00023036+8524194	5095	239	55844	2	4.0 ... 0.0	42.22613 ... nan	0.31082585 ... nan	24.475822 ... nan	0.5241617 ... nan	0.013574529 ... nan	1.2343063 ... nan
...	...	...	...	...	...	...	...	...	...	...	...

3.0 The Interplay of Stellar Evolution, Rotation, and Multiplicity

Stellar multiplicity plays a crucial role in stellar astrophysics, with roughly half of the solar-type stars in the solar neighborhood being part of multi-star systems (Duquennoy et al. 1991; Raghavan et al. 2010). In cases where these stars get close enough to interact, they can be responsible for a whole host of astrophysical phenomena, ranging from low- and high-mass X-ray binaries, Type Ia SNe, many core-collapse SNe, novae, cataclysmic variables, and the majority of stellar sources of gravitational waves (see De Marco et al. 2017, for a review). Most of these phenomena arise from the interplay between stellar evolution and multiplicity. Data from astrometric surveys now makes it possible to study stellar multiplicity across the Hertzsprung-Russell diagram, and as a function of many stellar properties (Belokurov et al. 2020; C. N. Mazzola et al. 2020; A. M. Price-Whelan, Hogg, Rix, Beaton, et al. 2020), though spectroscopy remains the best way to identify and characterize the close ($\log(P/\mathrm{d}) \lesssim 4$), unresolved binaries that are the progenitors of interacting systems. Luckily, modern spectroscopic surveys have already collected the necessary data for large samples of stars within the Milky Way.

One such survey is the Apache Point Observatory Galactic Evolution Experiment 2 (APOGEE-2; Majewski et al. 2017), a component of the Sloan Digital Sky Survey IV (SDSS-IV; Blanton et al. 2017; Gunn et al. 2006). APOGEE-2 has two high-resolution ($R \sim 22500$), multiplexed infrared spectrographs (Wilson et al. 2019), deployed in the northern and southern hemispheres, that have taken multi-epoch data for hundreds of thousands of stars representative of every major component in our Galaxy. Spectral parameters are determined via the the APOGEE Stellar Parameter and Chemical Abundances Pipeline (ASPCAP; García Pérez et al. 2016; Jönsson, Holtzman, et al. 2020), and precise radial velocities (RVs) are calculated for each individual visit spectra (Nidever et al. 2015). Though most APOGEE-2 stars only have sparsely-sampled RV curves, a large number of such curves can effectively constrain stellar multiplicity statistics and their correlation with a number of spectroscopic parameters (Badenes and Maoz 2012; Maoz et al. 2012; Sana et al. 2012).

Badenes, C. Mazzola, et al. 2018 and A. M. Price-Whelan, Hogg, Rix, Beaton, et al.

2020 found a strong relationship between the close binary fraction and the surface gravities measured by APOGEE, $\log(g/\mathrm{cm\ s^{-2}})$, which is an observational proxy for the evolutionary stage of stars. Both studies observed a positive correlation between the close binary fraction and $\log(g)$, and measured a low fraction of close binaries for red clump (RC) stars. These results agree with the expectation that companion engulfment occurs at longer and longer periods as the primary ascends the red giant branch (RGB), resulting in the gradual attrition of short-period companions until stars reach the tip of the red giant branch (TRGB). The end product of this process is a small fraction (a factor of $\sim$2 fewer) of close binaries for core-He burning stars in the RC. The shortest possible orbital period for a given system should correspond to the critical period for Roche Lobe overflow (RLOF),

$$\mathrm{P_{crit}} = \frac{2\pi}{\sqrt{\mathcal{R}^3(q)(1+q)}} \left(\frac{GM}{g^3}\right)^{1/4} \tag{3.1}$$

where g is the surface gravity and M the mass of the primary, $q = M_2/M$ is the system's mass ratio, and $\mathcal{R}(q)$ is the ratio between the radius of the Roche Lobe and orbital separation (Eggleton 1983). Values for $\mathrm{P_{crit}}$ for several evolutionary stages are shown in Fig. 19, together with with the lognormal period distribution measured by Raghavan et al. 2010 for Sun-like dwarfs in the Solar neighborhood. The top axis shows the maximum observable RV shift for a given system: its peak-to-peak RV amplitude, which is twice the semi-amplitude K and given by

$$\Delta\mathrm{RV_{pp}} = 2K = \frac{2}{\sqrt{1-e^2}} \left(\frac{\pi GM}{2\mathrm{P_{orb}}}\right)^{1/3} \sin(i_{\mathrm{orb}}) \tag{3.2}$$

where e is the eccentricity, M is the primary's mass, $\mathrm{P_{orb}}$ is the orbital period of the system, and i_{orb} is the inclination angle of the orbital axis.

Short-period systems can interact in a variety of ways before mass transfer or companion engulfment occurs. Tidal dissipation in close binaries will lead to rotational synchronization, equalizing the orbital period and the rotation periods, as well as orbital circularization, though the mechanisms for dissipation differ between early and late type stars (see Mazeh 2008; Zahn 2008). There is a clear "circularization period" in close binaries, below which orbital eccentricities are usually very small (see A. M. Price-Whelan and Goodman 2018, and references therein), and which varies with $\log(g)$. Rotational synchronization timescales are

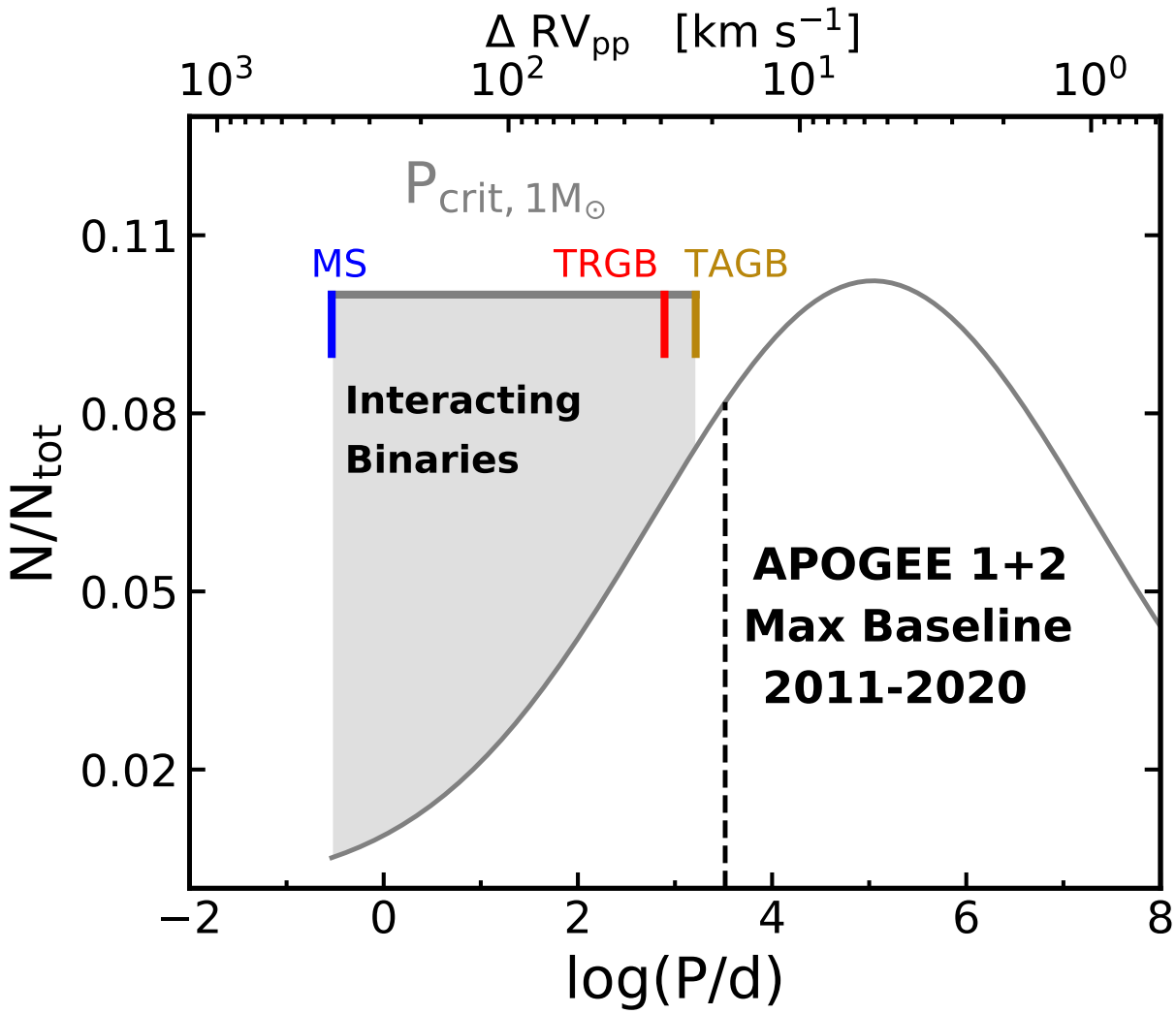

Figure 19: The Raghavan et al. 2010 lognormal period distribution ($\overline{\log \mathrm{P}} = 5.04$, $\sigma_{\log \mathrm{P}} = 2.28$) for Sun-like MS stars in the solar neighborhood. Values of $\mathrm{P}_{\mathrm{crit}}$ (equation 3.1) are indicated for a 1 $\mathrm{M}_\odot$ [Fe/H] = 0 star in an equal-mass ($q = 1$) binary across several important evolutionary points. The top axis shows $\Delta\mathrm{RV}_{\mathrm{pp}}$ (equation 3.2) for a 1 $\mathrm{M}_\odot$ star in an $e = 0$, $i_{\mathrm{orb}} = 90°$ binary across the range of periods shown.

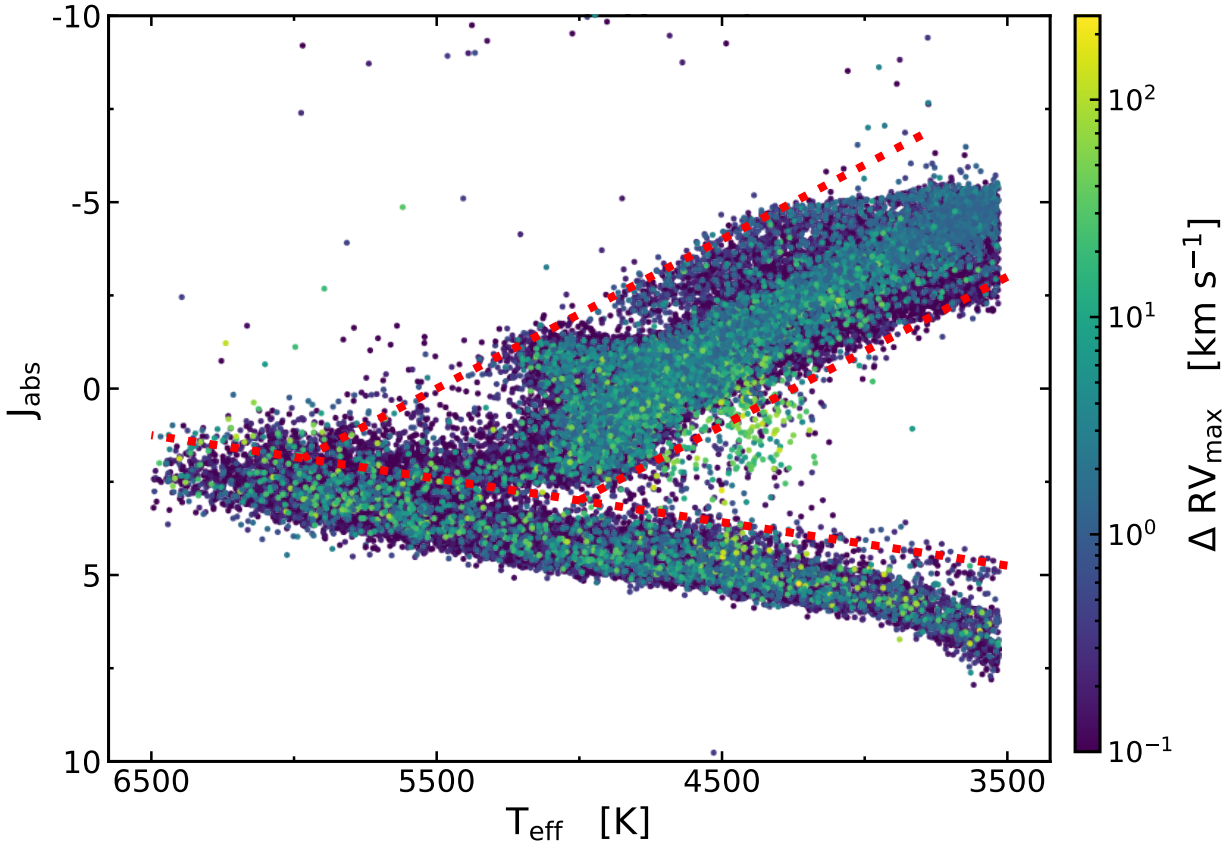

Figure 20: An HR diagram for stars passing our quality cuts using APOGEE DR14 uncalibrated $T_{\rm eff}$ and absolute 2MASS J magnitude, calculated using the Sanders et al. 2018 distance estimates. Points are colored by the ΔRV$_{\rm max}$ colorbar at right. Stars with ΔRV$_{\rm max}>$ 1km s^{-1} are shown on top for clarity and are present across the entire range of the HR diagram, meaning we are sensitive to binaries across all evolutionary points and metallicities. The dotted red lines indicate the regions we use to define our "red giant" and "dwarf" samples. These cuts retain the sequence of photometric binaries seen above the primary main sequence.

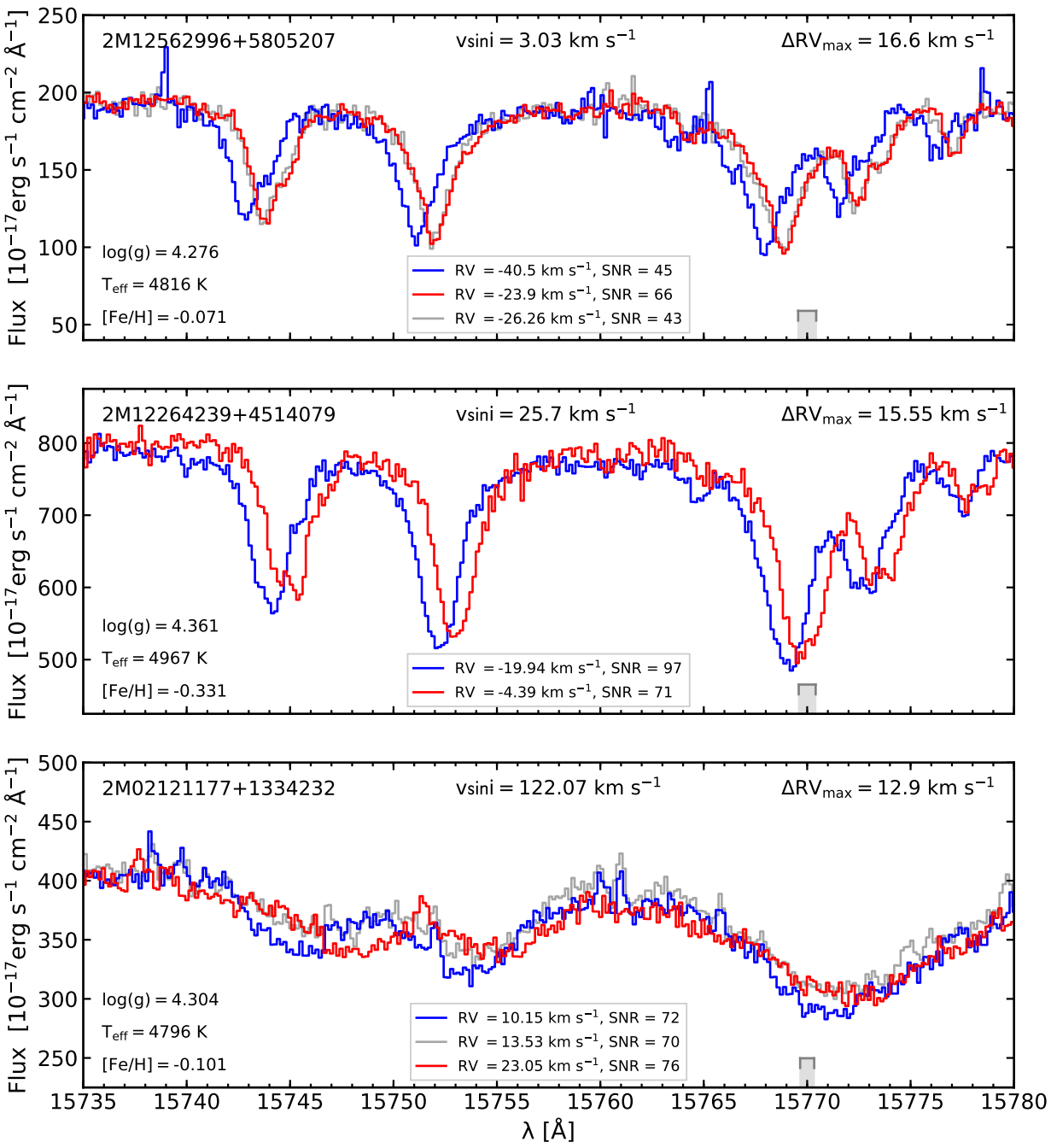

Figure 21: Visit spectra for three dwarfs with similar stellar parameters ($\log(g)$, $T_{\rm eff}$, metallicity) and $\Delta{\rm RV}_{\rm max}$ but a range of $v \sin i$ values representative of our sample. The top panel shows a slowly-rotating dwarf, the middle panel a progressively faster rotator, and the bottom panel an extremely fast rotator relative to our sample. The visit with maximum RV is shown in red and the minimum RV shown in blue, and the three major absorption lines are all from magnesium. The gray ruler at the bottom right of each panel shows the expected shift in wavelength from each star's $\Delta{\rm RV}_{\rm max}$ for a feature centered on $\lambda = 15770$ Å. Even with the extremely broadened lines in the final panel, we can still identify RV shifts from APOGEE spectra.

thought to be two or three orders of magnitude smaller than orbital circularization timescales, but depend on eccentricity (Mazeh 2008). Between the onset of rotational synchronization and the final circularization of the orbit, multiple systems can experience "pseudosynchronization" where the star's rotation speed is synchronized to its orbital speed at periastron (Mazeh 2008; Zahn 2008), but full synchronization can be further delayed or prevented due to three-body effects (Lurie et al. 2017). The timescale for orbital circularization depends strongly on the orbital period and the structure of the star's convective and radiative envelopes (Verbunt et al. 1995). Together, these effects produce pitfalls for gyrochronology, the method of calculating a star's age based upon a decrease in its rotation speed as it ages. Due to rotational synchronization, stars in close binaries may have rotation speeds much greater than their single counterparts of the same age (e.g. Simonian, Marc H. Pinsonneault, and Terndrup 2019).

The goal of this paper is to characterize the dependence of stellar rotation on close binary interactions and evolutionary state via reasonable assumptions about rotational synchronization using public data from APOGEE and *Gaia*, stellar parameters measured from this data, and rotation speeds derived from rotational line broadening in the APOGEE spectra (Dixon et al. 2020; Tayar et al. 2015). So far, the connection between intrinsic stellar parameters, stellar multiplicity, and stellar rotation has been explored mainly using small samples in stellar clusters (for a review, see Mazeh 2008), or more recently with rotation periods from *Kepler* (Simonian, Marc H. Pinsonneault, and Terndrup 2019; Simonian, Marc H. Pinsonneault, Terndrup, and Saders 2020). Here, we aim to provide a broad study of these relationships using a large sample of field stars, with a specific focus on the implications for gyrochronology. We discuss our sample selection and pipeline in Section 3.1.1 and our theoretical framework in Section 3.1.2, present our results in Sections 3.2 and 3.3, and draw our conclusions in Section 3.4.

3.1 Data and Methods

3.1.1 Sample Selection

Spectral parameters are taken from the APOGEE Data Release 14 `allStar` file, which contains entries for 277 371 objects (Abolfathi et al. 2018; Holtzman, Hasselquist, et al. 2018; Jönsson, Carlos Allende Prieto, et al. 2018). Note that only 258 475 unique APOGEE IDs exist among these entries; this is because the same star may be observed on different fiber plugplates that each correspond to a different field center, but ASPCAP does not automatically combine all visit spectra with the same APOGEE ID from different fields. However, the combination of an APOGEE ID and field location ID can securely identify each unique target, its combined spectrum, its associated stellar parameters in the `allStar` file, and its individual visit RVs in the `allVisit` file.

Our first round of quality cuts removed stars with the STAR_BAD flag set in the ASPCAP bitmask (Holtzman, Shetrone, et al. 2015). Stars identified as commissioning observations (bit 1 in STARFLAG ibid.) and telluric calibrators (bit 9 in both the apogee target2 and apogee2 target2 masks Zasowski, Cohen, et al. 2017; Zasowski, Johnson, et al. 2013) were removed as well. We limited our sample to field stars by removing known cluster members (bit 9 in apogee target1 and apogee2 target1 and bit 10 in apogee target2 and apogee2 target2).

We required that stars have well measured ($\neq -9999$, the default for a bad value), uncalibrated effective temperatures ($T_{\rm eff}$) and surface gravities [$\log(g)$], because most APOGEE DR14 dwarfs do not have calibrated $\log(g)$ values (Holtzman, Hasselquist, et al. 2018). In this work, we chose to restrict our view to giants and dwarfs, so we first removed all stars identified as RC in the APOGEE DR14 RC catalog (Bovy et al. 2014). We then estimated deredenned JHK_s magnitudes from the A_k value adopted in targeting (AK_TARG, Zasowski, Cohen, et al. 2017; Zasowski, Johnson, et al. 2013) and used them to further remove potential RC stars based upon the criteria outlined in Price-Jones et al. 2017.

Using the VISITS_PK indices (Holtzman, Shetrone, et al. 2015; Nidever et al. 2015), we identified the individual visits that are included in the combined APOGEE spectrum

for each APOGEE ID/location ID combination and required that two or more of the visit spectra had S/N$\geq$ 40. We concatenated all acceptable visit RVs for stars with duplicated APOGEE IDs, meaning stars with at least one good visit in two or more fields are included in our data set. For these objects, any stellar parameters with multiple valid ($\neq -9999$) values were averaged. We do not use the RV uncertainties in quality cuts and instead use the $\Delta\mathrm{RV}_{\mathrm{max}}$ distributions to inform our estimates for the RV precision in Section 3.2.

Close companions with sufficiently high q can produce measurable contributions to the observed spectrum, which can introduce biases into APOGEE's spectral fits and resulting spectral parameters (K. El-Badry et al. 2018). Additionally, these double-lined spectroscopic binaries, or SB2s, can lead to two distinct peaks in the spectrum's cross-correlation function and thus unreliable identification of the primary's RVs. We account for this uncertainty in the RV selection by using the sample of likely SB2s presented in C. N. Mazzola et al. 2020, where the RV for each visit was determined at the highest peak of either the APOGEE CCFs or recalculated CCFs using the method described in Kounkel, K. Covey, et al. 2019; Kounkel, K. R. Covey, et al. 2021. Our quality-cut sample contained 108 789 stars, 1052 of which were identified as likely SB2s.

The APOGEE ASPCAP pipeline estimates rotational broadening for most dwarfs but nearly no giants or subgiants. Following the work of Dixon et al. 2020; Tayar et al. 2015, we cross-correlate the observed combined spectrum with broadened versions of the provided fit spectrum to determine if additional broadening is necessary over what was identified in the ASPCAP analysis. Because the APOGEE spectra are recorded on three individual detector arrays, this procedure was performed on the data from each of the arrays separately, giving us a mean and standard deviation for each additional broadening measurement. We excluded measurements below 5 km s^{-1} for giants, allowing measurements down to 2 km s^{-1} for dwarfs, and excluded any cases where the standard deviation was larger than the average. We then added this additional broadening to any $v \sin i$ measurement provided by the ASPCAP pipeline; for some stars where there was no $v \sin i$ provided before, we add new measurements.

After running our quality-cut APOGEE sample through this pipeline, we then removed the likely SB2s within our sample due to concerns that their rotation rates are likely over-

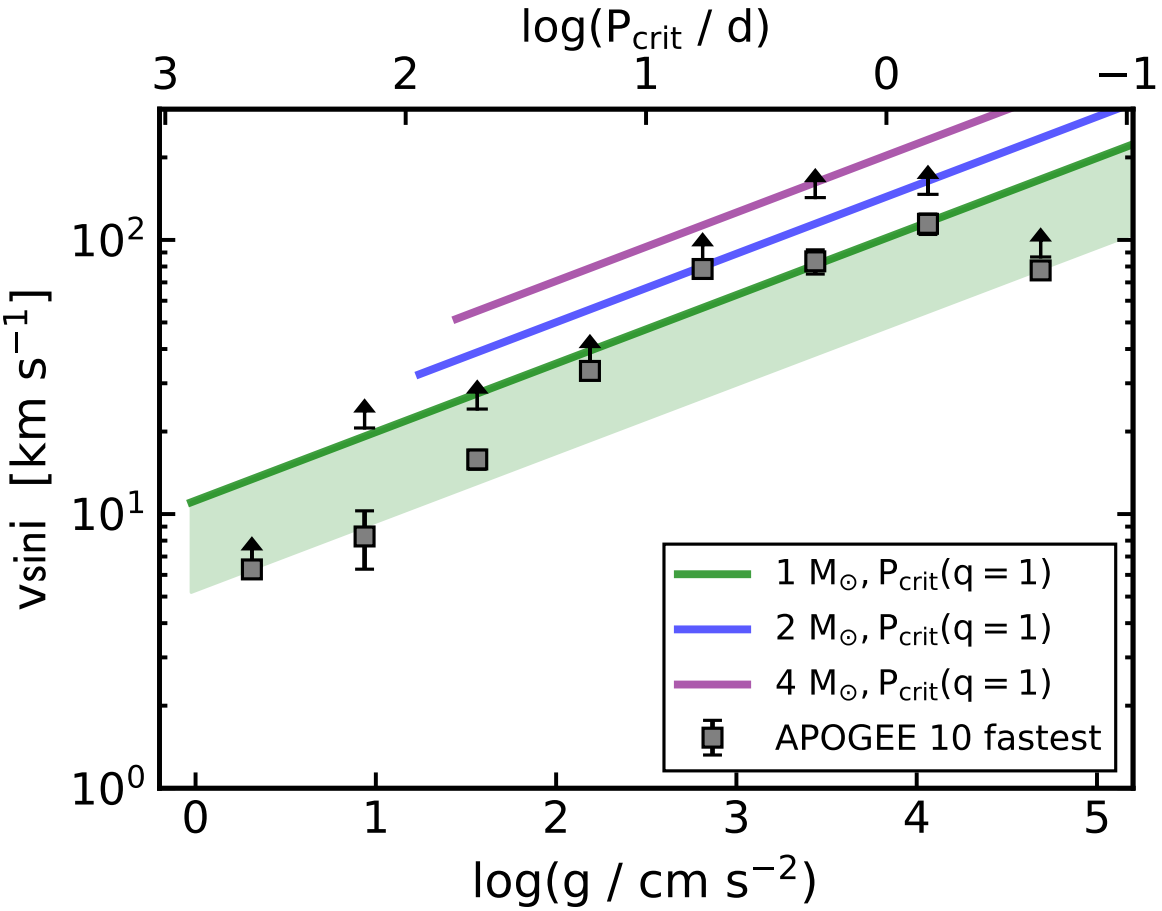

Figure 22: Relationship between $v \sin i$ and $\log(g)$ accompanied by theoretical upper limits. The median $v \sin i$ for the ten fastest rotators in each $\log(g)$ sample are shown as gray squares with error bars indicating Poisson uncertainties, and black arrows indicate the largest $v \sin i$ in each bin. The diagonal lines are theoretical constraints for several masses assuming $q = 1$, perpendicular rotational axes ($i_{\rm rot} = 90°$), and tidal synchronization at the beginning of RLOF ($\rm P_{orb} = P_{rot} = P_{crit}$). Because our sample is biased against high-q systems after removing suspected SB2s, the green shaded region indicates $0.25 \leq q \leq 1.0$. The top axis shows $\rm P_{crit}$ (equation 3.1) for a binary with $q = 1$, $M = 1$ $\rm M_\odot$ across the range of $\log(g)$ values. The colored lines end at the TRGB in MIST models of solar metallicity.

estimated due to our pipeline interpreting blended spectral lines as rotational broadening (Simonian, Marc H. Pinsonneault, Terndrup, and Saders 2020). This will bias our sample of binaries towards mass ratios $q \lesssim 0.9$, and this may introduce a slight bias towards higher primary masses, as there is some evidence that K-type stars have a larger twin excess than FG stars (Kareem El-Badry, Rix, et al. 2019). However, an individual analysis of each SB2 spectrum and estimated $v \sin i$ would be required to confidently include them, and such an analysis is beyond the scope of the current work.

We used APOGEE DR14 rather than the newest public (DR16) or proprietary (DR17) data so that we could cross-match our sample against the Sanders et al. 2018 catalog to add estimates of mass M, distance d, and age τ. ibid. provides Bayesian posteriors for these parameters by using broadband photometry, spectral parameters from a number of spectroscopic surveys, including APOGEE DR14, and *Gaia* DR2 parallaxes to fit PARSEC isochrones. Requiring non-NAN values for d, M, and τ resulted in a final sample with 104 987 stars. The HR diagram for our final sample is shown in Fig. 20, with absolute 2MASS magnitude $J_{\rm abs}$ plotted versus APOGEE uncalibrated $T_{\rm eff}$. The points are colored by the maximum RV shift, $\Delta \mathrm{RV}_{\rm max} = |\mathrm{RV}_{\rm max} - \mathrm{RV}_{\rm min}|$ (see also Badenes and Maoz 2012; Badenes, C. Mazzola, et al. 2018; Maoz et al. 2012; C. N. Mazzola et al. 2020; Moe, Kaitlin M. Kratter, and Badenes 2019). Many of the same features noted in C. N. Mazzola et al. 2020 are also clear in this similar sample, e.g. high $\Delta \mathrm{RV}_{\rm max}$ stars spread across the entire HR diagram, though we note that the sequence of high-$\Delta \mathrm{RV}_{\rm max}$ stars in the photometric binary sequence is far less pronounced without the SB2s that were included in that prior work. For further commentary, we refer the reader to the discussion in that work. Using the distribution from these parameters, we make one final cut to select giants and dwarfs with the red dotted lines shown in Fig. 20, yielding a sample of 79 308 giants and 24 768 dwarfs. The lines are drawn such that we remove outliers from the bulk of the distribution while retaining the offset photometric binary sequence among the dwarfs at the expense of also retaining some subgiants, which we will revisit in Section 3.3. These cuts may also remove potential blue stragglers, but as these stars may have anomalously large rotation speeds as a result of binary mass transfer or mergers (see E. Leiner, Mathieu, Vanderburg, et al. 2019, and discussion within), a deeper analysis would be required to accurately interpret any observations and is

beyond the scope of the current work.

Further requiring a measured value for $v \sin i$ limits our sample to 2786 giants and 24 496 dwarfs. Below is a summary of the differences between the ASPCAP measurements for these stars and the values we use in this work:

1. 1851 giants and 23 865 dwarfs had no changes to their ASPCAP $v \sin i$ measurements;
2. 46 giants and 516 dwarfs had additional rotational broadening between $0 < \Delta v \sin i < 10$ km s^{-1};
3. 40 giants and 98 dwarfs had added rotational broadening of $\Delta v \sin i \geq 10$ km s^{-1};
4. 849 giants and 17 dwarfs did not have ASPCAP $v \sin i$ values and so our pipeline provides measurements.

Fig. 21 shows visit spectra for several representative stars with large $\Delta \mathrm{RV}_{\mathrm{max}}$, similar $\log(g)$, T_{eff}, and [Fe/H], and a range of $v \sin i$ values. Though the star in the bottom panel demonstrates extreme rotational broadening relative to the other stars, the high-quality spectra from APOGEE are still able to confidently distinguish large variation in stellar RVs.

3.1.2 Theoretical Framework

In the simplest approximation, we expect the orbital properties of a short-period binary to dictate the rotation period of its constituent stars through spin-orbit synchronization. In that case, the properties of the orbit predict the range of allowed stellar rotation velocities, and we can use this allowed range to interpret the distributions of measured values and relate them to the physics of tidal interactions in binary systems.

Assuming a star is spherical and lacks surface differential rotation, we can define its rotation speed as

$$v \sin(i_{\mathrm{rot}}) = \frac{2\pi R}{\mathrm{P}_{\mathrm{rot}}} \sin(i_{\mathrm{rot}}) = \frac{2\pi}{\mathrm{P}_{\mathrm{rot}}} \sqrt{\frac{GM}{g}} \sin(i_{\mathrm{rot}}) \tag{3.3}$$

where g is the surface gravity, $\mathrm{P}_{\mathrm{rot}}$ is the period of rotation, and i_{rot} is the inclination angle of the axis of rotation. This ignores surface differential rotation, which has been observed with *Kepler* in single stars (Reinhold and Gizon 2015; Reinhold, Reiners, et al. 2013) and more recently in eclipsing binaries (Jermyn et al. 2020; Lurie et al. 2017). However, Zeeman

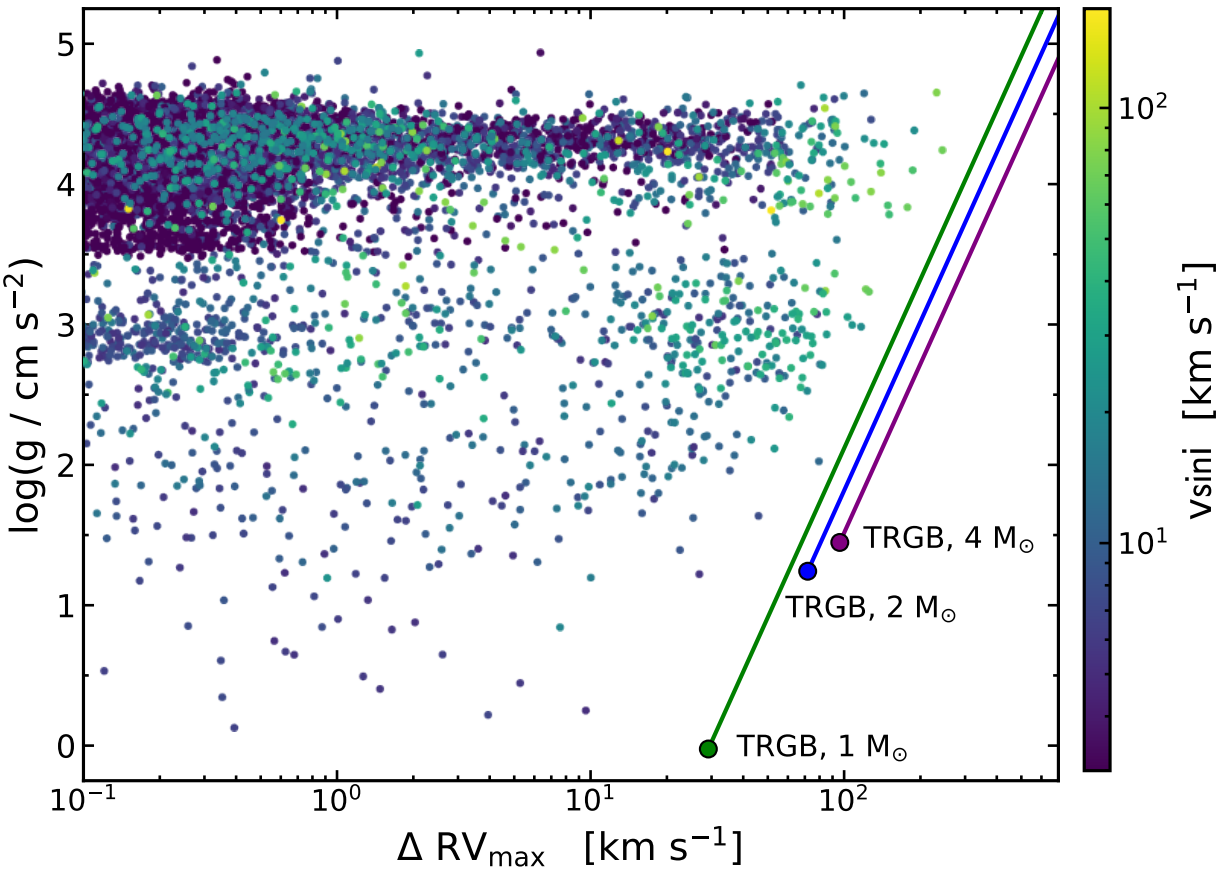

Figure 23: Distribution of $\Delta\mathrm{RV}_{\mathrm{max}}$ and $\log(g)$ for our sample with a color bar on $v \sin i$ which shows a correlation between large $\Delta\mathrm{RV}_{\mathrm{max}}$ and $v \sin i$. The diagonal lines show the maximum $\Delta\mathrm{RV}_{\mathrm{max}}$ values expected as a function of $\log(g)$ at 1 (green), 2 (blue), and 4 $\mathrm{M}_\odot$ (purple), which are calculated from equation (3.2) assuming $q = 1$, $e = 0$, $i_{\mathrm{orb}} = 90°$, and $\mathrm{P}_{\mathrm{orb}}$=$\mathrm{P}_{\mathrm{crit}}$. Terminal symbols show the position of the TRGB.

Doppler imaging indicates that surface differential rotation in fast rotating stars is very small, so for the sake of calculating upper limits, we will ignore differential rotation and assume we can relate the observed rotation speed $v \sin(i_{\rm rot})$ to a singular rotational period $P_{\rm rot}$ via equation (3.3).

We distinguish between the orbital and rotational inclination angles because it still unclear what the preferred system alignment is (Justesen et al. 2020). Neither of these angles are directly measurable from our data, and so we will refer to our measured rotation speeds as $v \sin i$ where i includes effects from both rotational and orbital inclination angles.

We can relate our understanding of stellar evolution to expectations for rotational synchronization by looking at the relationship between $\log(g)$ and $v \sin i$. As a Sun-like star ascends the RGB, its $\log(g)$ will decrease and its radius will increase until it reaches the TRGB. This gradually reduces the allowed range of semi-major axis for a detached nearby companion as $P_{\rm crit}$ for RLOF increases, the tidal period lengthens, and the maximum $v \sin i$ decreases. In this framework, we can calculate theoretical upper limits for measured quantities by assuming stellar masses that are representative of our sample and combining equations (3.1) and (3.3) under these assumptions:

1. equal mass binary, $q = 1$
2. rotation axis perpendicular to line-of-sight, $i_{\rm rot} = 90^\circ$
3. $P_{\rm crit}$ is the minimum possible period
4. orbital synchronization occurring at the minimum period, $P_{\rm rot}$=$P_{\rm orb}$=$P_{\rm crit}$

The resulting relationships between $v \sin i$ and $\log(g)$ are shown as the solid lines in Fig. 22. We use solar metallicity models from the MESA Isochrone and Stellar Tracks collaobration (MIST; Choi et al. 2016; Dotter 2016; Paxton, Bildsten, et al. 2011; Paxton, Cantiello, et al. 2013; Paxton, Marchant, et al. 2015) to determine the location of the TRGB (corresponding to the maximum radius and lowest $\log(g)$) for each mass. Removing the suspected SB2s has biased our sample against high-q systems, so the green shaded region shows the range of $v \sin i$ expected for $0.25 \leq q \leq 1.0$. We compare these theoretical limits to the median $v \sin i$ of the ten fastest rotators in each $\log(g)$ bin, shown as the gray squares with error bars showing Poisson uncertainties, and the maximum observed $v \sin i$ for each bin, indicated by

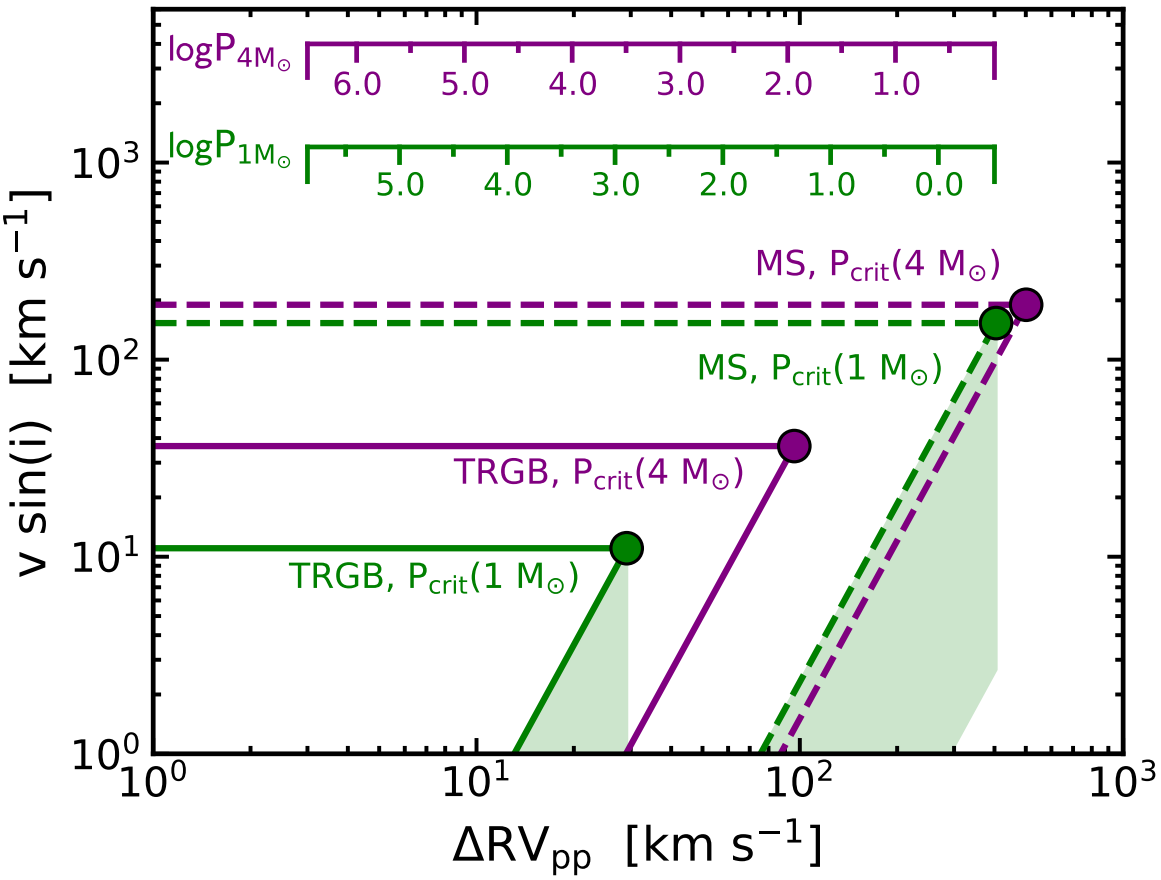

Figure 24: Theoretical constraints on ΔRV_{pp} and $v \sin i$ assuming $q = 1$, edge-on ($i_{orb} = 90°$), circular orbits, perpendicular rotational axes ($i_{rot} = 90°$), and tidal synchronization ($P_{orb} = P_{rot}$). The diagonal lines are calculated using equations 3.2-3.3 for $P \geq P_{crit}$, where the circular point shows P_{crit} and hence the start of RLOF (equation 3.1). The $\log(g)$ values for each point are taken from MIST models at solar metallicity. The MS points are $\log(g/\text{cm s}^{-2}) = 4.546$ (1 $M_\odot$) and 4.316 (4 $M_\odot$), while the TRGB are $\log(g/\text{cm s}^{-2}) = -0.024$ (1 $M_\odot$) and 1.447 (4 $M_\odot$). Shaded regions indicate the range expected for $1° \leq i_{rot} \leq 90°$; for each point on the diagonal, follow the shaded region straight down to see the range of expected $v \sin i$ values. Horizontal lines emphasise the maximum $v \sin i$ expected at the start of RLOF. The colored rulers indicate the $\log(P/d)$, where $P = P_{orb} = P_{rot}$, that corresponds to the ΔRV_{pp} values along the x-axis for each mass.

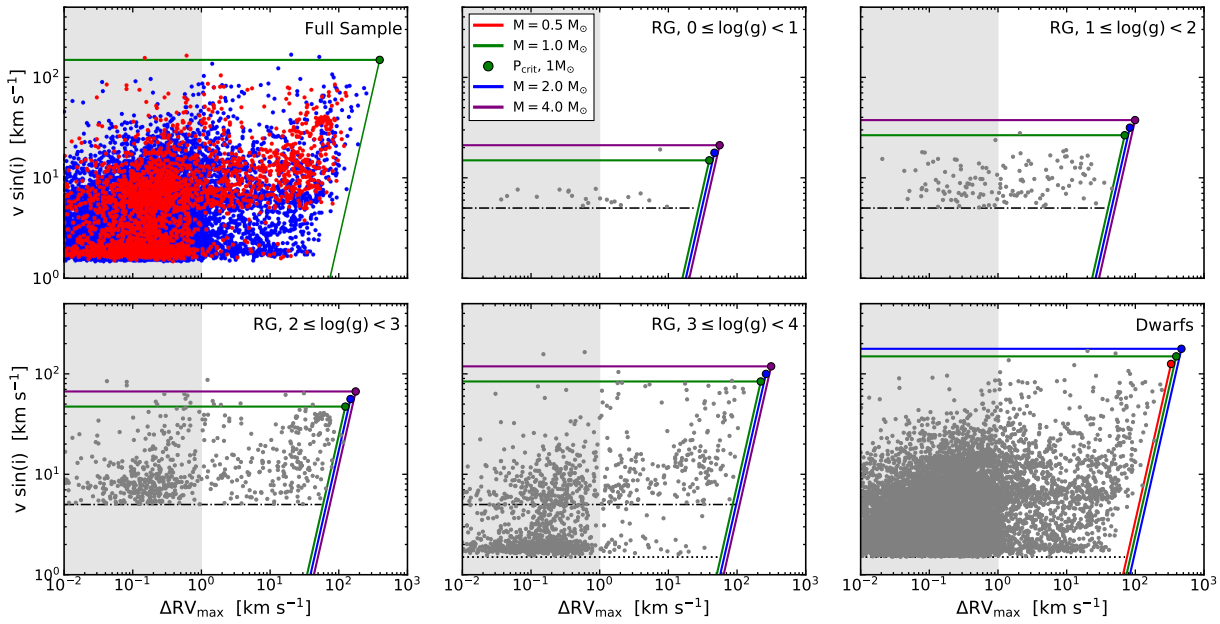

Figure 25: Distribution of $v \sin i$ and $\Delta\mathrm{RV}_{\mathrm{max}}$ plotted alongside theoretical constraints assuming orbital synchronization. The diagonal lines show the same theoretical constraints shown in Fig. 24 calculated at the midpoint of the $\log(g)$ bin and a range of masses representative of the Sanders et al. 2018 mass distribution for that $\log(g)$ sample. We distinguish two regions of interest, likely RV variables from stars with noise-dominated RV variation, by hatching $\Delta\mathrm{RV}_{\mathrm{max}} \leq 1$ km s^{-1}. The dash-dot line shows the minimum $v \sin i$ measurement from our pipeline, $v \sin i = 5$ km s^{-1}, and the dotted line in the final two panels show the approximate minimum value from ASPCAP, $v \sin i = 1.5$ km s^{-1}. Top left: the red and blue points designate our giants and dwarfs samples, respectively. Remaining panels: gray points indicate the main sample across various $\log(g)$ bins.

the black arrows. The maximum observed rotation speed for each bin is strongly driven by the stars' $\log(g)$, and the simple set of assumptions laid out above are able to reproduce the general trend exhibited by the APOGEE data.

3.2 Results: The relationship between rotation, evolution, and stellar multiplicity

We now consider the joint relationship between RV variability, stellar evolution, and stellar rotation through $\Delta\mathrm{RV}_{\mathrm{max}}$, $\log(g)$, and $v \sin i$ in Fig. 23. Starting from assumptions listed previously, we further require an edge-on ($i_{\mathrm{orb}} = 90°$), circular ($e = 0$) orbit to find the maximum expected $\Delta\mathrm{RV}_{\mathrm{pp}}$ values as a function of $\log(g)$. These constraints are shown as the diagonal lines, and the maximum $\Delta\mathrm{RV}_{\mathrm{max}}$ values in our sample are nicely bounded by them, as Badenes, C. Mazzola, et al. 2018 noted with APOGEE DR13 data. Stars with $\Delta\mathrm{RV}_{\mathrm{max}} \lesssim 1$ km s^{-1} may be the result of RV uncertainties and should not be treated as a true detection of RV variability. As we discuss in more detail later, true RV variables can begin to be identified from $\Delta\mathrm{RV}_{\mathrm{max}} \gtrsim 1$ km s^{-1}; in our sample, 627 giants (23 per cent) and 1556 dwarfs (6.4 per cent) have $\Delta\mathrm{RV}_{\mathrm{max}} > 1$ km s^{-1}. The points in Fig. 23 are colored by $v \sin i$, and we observe a color gradient with $\Delta\mathrm{RV}_{\mathrm{max}}$: stars with large RV variability are more likely to have large $v \sin i$ values. More quantitatively, we can compare the ratio of rapid rotators ($v \sin i \geq 10$ km s^{-1}) to slow rotators ($v \sin i < 10$ km s^{-1}) for RV variables and non-RV variables. Giants with $\Delta\mathrm{RV}_{\mathrm{max}} \geq 10$ km s^{-1} have $N_{\mathrm{fast}}/N_{\mathrm{slow}} = 223/84 = 2.65$, whereas giants with $\Delta\mathrm{RV}_{\mathrm{max}} < 10$ km s^{-1} have $N_{\mathrm{fast}}/N_{\mathrm{slow}} = 434/2045 = 0.212$; for the dwarfs, these fractions are $178/293 = 0.608$ and $1254/22771 = 0.055$, respectively.

To explore this relationship further, we relax our previous orbital synchronization condition ($\mathrm{P}_{\mathrm{rot}}$=$\mathrm{P}_{\mathrm{orb}}$=$\mathrm{P}_{\mathrm{crit}}$) and allow the synchronized period to be any value that is equal to or larger than the critical period for RLOF ($\mathrm{P}_{\mathrm{rot}}$=$\mathrm{P}_{\mathrm{orb}}$≥$\mathrm{P}_{\mathrm{crit}}$). We will use these assumptions to produce upper limits on $\Delta\mathrm{RV}_{\mathrm{pp}}$ and $v \sin i$ and directly compare with our observed $\Delta\mathrm{RV}_{\mathrm{max}}$ and $v \sin i$. Before we compare with data, we display these constraints for two different masses and two $\log(g)$ values corresponding to solar-type main sequence (MS) and TRGB

evolutionary phases in Fig. 24. The shaded regions show the range of expected rotation speeds if we vary $i_{\rm rot}$ from $1 - 90°$. The horizontal lines provide an expected upper limit on the rotation speed for binaries with a given mass and $\log(g)$. Note that this is not a hard upper limit, like the break-up velocity, but is simply the point where RLOF begins and the system will experience more complex interactions due to mass transfer.

Fig. 25 displays these constraints against the measurements for our APOGEE dwarfs and giants. The upper left panel shows the giants in red and the dwarfs in blue, together with the theoretical upper limits calculated for a star with $M = 1$ M$_\odot$, $\log(g)$= 4.5. The dwarfs are shown by themselves in the final panel, and the remaining panels show the giants split into four bins in $\log(g)$.

The theoretical upper limits prove generally successful at constraining the data in both axes, and we recover the predicted upper limit on $v \sin i$ as a function of $\log(g)$. From theory and Fig. 22, we expect that stars with higher $\log(g)$ values are able to rotate faster due to their smaller radii, and combined with our characterization of RLOF via $\rm P_{crit}$, the horizontal lines constrain the vast majority of the observed $v \sin i$ values. The few exceptions in the bottom panels are discussed in more detail below.

The hatched region from $\Delta \rm RV_{max} \leq 1$ km s^{-1} is intended to guide the eye in distinguishing stars whose RV variability is most likely driven by RV uncertainties from *bona fide* RV variables that are likely to have short-period companions. For an extended discussion of the influence of stellar properties and RV errors on the distribution of $\Delta \rm RV_{max}$, we refer the reader to Badenes, C. Mazzola, et al. 2018.

For now, we will make a few observations about general trends in these groups of stars.

1. In every panel with adequately large samples, stars with $\Delta \rm RV_{max} \geq 1$ km s^{-1} appear to show $v \sin i$ values that span the entire range up to the theoretical limit.
2. In the lower panels, stars with $\Delta \rm RV_{max} < 1$ km s^{-1} (hatched region) demonstrate two roughly distinct populations. There is a noisy trend of decreasing rotation speed with decreasing $\Delta \rm RV_{max}$; as $v \sin i$ decreases, spectral lines become sharper, making RV measurements more accurate. While we still caution against inferring binarity from RV variability at these low $\Delta \rm RV_{max}$, it is worth noting the overall trend between rotation and $\Delta \rm RV_{max}$. However, there are some systems with $v \sin i$ that extend up to or just

above the horizontal lines, and these are discussed in more detail in point (v).

3. The dot-dashed horizontal lines ($v \sin i = 5$ km s^{-1}) and dotted lines ($v \sin i = 1.5$ km s^{-1}) indicate the minimum $v \sin i$ measurement from our pipeline or ASPCAP. We removed giants with $v \sin i < 5$ km s^{-1} from our sample due to the pipeline's unreliability below this threshold (Tayar et al. 2015). The pipeline is more reliable for dwarfs, who have narrower lines in general due to their larger $\log(g)$, so we allowed dwarfs to have $v \sin i$ down to the minimum measurement value. However, the RG bin with $3 \leq \log(g) < 4$ contains a mixture of giants and subgiants and thus a mixture in the lower allowed $v \sin i$ measurement.
4. From Fig. 24, a star with a large $\Delta\mathrm{RV}_{\mathrm{max}}$ value can have an unfavorable i_{rot} and thus a $v \sin i$ value that would be beyond the diagonal line. A few stars lie along the boundaries, particularly in the dwarf and RG $2 \leq \log(g) < 3$ panels, but none lie significantly beyond the diagonal lines. Measuring rotation through $v \sin i$ necessarily biases our sample against low i_{rot}, so our data is unable to distinguish whether this lack of result is due to selection effects or to something more fundamental, such as preferential spin-orbit alignment.
5. The vast majority (> 85 per cent) of the stars that lie off the sequence described in (ii), including all six stars with low $\Delta\mathrm{RV}_{\mathrm{max}}$ and rotation speeds above the horizontal lines, have sparsely sampled RV curves with only two or three visits that pass our quality cuts, so these may be true binaries whose visits are unfortunately timed in the orbit. Out of the six stars above the upper limits, the minimum and maximum RVs for one star (2M18423451-0422454) are separated by roughly seven months, but the other five outliers have all their visits spaced out over two to four days. Additional RVs could help distinguish whether these are unluckily sampled binaries or single stars with extremely fast rotation and will be the subject of future investigations.

Estimates for the orbital periods would provide great insight into the extent orbital synchronization explains our high-$\Delta\mathrm{RV}_{\mathrm{max}}$ and high-$v \sin i$ systems. We cross-matched our stars against the *Gold Sample* from A. M. Price-Whelan, Hogg, Rix, Beaton, et al. 2020 to add estimates for orbital parameters from their custom Monte Carlo sampler, *The Joker*. This resulted in 45 dwarfs and 19 giants, which was too small of a sample for us to draw

meaningful conclusions. These results are unsurprising, since tightly constraining orbital parameters from an RV curve typically requires a large number of RVs (for a discussion, see A. M. Price-Whelan, Hogg, Rix, Beaton, et al. 2020), but the majority of the stars in our sample have only two (41.4 per cent) or three (43.4 per cent) visits. Expanding the number of stars in our sample with estimated orbital parameters is the subject of future work.

Fig. 26 compares the normalized $\Delta\mathrm{RV}_{\mathrm{max}}$ histograms for our slow and rapid rotators ($v \sin i < 10$ km s^{-1} and $v \sin i \geq 10$ km s^{-1}) in gray and black, respectively. The histogram bin values are normalized by the largest histogram bin, which is $N_{\mathrm{max}}^{\mathrm{slow}} = 1369$ and $N_{\mathrm{max}}^{\mathrm{fast}} = 60$ for the dwarfs and $N_{\mathrm{max}}^{\mathrm{slow}} = 121$ and $N_{\mathrm{max}}^{\mathrm{fast}} = 27$ for the giants. The slow rotators display the standard features of a high-quality statistical sample of sparsely sampled RV curves: a core of low $\Delta\mathrm{RV}_{\mathrm{max}}$ values dominated by RV uncertainties, and a tail of genuine RV variables dominated by short-period binaries (Maoz et al. 2012). A vertical line at $\Delta\mathrm{RV}_{\mathrm{max}}$= 3 km s^{-1} shows the clear transition from core to tail seen in dwarf slow rotators, though this transition from core to tail is less clear for the giants because larger RV uncertainties, on average, contribute to a broader core (Badenes, C. Mazzola, et al. 2018). The distributions for the rapid rotators deviate considerably from this model, with a much broader core that extends out to $\Delta\mathrm{RV}_{\mathrm{max}} \lesssim 10$ km s^{-1} and then an equivalent fraction of RV variable systems with $\Delta\mathrm{RV}_{\mathrm{max}} \gtrsim 10$ km s^{-1}. The rapid rotators' broader core is due to larger RV uncertainties from their rotationally broadened lines, as Fig. 21 demonstrates. With these caveats in mind, we will use the threshold $\Delta\mathrm{RV}_{\mathrm{max}} \geq 3$ km s^{-1} as an indicator for RV variability in Section 3.3 but will include a comparison to the threshold $\Delta\mathrm{RV}_{\mathrm{max}} \geq 10$ km s^{-1} in the text.

To help interpret these distributions, we rely on the Monte Carlo (MC) sampler described in C. N. Mazzola et al. 2020, which is built to simulate populations of mock multiple systems and predict their $\Delta\mathrm{RV}_{\mathrm{max}}$. We defer a detailed discussion of the MC sampler to those in Badenes, C. Mazzola, et al. 2018 and C. N. Mazzola et al. 2020 and instead briefly describe the MC and list the settings used in this work. Each simulated binary is assigned its main orbital parameters from observational distributions and randomly assigned an orbital inclination and initial phase. We then simulate observations of the system's RVs using the randomly assigned visit history of a real APOGEE star in our sample, with RV errors drawn from a user-specified distribution. In this work, primary masses are drawn from the Sanders et al.

2018 mass distributions, and we assume a flat mass ratio distribution between $0.1 \leq q \leq 0.9$ (Moe and Di Stefano 2017), allowing no binaries with $q > 0.9$ to account for our sample's bias against equal-mass binaries from the removal of likely SB2s. The remaining settings are listed in Table 7; the number of stars in each mock sample, N, was chosen to be ten times the the number of objects in the corresponding $\log(g)$ bin from our data to allow for bootstrapping uncertainty regions but keeping the relative fraction of systems the same. The simulations corresponding to the first four rows of Table 7 were combined when looking at the APOGEE giants as a whole (like in Fig. 26), but could be separately analyzed if desired. The simulation corresponding to the fifth row was used to compare against our APOGEE dwarfs.

The red, green, and blue histograms in Fig. 26 show normalized $\Delta\mathrm{RV}_{\mathrm{max}}$ distributions for various samples of MC-simulated binaries. The blue histogram shows all of our simulated binaries, which have a clear core and tail similar to the slow rotators in APOGEE. The green histogram corresponds to all close ($\log(\mathrm{P/d}) < 4.0$) binaries; here, too, there is a significant fraction of systems with low $\Delta\mathrm{RV}_{\mathrm{max}}$, but the tail of RV variables is much larger. The red histogram represents the closest binaries ($\log(\mathrm{P/d}) < 2.0$), which are completely dominated by RV variables. It also has very few stars at low $\Delta\mathrm{RV}_{\mathrm{max}}$ because the large $\Delta\mathrm{RV}_{\mathrm{pp}}$ values make it highly unlikely to observe the primary at points in its orbit with similar RV, though not impossible, as suggested by the few stars with high $v \sin i$ low $\Delta\mathrm{RV}_{\mathrm{max}}$ and three or fewer visits discussed previously. For both dwarfs and giants, the $\Delta\mathrm{RV}_{\mathrm{max}}$ distributions of the fast rotators in APOGEE show prominent tails of RV variables, indicating that these samples have a large fraction of short period binaries.

3.3 Discussion: Implications for Gyrochronology

Observations of open clusters and star forming regions have revealed that protostars are born with a wide range of rotation rates (Kraft 1965; Stauffer et al. 1987; Vogel et al. 1981). Regardless of their initial rotation speed, stars with masses below 1.3 $\mathrm{M}_{\odot}$, corresponding to $T_{\mathrm{eff}} < 6250$ K, tend to spin down over their MS lifetimes, whereas higher-mass stars maintain

Table 7: Parameters used to produce mock data from MC simulations.

N	multiplicity fraction f_m	$\log(g/\mathrm{cm\ s^{-2}})$	RV error source	RV error μ (km s^{-1})	RV error σ (km s^{-1})
30 000		0.5			0.75
230 000		1.5			0.25
340 000	0.5	2.5	Gaussian	0.0	0.25
200 000		3.5			0.25
260 000		4.5			0.25

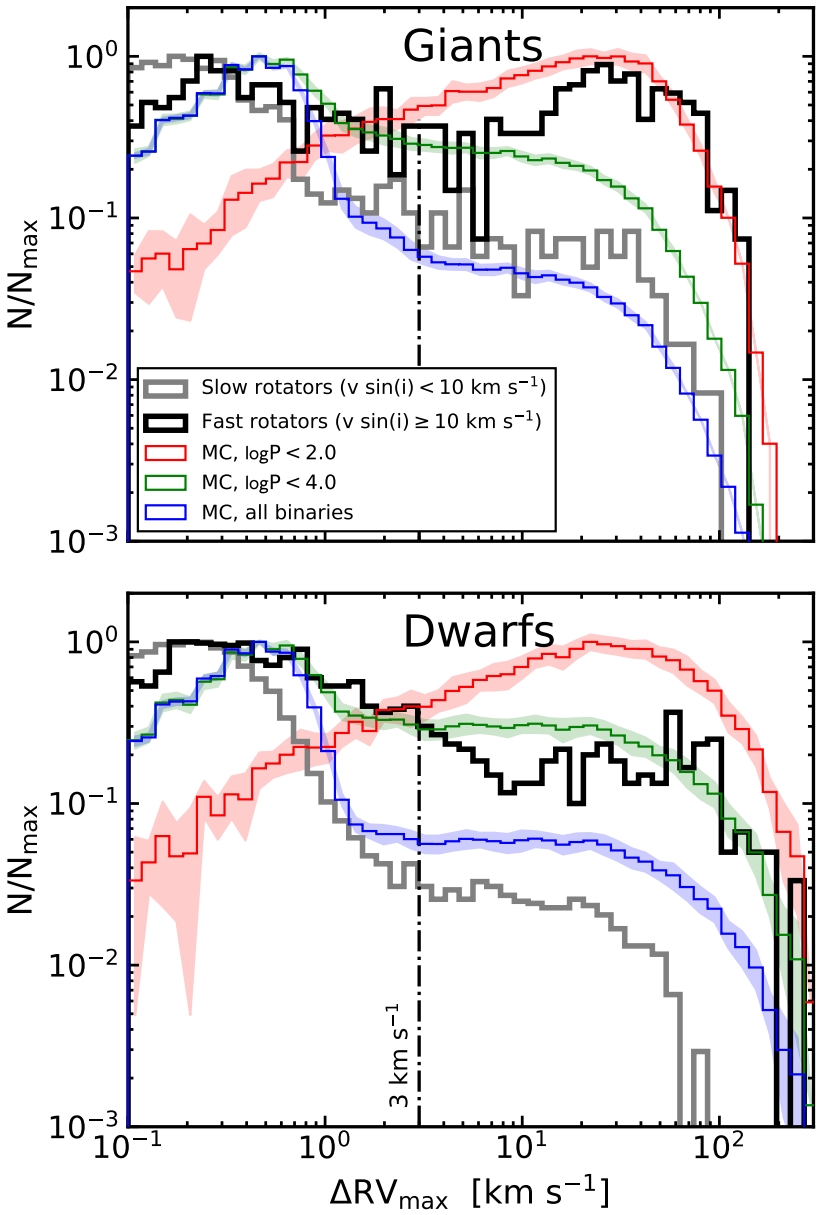

Figure 26: Normalized ΔRV_{max} histograms with slow and fast rotators shown in gray and black, respectively. The red, green, and blue lines are for several log(P/d) samples from the relevant MC simulations, with shading indicating 1σ intervals from bootstrapping the sample ($N_{boots} = 50$). The tail of RV variables appears to begin around $\Delta RV_{max} = 3$ km s^{-1} for the slow rotators but is closer to 10 km s^{-1} for the rapid rotators. The distributions for the rapid rotators in both dwarfs and giants display a broad core ($\Delta RV_{max} \lesssim 10$ km s^{-1}), likely connected to larger RV uncertainties from rotationally broadened lines, and a prominent tail ($\Delta RV_{max} \gtrsim 10$ km s^{-1}) that, upon comparison with the MC simulations, suggests these samples contain a significant fraction of short period binaries.

the rotation they were imparted at their births much more effectively (Wolff et al. 1986). This mass threshold is known as the Kraft break (Kraft 1967) and is thought to be due to the presence, or lack thereof, of convective envelopes (Durney et al. 1978). Stars below the Kraft break have convective envelopes which drive magnetized winds that cause angular momentum loss, slowing the star's rotation rate as it ages. Gyrochronology relations use the empirical constraints from clusters (Gallet et al. 2015; Godoy-Rivera, Marc H. Pinsonneault, et al. 2021) and field stars (Angus, Aigrain, et al. 2015; Angus, Beane, et al. 2020) to parametrize this angular momentum loss and infer stellar ages from rotation speeds (Angus, Morton, et al. 2019; Barnes 2010, 2007; Epstein et al. 2014; Gallet et al. 2013; Kawaler 1987; Mamajek et al. 2008; Matt et al. 2015; M. H. Pinsonneault et al. 1989; Skumanich 1972; van Saders et al. 2013, but also see Saders et al. 2016).

To explore how close binaries diverge from the expectations of gyrochronology, we restricted our APOGEE dwarf sample to those stars below the Kraft break, or $T_{\rm eff} < 6250$ K. We based our selection on the $T_{\rm eff}$ values from APOGEE rather than the masses from Sanders et al. 2018 because the former are determined directly from the spectra. The line used to select our dwarf sample in Fig. 20 was chosen to retain the photometric binaries that are offset from the main sequence, but this leads to contamination from subgiants above $T_{\rm eff} \gtrsim 5300$ K. We use the same line shown in Fig. 20 but with a larger y-intercept to remove 1423 suspected subgiants from our sample.

We will compare the predicted gyrochronological ages of our sample to the isochrone ages from ibid., who calculated Bayesian posteriors on masses M and ages $\tau_{\rm SD}$ from fits to PARSEC isochrone using Gaia DR2 parallaxes, broadband photometry, and APOGEE spectral parameters. This method assumes single star models and introduces additional biases in some parameters, including masses and stellar ages (K. El-Badry et al. 2018), although our removal of SB2 systems should reduce systematic errors to some extent. In any case, stellar ages are notoriously hard to estimate without astroseismology (Ness et al. 2016; Marc H. Pinsonneault et al. 2018, and see Soderblom 2010 for a review). While age estimates for individual stars should only be considered a starting point for a deeper analysis, general trends should be preserved in our large, statistical sample.

We plot 2D and 1D histograms of $v \sin i$ and stellar age $\tau_{\rm SD}$ in Fig. 27. The black

histograms in the top and right panels show the distributions of each parameter, and the blue histograms represent the close binary fraction as a function of that parameter alone. In the 2D histogram on the left side of the figure, the bins are colored by the completeness corrected close binary fraction, shown in the colorbar at the bottom. We calculate completeness corrected close binary fractions using the same procedure described in Moe, Kaitlin M. Kratter, and Badenes 2019 and C. N. Mazzola et al. 2020, which we will briefly outline below.

From our MC simulations, we calculated the cumulative fraction of close ($\log(P/\mathrm{d}) < 4$) binaries with $\Delta\mathrm{RV}_{\mathrm{max}} \geq 3$ km s^{-1}, i.e., the fraction of binaries we would confidently detect. The inverse of this fraction is the factor needed to correct our sample for completeness and recover the total number of close binaries in our sample (for more discussion, see Sec. 3.1 and Fig. 3 in ibid.). From the MC simulation of our dwarf sample (see Section 3.2), we found a completeness fraction of 0.35 for $\Delta\mathrm{RV}_{\mathrm{max}} \geq 3$ km s^{-1} and $\log(\mathrm{P/d}) < 4$. As discussed in Moe, Kaitlin M. Kratter, and Badenes 2019 and C. N. Mazzola et al. 2020, we expect systematic biases that favor observing twin binaries in a magnitude-limited sample and disfavor observing SB2s with blended absorption features. Following ibid., we assume that the Malmquist bias favoring the detection of twin binaries should be larger than the difficulties inherent in measuring SB2 RV variability, so we reduce our completeness-corrected close binary fractions by 10 per cent. Accounting for this bias leads to an estimated detection efficiency of 0.39 for close ($\log(\mathrm{P/d}) < 4$) binaries in our dwarf sample when using our $\Delta\mathrm{RV}_{\mathrm{max}}$ threshold.

For both the 2D and 1D histograms, we require at least ten objects per bin to cover as much parameter space as possible. We calculate the RV variability fraction f (the fraction of systems with $\Delta\mathrm{RV}_{\mathrm{max}} \geq 3$ km s^{-1}) in each histogram bin and correct it for completeness: close binary fraction $= f/c$ where $c = 0.39$ is our detection efficiency. Uncertainties in the close binary fraction are shown in the 1D histograms as shaded regions but are not shown in the 2D histogram. Uncertainties for both scale as σ_f/c, where σ_f is the uncertainty from the binomial process on each measurement,

$$\sigma_f = \sqrt{\frac{f(1-f)}{N}} \tag{3.4}$$

where N is the total number of objects in each bin. As noted in C. N. Mazzola et al. 2020, this method can result in bins with completeness-corrected close binary fractions that are larger than 100 per cent. We again assumed the same Raghavan et al. 2010 period distribution for all systems in our MC simulations, an assumption that may not be valid for the entirety of the APOGEE sample (Moe, Kaitlin M. Kratter, and Badenes 2019). Metal-poor eclipsing binaries have been found to be skewed towards shorter periods than metal-rich systems (Jayasinghe et al. 2021). A systematic shift at short periods produces an overcorrection from the completeness estimate and thus creates bins with excessively high close binary fractions. Future studies detailing the relationship between stellar chemistry and the period distribution will enable us to improve our completeness estimates.

As expected, the close binary fraction is strongly correlated with $v \sin i$. It is unclear whether a trend exists with $\tau_{\rm SD}$ from our figure, especially given the larger uncertainties. However, age has significant internal correlations with other parameters that do correlate with the close binary fraction, such as [Fe/H] and α process abundances, so a thorough multi-variate analysis is necessary to fully interpret this histogram. Despite this, the 2D histogram shows a clear age-dependent gradient in the close binary fraction across $v \sin i$, such that stars that are 10 Gyr old have notably larger fractions of close binaries at $v \sin i$ < 10 km s^{-1} than stars that are 3 Gyr.

Due to using only single star tracks, equal-mass binaries that are offset from the main sequence are expected to be biased towards very young (100s Myr) or very old (> 10 Gyr) $\tau_{\rm SD}$ estimates. Removing SB2s reduces the impact of these biases, but particularly for the oldest stars, we still expect some contamination from poorly-constrained binary $\tau_{\rm SD}$ in the age-dependence of the close binary fraction. However, we note that the gradient extends down into intermediate ages ($1 \lesssim \tau_{\rm SD}/{\rm Gyr} \lesssim 8$), where we expect relatively robust ages for binaries and single stars alike. To further check for biases from photometric binaries, we calculated a simple photometric offset $J_{\rm avg} - J_{\rm abs}$ from a line spanning the center of the main sequence, such that photometric binaries should have $J_{\rm avg} - J_{\rm abs} \gtrsim 0.5$. We colored the 2D histogram from Fig. 27 on the median photometric offset and found that stars with $\tau_{\rm SD} \gtrsim 9.5$ Gyr have systematically positive offsets of $J_{\rm avg} - J_{\rm abs} \approx 0.5$, as to be expected for the oldest stars moving towards the subgiant branch. However, the remaining portion of

the figure showed very small median offsets, with a median value of 0.05 for histogram bins between $4.5 \leq \tau_{\rm SD} < 9.5$ Gyr, a region where we still see the effects of the age gradient.

To compare this trend with predictions from gyrochronology, we use the relation from Barnes 2010,

$$\tau_{\rm gyro} = \frac{\tau_c}{k_{\rm C}} \ln\left(\frac{P_{\rm rot}}{P_0}\right) + \frac{k_{\rm I}}{2\tau_c}\left(P_{\rm rot}^2 - P_0^2\right) \tag{3.5}$$

where τ_c is the convective turnover timescale, P_0 is the initial period, and $k_{\rm C}$ and $k_{\rm I}$ are dimensionless constants. We adopt $\tau_c = 34.87$ days (Barnes and Kim 2010) and $P_0 = 1.1$ days (Saders et al. 2016). The orange lines in Fig. 27 show this relation for 1 $M_\odot$ and $\log(g/\text{cm s}^{-2}) = 4.0$ (lightest), 4.5, and 5.0 (darkest). Gyrochronology predicts that most old MS stars should be rotating slowly, but our data indicate that tidal interactions in close binary systems can keep older stars spinning faster than predicted. This manifests as a gradual increase in the close binary fraction across our measured rotation speeds as a function of stellar age.

We further explore these discrepancies with gyrochronology in the right side of the figure. We calculated $\tau_{\rm gyro}$ from equation (3.5) with each star's APOGEE $\log(g)$, our $v \sin i$, and Sanders et al. 2018 mass. The 2D histograms show the same binning scheme as before, but they are now colored by the median in the difference between the predicted gyrochronological age and the measured isochrone age, $|\tau_{\rm gyro} - \tau_{\rm SD}|$, and the median [Fe/H] of each bin. There is clear overlap in the bins with large close binary fractions and those with large age discrepancies, some on the order of 10 Gyr or more. This provides supporting evidence for the hypothesis that the components of wide-separation binaries with unusually fast rotation rates are due to effects of close binary companions (Godoy-Rivera and Chanamé 2018; Janes 2017). As expected, the oldest stars have lower median [Fe/H] values, and there is a modest bias towards lower [Fe/H] among the bins with large close binary fractions, in agreement with the well-established anti-correlation between the close binary fraction and metallicty (e.g. Moe, Kaitlin M. Kratter, and Badenes 2019). However, the differences in median [Fe/H] are small across much of the figure and thus unlikely to drive the observed trends. Calculating $\tau_{\rm gyro}$ with $5P_0$ and $0.2P_0$ did not significantly change our median differences in predicted and measured ages. Repeating this analysis using the threshold $\Delta\text{RV}_{\rm max} \geq 10$ km s^{-1} and detection efficiency $c = 0.25$ removed five bins due to insufficient numbers of systems but

revealed the same trends in all panels of Fig. 27.

In a young field, rapid rotation is mostly a single star phenomenon, but in an old field, essentially all rapid rotators are binaries or merger products. This is evidenced by the similar fractions of rapid rotators ($v \sin i \geq 10$ km s^{-1}) but differences in RV variability for young and old stars within our sample; young stars ($0.5 \leq \tau_{\rm SD} < 3$ Gyr) have $N_{\rm fast}/N_{\rm tot} = 0.026 \pm 0.003$ and old stars ($\tau_{\rm SD} \geq 8$ Gyr) have $N_{\rm fast}/N_{\rm tot} = 0.031 \pm 0.003$, but Fig. 27 demonstrates significant differences in the close binary fraction between the rapid rotators of these two age groups. Those wishing to apply gyrochronology relations to cool MS stars should thus be cautious and consider taking several spectra for each target to remove the RV variables, particularly for metal-poor samples, or consider using Gaia RUWE statistics to infer photcenter wobble (Belokurov et al. 2020).

3.4 Conclusions

We have explored the connection between multiplicity and rotation across stellar lifetimes. Using a sample of 24 496 dwarfs and 2786 giants from APOGEE DR14, we measured trends between the maximum RV shift, $\Delta{\rm RV}_{\rm max}$, effective gravity $\log(g/{\rm cm\ s}^{-2})$, and projected rotation speeds $v \sin i$, and we interpreted these trends through the application of theoretical upper limits calculated using a simple set of assumptions. By assuming rotational synchronization and that the minimum allowed period is the critical period for Roche Lobe overflow, $\rm P_{crit}$, we calculated theoretical upper limits on rotational speeds and $\Delta{\rm RV}_{\rm max}$, which were able to explain the maximum extent of our data across several $\log(g)$ bins. We simulated populations of binaries using a Monte Carlo sampler and compared their simulated $\Delta{\rm RV}_{\rm max}$ distributions to the slow and rapid rotators in our APOGEE data. The distributions for rapid rotators in our sample were consistent with those from the shortest-period binaries in our simulation, supporting the idea that rapid rotators are more likely to possess a close companion. We also see evidence for this in dwarfs below the Kraft break: older stars show increased close binary fractions across the entire range of $v \sin i$ values. Older, rapidly rotating stars have particularly large close binary fractions and correspondingly large differences

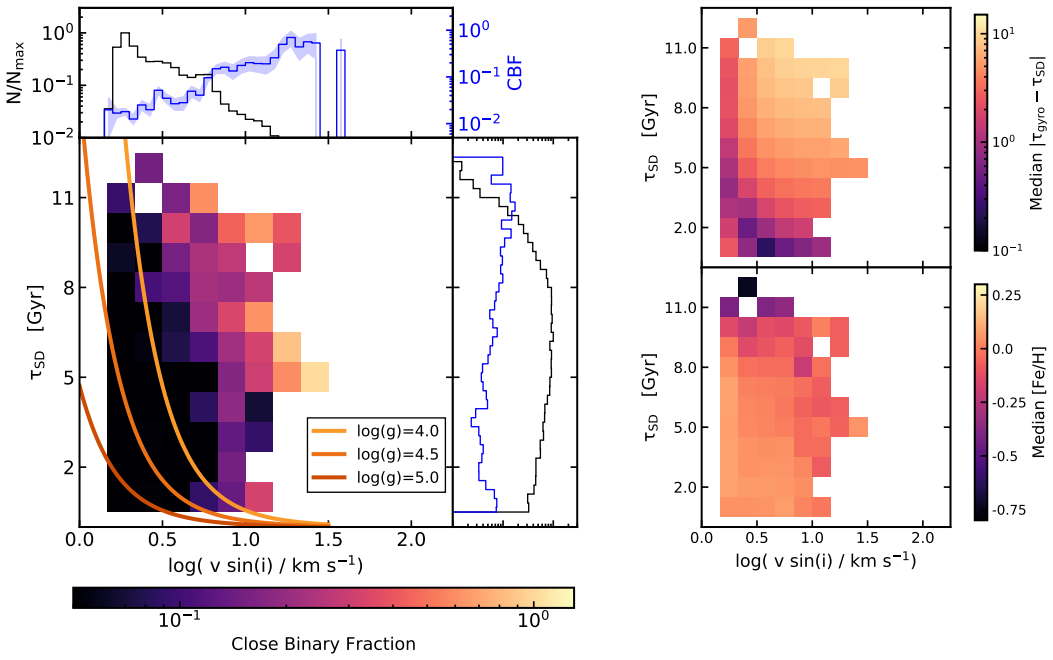

Figure 27: Left: Two-dimensional histogram showing the completeness-corrected close binary fraction as a function of stellar age $\tau_{\rm SD}$ and rotation speed $\log(v \sin i$ / km s$^{-1})$ for dwarfs with $T_{\rm eff}<$ 6250 K (below the Kraft break). The orange lines indicate the gyrochronology relation of Barnes 2010 for 1 M$_\odot$ and $\log(g/{\rm cm\ s^{-2}}) = 4.0$ (lightest), 4.5, and 5.0 (darkest). The side panels show the normalized histogram (black) and completeness-corrected close binary fraction (blue) for each parameter alone. Blue shading indicates the uncertainties on the completeness-corrected close binary fraction. Right: The same binning scheme as the left panel, but now showing the median in the difference between predicted age and measured age, $|\tau_{\rm gyro} - \tau_{\rm SD}|$, and the median [Fe/H] of the stars in that bin.

between their predicted gyrochronological ages and those measured by isochrone fits. Rotationally synchronized binaries present an ongoing challenge for gyrochronology, but great progress can be made to characterize these systems from the intersection of spectroscopic, photometric, and astrometric observations enabled by modern surveys of field stars.

4.0 Uncovering Binary Formation Channels in Low-Mass Stars

Interacting binaries are the progenitors a wide range of astrophysical transients, including all Type Ia and most core collapse supernovae, cataclysmic variables, novae, low- and high-mass X-ray binaries, and most stellar sources of gravitational waves (for a review, see De Marco et al. 2017). The occurrence rates of these sources depend on the initial conditions that govern their progenitors: the multiplicity fraction and the distributions of periods, mass ratios, and eccentricities, which together form the fundamental statistics of stellar multiplicity. However, the accurate characterization of these distributions is complicated by the realization that they are strong functions of stellar properties and not independent of one another (for reviews, see Duchêne et al. 2013; Moe and Di Stefano 2017). Fortunately, the combination of Gaia astrometry and modern spectroscopic surveys now offers the most comprehensive view of the stellar content of the Milky Way and the Local Group to date. As spectroscopy remains the most efficient method for identifying close ($\log P/\mathrm{d} \lesssim 4$), unresolved binaries, these data provide the necessary leverage to disentangle the complex correlations between stellar properties and multiplicity statistics in the field.

The Apache Point Galactic Evolution Experiment 2 (APOGEE-2; Majewski et al. 2017), a constituent survey of the fourth Sloan Digital Sky Survey (SDSS-IV; Blanton et al. 2017; Gunn et al. 2006), has taken multi-epoch spectra for hundreds of thousands of stars across all major populations of the Milky Way with its dual high-resolution ($R \sim 22500$), multiplexed, near-infrared spectrographs (Wilson et al. 2019) in the northern and southern hemispheres. Precise radial velocities (RVs) are measured from individual visit spectra (Nidever et al. 2015), and the visit spectra are stacked into a higher-S/N combined spectrum from which reliable stellar parameters are determined by the APOGEE Stellar Parameter and chemical Abundances Pipeline (ASPCAP; García Pérez et al. 2016; Jönsson, Holtzman, et al. 2020).

Prior work has established a strong anti-correlation between the close binary fraction and metallicity, including several studies involving APOGEE giants and dwarfs (see Badenes, C. Mazzola, et al. 2018; C. N. Mazzola et al. 2020; Moe, Kaitlin M. Kratter, and Badenes 2019; A. M. Price-Whelan, Hogg, Rix, Beaton, et al. 2020, and sources cited within). This

trend profoundly affects the rates of interacting binaries (e.g. De Marco et al. 2017; A. Price-Whelan et al. 2019; Stanway et al. 2020), but it also sheds light on the formation mechanisms of binaries (e.g. Duchêne et al. 2013; Kounkel, K. Covey, et al. 2019; Kaitlin M. Kratter, Matzner, et al. 2010; Moe and Di Stefano 2017; Moe and Kaitlin M. Kratter 2018). In particular, the complex relationship between the close binary fraction, α abundances, and metallicity discovered by C. N. Mazzola et al. 2020 provides observational evidence for the role played by icy and dusty grains on the fragmentation of protostellar discs, in agreement with the predictions of analytical models and hydrodynamical simulations of close binary formation(Machida et al. 2009; Moe, Kaitlin M. Kratter, and Badenes 2019; Tanaka et al. 2014).

In the context of these discoveries, the metallicity-dependence of the M-dwarf close binary fraction is particularly important; a correlation (or lack thereof) reveals insight into the fragmentation physics of low-mass protostellar discs and help distinguish between possible explanations for the apparent floor in the close binary fraction of $\sim 10\%$ (C. N. Mazzola et al. 2020). To answer these questions, this paper aims to characterize the relationship between RV variability and metallicity for M-dwarfs, compare it to the well-established anti-correlations for GK dwarfs, and consider the implications for binary formation theory. We describe our method of selecting GKM dwarfs using public data from APOGEE and Gaia Early Data Release 3 in Section 4.1, present our results in Section 4.2, and briefly discuss these preliminary findings in Section 4.3.

4.1 Sample Selection

We use the spectral parameters from the APOGEE Data Release 17 `allStar` file (Abdurro'uf et al. 2022; Holtzman et al., in prep), which has 733 901 total entries corresponding to 657 135 unique APOGEE IDs. Individual observations are identified by the fiber plugplate used to observe them, with each plugplate corresponding to a unique field center. ASPCAP does not automatically combine all visit spectra with the same APOGEE ID but different fields, occasionally leading to multiple `allStar` entries with the same APOGEE ID. Thus,

Table 8: General properties of the dwarf sub-samples.

Spectral Type	$T_{\rm eff}$ Range	$\log(g/{\rm cm\ s^{-2}})$ Range	N	$N_{\rm RV\ variable}$[1]
G	5325 – 5960	3.55 – 4.75	31965	2625
K	3890 – 5325	4.15 – 5.26	36540	3422
M0-2	3500 – 3890	4.36 – 5.20	4033	511

a given combined spectrum and its derived stellar parameters can be uniquely identified through the combination of its APOGEE ID and field location ID.

We implemented several quality cuts to clean the data. These included removing stars with the STAR_BAD flag set in the ASPCAP bitmask (Holtzman, Shetrone, et al. 2015); commissioning observations (bit 1 in STARFLAG, ibid.); telluric calibrators (bit 9 in both the apogee target2 and apogee2 target2 masks Zasowski, Cohen, et al. 2017; Zasowski, Johnson, et al. 2013); and known cluster members (bit 9 in APOGEE_TARGET1 and APOGEE2_TARGET1 and bit 10 in APOGEE_TARGET2 and APOGEE2_TARGET2, Zasowski, Cohen, et al. 2017; Zasowski, Johnson, et al. 2013). We also required that stars have well measured ($\neq -9999$, the default for a bad value) metallicities ([Fe/H]), Bailer-Jones *Gaia* Early DR3 distances (Bailer-Jones et al. 2021), and calibrated effective temperatures ($T_{\rm eff}$) and surface gravities [$\log(g)$].

For each APOGEE ID, we identified all of the visit entries from the DR17 `allVisit` file that were included in its combined spectrum via its VISITS_PK indices (Holtzman, Shetrone, et al. 2015; Nidever et al. 2015) and required that two or more visit spectra had S/N$\geq$ 40. For duplicated APOGEE IDs, we concatenated all the visits with different field location IDs, meaning that a star with at least one good visit in two or more fields also passed our quality cut. We averaged the stellar parameters in the cases where stars had multiple valid ($\neq -9999$) values from their multiple `allStar` entries.

Our quality-cut sample contained 305 345 stars spanning the main sequence (MS), giant

[1]Here, a star is considered RV variable if $\Delta{\rm RV_{max}} > 1$ km s^{-1}, though the choice of $\Delta{\rm RV_{max}}$ threshold depends on the stellar properties of the sample (for a discussion, see C. N. Mazzola et al. 2020).

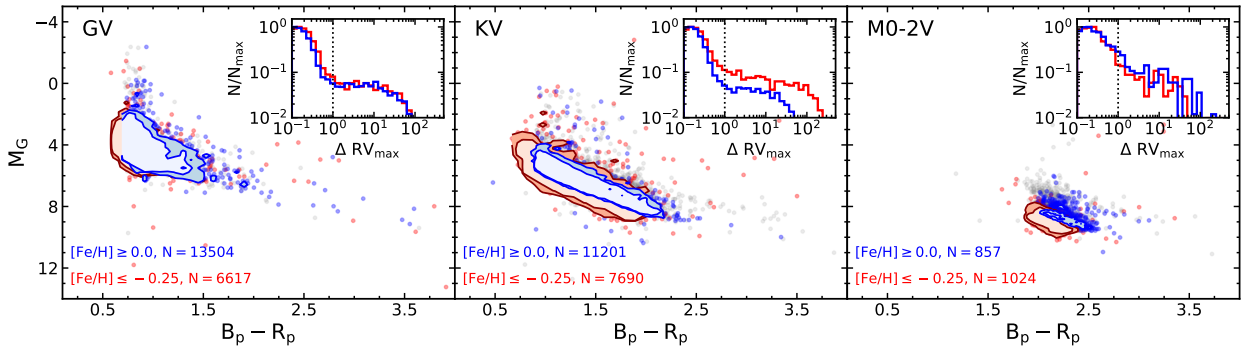

Figure 28: Gaia CMD for our various dwarf samples. We compare the CMDs for low-[Fe/H] (red) and high-[Fe/H] (blue) sub-samples, with the number of stars in each provided in the bottom left corner. The inset figure shows the normalized ΔRV_{max} histograms for the low-and high-metallicity sub-samples.

branch, and red clump. To restrict our sample to dwarfs, we calculated a lower limit on MS $\log(g)$, as a function of $T_{\rm eff}$, by using the predicted $\log(g)$ and $T_{\rm eff}$ values of terminal-age MS stars from the most metal-rich ([Fe/H]= 0.50) evolutionary tracks of the MESA Isochrone and Stellar Tracks Collaboration (MIST; Choi et al. 2016; Dotter 2016; Paxton, Bildsten, et al. 2011; Paxton, Cantiello, et al. 2013; Paxton, Marchant, et al. 2015). We identified dwarfs as stars with APOGEE $\log(g)$ larger than the minimum predicted $\log(g)$. Following the spectral classifications of Pecaut et al. 2013, we further classify our dwarfs into GV, KV, or MV based on the $T_{\rm eff}$ bins listed in Table 8.

The primary scientific goal of APOGEE was to conduct galactic archaeology with red giants, so ASPCAP is naturally optimized to fit the parameters of giants. There are some known calibration issues for M dwarfs (Souto, Cunha, Smith, C. Allende Prieto, Burgasser, et al. 2020; Souto, Cunha, Smith, C. Allende Prieto, K. Covey, et al. 2022), and given that ASPCAP simultaneously fits for seven stellar parameters ($T_{\rm eff}$, $\log(g)$, [M/H], [α/M], [C/M], [N/M], microturbulent velocity, and stellar rotation $v \sin i$), issues with any one of these stellar parameters may permeate to the other six. As an independent check on the APOGEE metallicities, we plot absolute *Gaia* magnitudes M_G versus *Gaia* color $B_p - R_p$ for our GKM dwarfs and color each by low- and high-metallicity in Fig. 28. The low- and high-metallicity M dwarfs separate out well, indicating that the metallicities are reasonable enough to preserve general trends across our statistical sample.

The inset figure in Fig. 28 displays the normalized histogram of ΔRV_{max} for the low- and high-metallicity sub-samples in each spectral class. As seen in previous studies (Badenes, C. Mazzola, et al. 2018; Daher et al. 2022; Maoz et al. 2012; C. N. Mazzola et al. 2020), the distributions consist of a low-ΔRV_{max} "core" primarily composed of RV uncertainties and a tail of large-ΔRV_{max} systems dominated by short-period binaries. The width of the core is indicative of the RV uncertainties, and larger RV uncertainties are known to be correlated to stellar properties such as evolutionary state and metallicity. We refer readers to (Badenes, C. Mazzola, et al. 2018) for a full discussion and instead only make a few observations relevant to the current work.

First, our M dwarfs appear to have a larger core and thus larger RV uncertainties than the GK samples; this is unsurprising given they are fainter and we have not controlled for S/N or apparent magnitudes between the spectral samples. Despite the larger RV errors in M dwarfs, all three samples show a clear transition between core and tail at or before the dotted line at $\Delta RV_{max} = 1$ km s^{-1}, so we choose to use $\Delta RV_{max} \geq 1$ km s^{-1} as our threshold for RV variability.

Second, there is a significant difference in the tails of the low- and high-metallicity sub-samples of K dwarfs, consistent with the anticorrelation between metallicity and the close binary fraction. Curiously, we do not see this same effect in the GV or MV samples. We further explore these trends and consider their consequences for star formation in the remainder of this paper.

4.2 Results

In Fig. 29, we compare the RV variability fractions as a function of [Fe/H] (left), [M/H] (middle), and [α/H] (right) for each spectral class, with error bars given by the binomial process uncertainty,

$$\sigma = \sqrt{\frac{f_{\mathrm{RVvar}}(1 - f_{\mathrm{RVvar}})}{N}} \tag{4.1}$$

where f_{RVvar} is the fraction of systems with $\Delta RV_{max} \geq 1$ km s^{-1} and N is the total number of systems in that bin. The KV sample again demonstrates a strong anticorrelation across

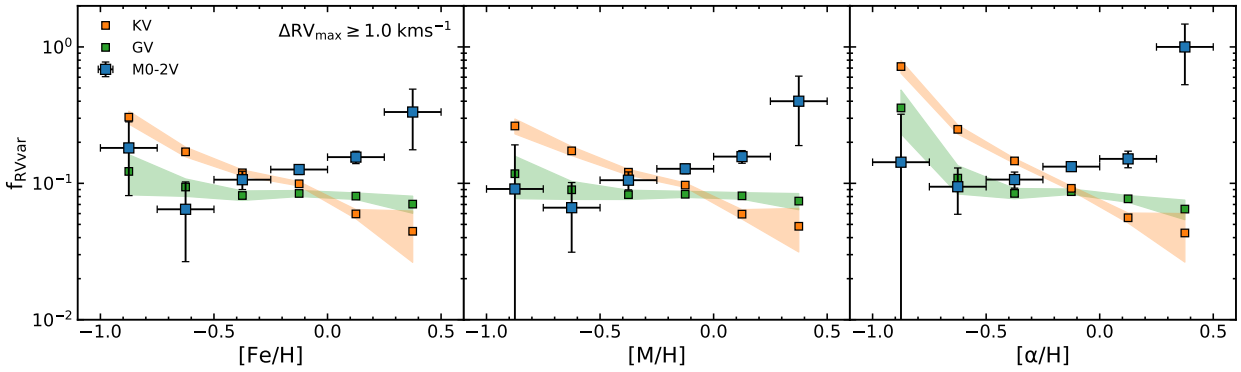

Figure 29: RV variability fractions for various spectral types as a function of [Fe/H] (left), [M/H] (middle), and [α/H] (right). Uncertainties are indicated by shading on the K and G dwarfs and error bars on M dwarfs for visual clarity.

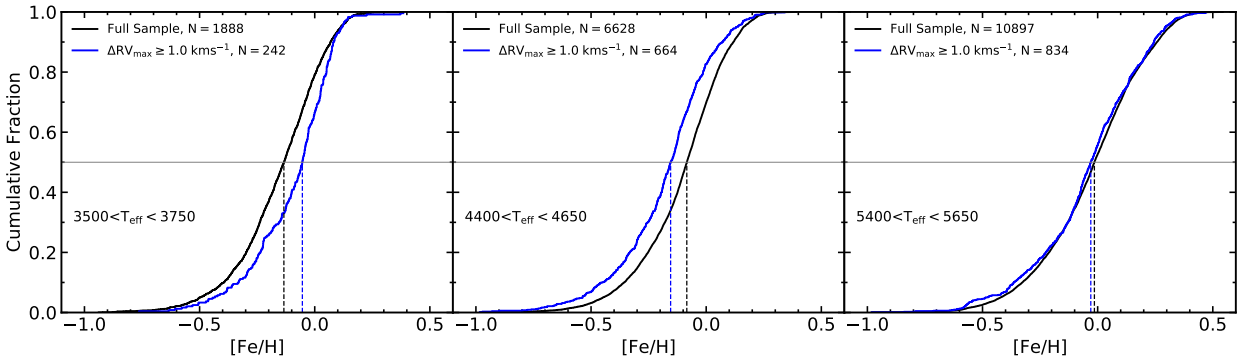

Figure 30: Cumulative distributions of [Fe/H] for several $T_{\rm eff}$ bins that contain MV stars (left), KV stars (center), and GV stars (right). Black indicates the full sample and blue the stars with $\Delta \mathrm{RV}_{\rm max} \geq$ 1.0 km s^{-1}. The gray horizontal line is drawn at a cumulative fraction of 50%, with the corresponding [Fe/H] value indicated by the dashed lines in the respective colors for the full sample and RV variables.

all three abundances. The GV sample shows no significant correlations, except perhaps for the two lowest [α/H] points. By contrast, the M dwarfs appear to show a positive correlation across all three abundances; though the end points have very large uncertainties, the trends are consistent across the three central points with much smaller error bars.

In order to avoid binning our data in metallicity, we instead compare the cumulative metallicity distributions of stars with $\Delta \mathrm{RV}_{\rm max} \geq 1$ km s^{-1} to the distributions of the full sub-sample. Rather than just compare the spectral class samples, we iteratively define bins in $T_{\rm eff}$ from a bin center T_i, a bin width β, and a step width ω. First, we define a sub-sample with $T_i - (\beta/2) \leq T_{\rm eff} < T_i + (\beta/2)$. We plot the cumulative distributions for the full sub-sample and the RV variables, then use an interpolating function to determine the [X/H] value that corresponds to a cumulative fraction (CF) of 0.5 in both distributions. Finally, we re-define the bin center as $T_{i+1} = T_i + \omega$ and repeat until $T_n + (\beta/2) > 6000$ K.

Fig. 30 shows a few of the cumulative [Fe/H] distributions output by this procedure using $\beta = 250$ K, $\omega = 100$ K, and a starting bin center $T_0 = 3625$ K. In the lowest $T_{\rm eff}$ bin (left panel), the RV variables are shifted towards larger metallicities than the full sample, reflected in the larger [Fe/H] value corresponding to CF=0.5 (vertical dashed lines). The middle panel shows the opposite trend, consistent with the strong anti-correlation in the KV sample, whereas there is no significant difference between the distributions in the right

panel, also consistent with the weak trends seen in the GV sample.

We then take the differences between the [Fe/H] values corresponding to CF= 0.5 for all of the bins and plot them as a function of $T_{\rm eff}$ in Fig. 31. We compare the results for [Fe/H] (black points), [M/H] (red dotted line), and [α/H] (blue dashed line) and find the same general trend: cool RV variables are shifted towards higher metal content until a transition point of $T_{\rm eff} \approx 3800$ K ($M \approx 0.45$ M$_\odot$), and an inflection point around $T_{\rm eff} \approx 4750$ K ($M \approx 0.8$ M$_\odot$) leads to progressively smaller differences for G-type dwarfs.

4.3 Discussion and Conclusions

These results are particularly interesting in the context of binary formation mechanisms. Protostellar disc fragmentation is believed to be one of the primary formation channels of close binaries (separations $a < 10$ au), and star formation models indicate that fragmentation increases as the discs become more massive, so long as they are massive enough to form stars with $M \gtrsim 0.8$ M$_\odot$ (Kaitlin M. Kratter and Matzner 2006), and as the metallicity of the gas decreases (Bate 2019; Machida et al. 2009; Moe, Kaitlin M. Kratter, and Badenes 2019; Tanaka et al. 2014). These two effects should cause the close binary fraction be correlated with primary mass and anticorrelated with metallicity, respectively; both of these predictions have been supported by considerable observational evidence throughout the years (see Moe and Di Stefano 2017 and Moe, Kaitlin M. Kratter, and Badenes 2019 for reviews).

The weakening correlation with metallicity for our early G dwarfs suggests a transition in regimes between these two effects. Perhaps K-type close binary formation depends primarily on metallicity-driven fragmentation, whereas G-type primaries become progressively less reliant on metallicity due to their more massive protostellar discs. This is further supported by the fact that the inflection in Fig. 31 occurs around $M \approx 0.8$ M$_\odot$, in agreement with both theoretical predictions and previous observations.

Previous studies have also found a "floor" in the close binary fraction of $\approx 10\%$ for metal-rich Sun-like stars (e.g., C. N. Mazzola et al. 2020) and M-dwarfs and brown dwarfs (Joergens 2008; Moe 2019; Moe and Di Stefano 2017; Murphy et al. 2018; Winters et al. 2019). One

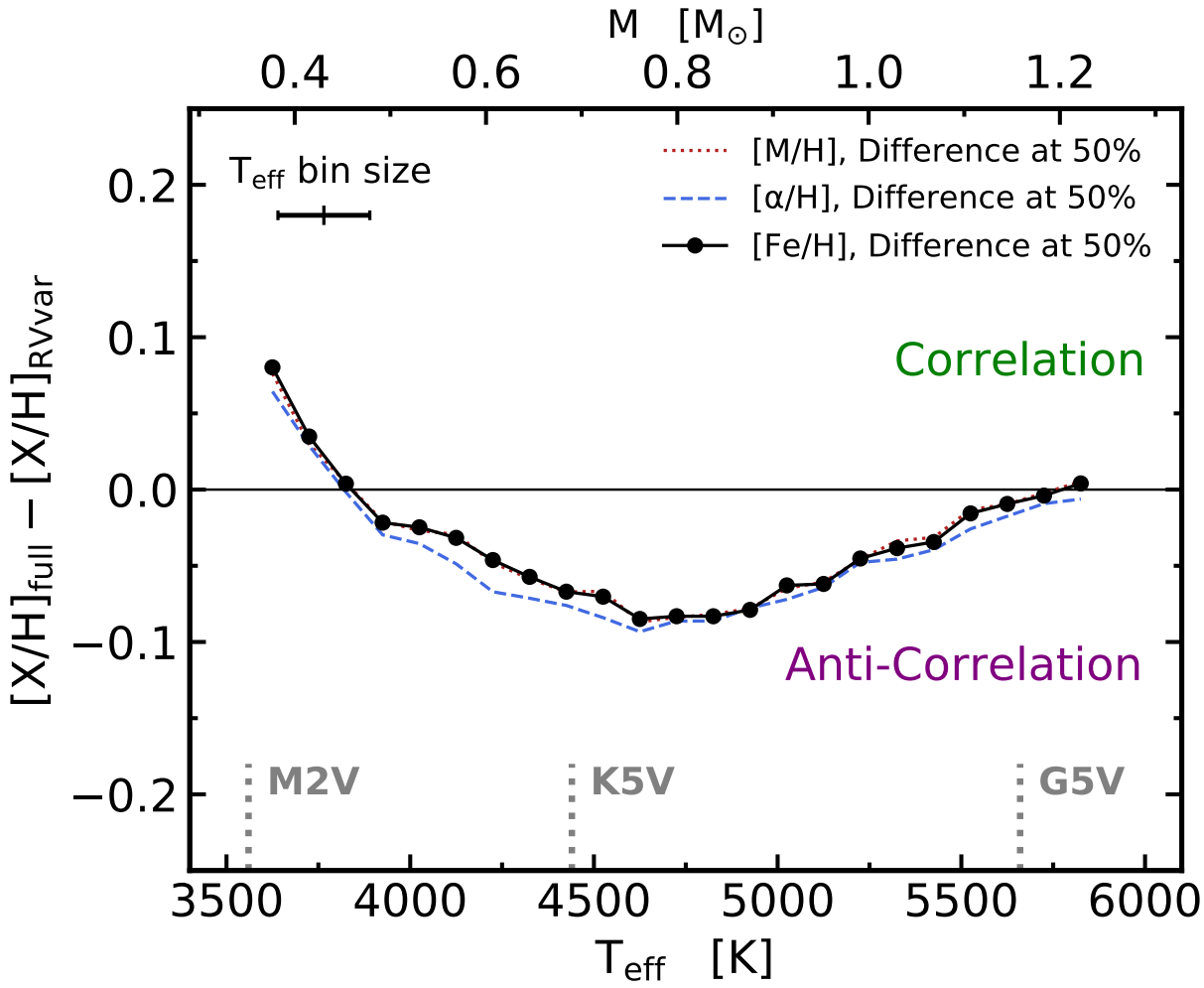

Figure 31: Difference between the [Fe/H] value at cumulative fraction = 0.5 for the full sample and for stars with $\Delta RV_{max} \geq$ 1.0 km s^{-1}. Each point is for a different T_{eff} bin with a width of 250 K and bin centers iteratively shifted in steps of 100 K. The black points are for [Fe/H], while the red and blue lines show the same relation for [M/H] and [α/H] respectively. The top axis relates stellar mass to T_{eff} for [Fe/H]= 0.0 dwarfs from the Baraffe stellar evolutionary tracks (Baraffe et al. 2015). The horizontal line at 0.0 is included to emphasize the crossover points.

possible explanation is that metal-rich and/or low-mass discs are entirely unsusceptible to fragmentation and so close binaries form through other means, such as core fragmentation followed by inward migration due to dynamical friction. This hypothesis should lead to no significant correlation between the close binary fraction and metallicity for M dwarfs. Alternatively, perhaps $\approx 10\%$ of protostellar discs are unstable enough to fragment early on in their accretion, regardless of disc chemistry or the resulting primary masses. In this scenario, the floor of 10% will exist regardless of other effects that may lead to correlations or anticorrelations with the close binary fraction.

Our RV variability fractions again demonstrate a floor of $\approx 10\%$, lending credence to the second possible explanation, but the significant correlation with chemistry demonstrated by our M dwarfs appears to rule out the first hypothesis. Naively, one might expect larger quantities of dust and icy grains to help protostellar discs radiate away heat more efficiently, cooling the disc faster and thus increasing the fragmentation rate. This would imply a positive correlation with Fe and particularly α abundances like O and Si, at odds with the general consensus of an anticorrelation. However, C. N. Mazzola et al. 2020 noted that the close binary fractions as a function of overall α, O, and Si were non-monotonic – they were strongly anti-correlated until an inflection point of $\approx 10\%$ around 0.075 dex in all three abundances, at which point the close binary fraction *increased*. Perhaps the protostellar discs capable of forming K dwarf primaries are far more sensitive to the effects linked to low-metallicity than the discs forming M dwarf primaries, or perhaps dynamical interactions and mergers play a more complex role at these low masses. Deeper investigations into simulations of star formation may reveal insight into the magnitude of these effects and the regimes where they are most impactful, and a closer comparison of our preliminary results to these simulations is the subject of ongoing work.

5.0 Conclusions

Many questions remain to be considered, and I will briefly touch on some of the potential avenues for future projects below, roughly organized by chapter.

From Chapter 2, a key prediction from recent star formation models is a bias towards shorter orbital periods among metal-poor stars. Using an orbital sampler such as *The Joker*, I hope to explore whether the period distribution varies with α-abundances and especially carbon, given that molecular carbon monoxide transitions are a dominant source of radiative cooling in protostellar cores. Characterizing the period distribution's dependence on chemistry is also critically important for interpreting the rate of interacting binaries and their resulting astrophysical transients, observations that are poised to flourish in the upcoming era of LSST/VRO. It is also a particularly exciting time for galactic archaeology; APOGEE's successor, the SDSS-V Milky Way Mapper survey, has begun operations within the last year, with plans to take near-infrared and/or optical spectra of more than 4 million stars throughout the Milky Way, including a volume-limited sample out to 100 pc.

A particularly large number of opportunities were leftover from the work in Chapter 3. First, some of the stars from my giants sample in Fig. 25 had $v \sin i$ close to or above the predicted upper limit for tidal interactions, despite having $\Delta \mathrm{RV}_{\mathrm{max}}$ values that are more likely due to measurement uncertainty or RV jitter than a short-period companion. If indeed lacking a close companion, they must have been hyper-rotating main sequence stars for their current $v \sin i$ to be the result of natural spin-down. Alternatively, these may be true binaries with unfortunately sampled RV curves, and additional RV follow-up should be able to confirm or rule out this possibility. Another explanation is that these systems are the result of stellar mergers and were spun-up from their engulfed companion's angular momentum. In addition to rapid rotation, they may display chemical signatures of the engulfment that are distinguishable by APOGEE spectra.

Second, a subset of stars in Fig. 25 have $v \sin i$ and $\Delta \mathrm{RV}_{\mathrm{max}}$ values that are comparable to the diagonal lines. These are all excellent candidates to test for orbital synchronization, provided I can obtain orbital and rotational periods. Orbital periods could be found for

these systems using an orbital sampler such as *The Joker*, though some may need targeted RV follow-up for such samplers to provide meaningful constraints. Rotation periods could be found from $v \sin i$ with high uncertainty or from photometry. It is worth noting that photometric periods may prove difficult, as these systems are also likely to be actively interacting and may show signs of interaction through complex photometric variability. However, the characterization of these photometric signatures is likely an interesting endeavor of its own.

As Chapter 4 is still preliminary, I will refrain from commenting on further work here and reserve those remarks to my personal checklist for the near future.

Finally, several outstanding groups of stars have consistently surfaced in APOGEE samples that warrant further study. The $\Delta\mathrm{RV}_{\mathrm{max}}$ distributions of red clump stars largely follow those of giants near the tip of the red giant branch, but a group of highly-RV-variable red clump stars have reportedly appeared across both APOGEE and TESS samples. Additionally, there exists a significant population of distinctly RV variable stars to the right of the giant branch in all of the HR diagrams I include in this dissertation. From their location, I suspect these may be sub-subgiant stars, and if so, their enhanced RV variability may shed light on their formation channels (Geller, E. M. Leiner, Bellini, et al. 2017; Geller, E. M. Leiner, Chatterjee, et al. 2017; E. Leiner, Mathieu, and Geller 2017).

6.0 Bibliography

[1] Abdurro'uf et al. "The Seventeenth Data Release of the Sloan Digital Sky Surveys: Complete Release of MaNGA, MaStar, and APOGEE-2 Data". In: *The Astrophysical Journal Supplement Series* 259.2, 35 (Apr. 2022), p. 35.

[2] Bela Abolfathi et al. "The Fourteenth Data Release of the Sloan Digital Sky Survey: First Spectroscopic Data from the Extended Baryon Oscillation Spectroscopic Survey and from the Second Phase of the Apache Point Observatory Galactic Evolution Experiment". In: *The Astrophysical Journal Supplement Series* 235.2 (Apr. 2018), p. 19.

[3] Franco D. Albareti et al. "The 13th Data Release of the Sloan Digital Sky Survey: First Spectroscopic Data from the SDSS-IV Survey Mapping Nearby Galaxies at Apache Point Observatory". In: *The Astrophysical Journal Supplement Series* 233.2 (Dec. 2017), p. 25.

[4] Ruth Angus, Suzanne Aigrain, et al. "Calibrating gyrochronology using Kepler asteroseismic targets". In: *Monthly Notices of the Royal Astronomical Society* 450.2 (Apr. 2015), pp. 1787–1798.

[5] Ruth Angus, Angus Beane, et al. "Exploring the Evolution of Stellar Rotation Using Galactic Kinematics". In: *The Astronomical Journal* 160.2 (July 2020), p. 90.

[6] Ruth Angus, Timothy D. Morton, et al. "Toward Precise Stellar Ages: Combining Isochrone Fitting with Empirical Gyrochronology". In: *The Astronomical Journal* 158.5 (Oct. 2019), p. 173.

[7] Carles Badenes and Dan Maoz. "THE MERGER RATE OF BINARY WHITE DWARFS IN THE GALACTIC DISK". In: *The Astrophysical Journal* 749.1 (Mar. 2012), p. L11.

[8] Carles Badenes, Christine Mazzola, et al. "Stellar Multiplicity Meets Stellar Evolution and Metallicity: The APOGEE View". In: *The Astrophysical Journal* 854.2 (Feb. 2018), p. 147.

[9] K. El-Badry et al. “Signatures of unresolved binaries in stellar spectra: implications for spectral fitting”. In: *Monthly Notices of the Royal Astronomical Society* 473 (Feb. 2018), pp. 5043–5049.

[10] Kareem El-Badry and Hans-Walter Rix. “The wide binary fraction of solar-type stars: emergence of metallicity dependence at a < 200 AU”. In: *Monthly Notices of the Royal Astronomical Society* 482 (Nov. 2018), p. L139.

[11] Kareem El-Badry, Hans-Walter Rix, et al. “Discovery of an equal-mass ‘twin’ binary population reaching 1000 + au separations”. In: *Monthly Notices of the Royal Astronomical Society* 489.4 (Sept. 2019), pp. 5822–5857.

[12] Kareem El-Badry, Yuan-Sen Ting, et al. “Discovery and characterization of 3000+ main-sequence binaries from APOGEE spectra”. In: *Monthly Notices of the Royal Astronomical Society* 476.1 (Jan. 2018), pp. 528–553.

[13] C. A. L. Bailer-Jones et al. “Estimating Distances from Parallaxes. V. Geometric and Photogeometric Distances to 1.47 Billion Stars in Gaia Early Data Release 3”. In: *The Astronomical Journal* 161.3 (Feb. 2021), p. 147.

[14] Isabelle Baraffe et al. “New evolutionary models for pre-main sequence and main sequence low-mass stars down to the hydrogen-burning limit”. In: *Astronomy & Astrophysics* 577, A42 (May 2015), A42.

[15] Sydney A. Barnes. “A SIMPLE NONLINEAR MODEL FOR THE ROTATION OF MAIN-SEQUENCE COOL STARS. I. INTRODUCTION, IMPLICATIONS FOR GYROCHRONOLOGY, AND COLOR-PERIOD DIAGRAMS”. In: *The Astrophysical Journal* 722.1 (Sept. 2010), pp. 222–234.

[16] Sydney A. Barnes. “Ages for Illustrative Field Stars Using Gyrochronology: Viability, Limitations, and Errors”. In: *The Astrophysical Journal* 669.2 (Nov. 2007), pp. 1167–1189.

[17] Sydney A. Barnes and Yong-Cheol Kim. “ANGULAR MOMENTUM LOSS FROM COOL STARS: AN EMPIRICAL EXPRESSION AND CONNECTION TO STELLAR ACTIVITY”. In: *The Astrophysical Journal* 721.1 (Aug. 2010), pp. 675–685.

[18] Matthew R. Bate. “The statistical properties of stars and their dependence on metallicity”. In: *Monthly Notices of the Royal Astronomical Society* 484.2 (Jan. 2019), pp. 2341–2361.

[19] Matthew R. Bate. “The statistical properties of stars and their dependence on metallicity: the effects of opacity”. In: *Monthly Notices of the Royal Astronomical Society* 442.1 (June 2014), pp. 285–313.

[20] Vasily Belokurov et al. “Unresolved stellar companions with Gaia DR2 astrometry”. In: *Monthly Notices of the Royal Astronomical Society* 496.2 (June 2020), pp. 1922–1940.

[21] M. R. Blanton et al. “Sloan Digital Sky Survey IV: Mapping the Milky Way, Nearby Galaxies, and the Distant Universe”. In: *The Astronomical Journal* 154, 28 (July 2017), p. 28.

[22] Jo Bovy et al. “THE APOGEE RED-CLUMP CATALOG: PRECISE DISTANCES, VELOCITIES, AND HIGH-RESOLUTION ELEMENTAL ABUNDANCES OVER A LARGE AREA OF THE MILKY WAY’S DISK”. In: *The Astrophysical Journal* 790.2 (July 2014), p. 127.

[23] Katelyn Breivik et al. “COSMIC Variance in Binary Population Synthesis”. In: *The Astrophysical Journal* 898.1 (July 2020), p. 71.

[24] Bruce W. Carney et al. “Spectroscopic Binaries, Velocity Jitter, and Rotation in Field Metal-poor Red Giant and Red Horizontal-Branch Stars”. In: *The Astronomical Journal* 125.1 (Jan. 2003), pp. 293–321.

[25] Jieun Choi et al. “MESA ISOCHRONES AND STELLAR TRACKS (MIST). I. SOLAR-SCALED MODELS”. In: *The Astrophysical Journal* 823.2 (May 2016), p. 102.

[26] C. J. Clarke. “Pseudo-viscous modelling of self-gravitating discs and the formation of low mass ratio binaries”. In: *Monthly Notices of the Royal Astronomical Society* 396.2 (June 2009), pp. 1066–1074.

[27] Christine Mazzola Daher et al. “Stellar multiplicity and stellar rotation: insights from APOGEE”. In: *Monthly Notices of the Royal Astronomical Society* 512.2 (Mar. 2022), pp. 2051–2061.

[28] Orsola De Marco et al. “Dawes Review 6: The Impact of Companions on Stellar Evolution”. In: *Publications of the Astronomical Society of Australia* 34 (2017).

[29] S. E. de Mink et al. “MERGER RATES OF DOUBLE NEUTRON STARS AND STELLAR ORIGIN BLACK HOLES: THE IMPACT OF INITIAL CONDITIONS ON BINARY EVOLUTION PREDICTIONS”. In: *The Astrophysical Journal* 814.1 (Nov. 2015), p. 58.

[30] Don Dixon et al. “Rotationally Driven Ultraviolet Emission of Red Giant Stars”. In: *The Astronomical Journal* 160.1 (June 2020), p. 12.

[31] Aaron Dotter. “MESA ISOCHRONES AND STELLAR TRACKS (MIST) 0: METHODS FOR THE CONSTRUCTION OF STELLAR ISOCHRONES”. In: *The Astrophysical Journal Supplement Series* 222.1 (Jan. 2016), p. 8.

[32] Caitlin Doughty et al. “The effects of binary stars on galaxies and metal-enriched gas during reionization”. In: *Monthly Notices of the Royal Astronomical Society* 505.2 (May 2021), pp. 2207–2223.

[33] Gaspard Duchêne et al. “Stellar Multiplicity”. In: *Annual Review of Astronomy and Astrophysics* 51.1 (Aug. 2013), pp. 269–310.

[34] A. Duquennoy et al. “Multiplicity among solar-type stars in the solar neighbourhood. II - Distribution of the orbital elements in an unbiased sample”. In: *Astronomy & Astrophysics* 248 (1991), p. 485.

[35] B. R. Durney et al. “On the angular momentum loss of late-type stars.” In: *Geophysical and Astrophysical Fluid Dynamics* 9 (Jan. 1978), pp. 241–255.

[36] P. P. Eggleton. “Approximations to the radii of Roche lobes”. In: *The Astrophysical Journal* 268 (May 1983), p. 368.

[37] Courtney R. Epstein et al. “HOW GOOD A CLOCK IS ROTATION? THE STELLAR ROTATION-MASS-AGE RELATIONSHIP FOR OLD FIELD STARS”. In: *The Astrophysical Journal* 780.2 (Jan. 2014), p. 159.

[38] Robert T. Fisher. “A Turbulent Interstellar Medium Origin of the Binary Period Distribution”. In: *The Astrophysical Journal* 600.2 (Jan. 2004), pp. 769–780.

[39] F. Gallet et al. “Improved angular momentum evolution model for solar-like stars”. In: *Astronomy & Astrophysics* 556 (July 2013), A36.

[40] F. Gallet et al. “Improved angular momentum evolution model for solar-like stars”. In: *Astronomy & Astrophysics* 577 (May 2015), A98.

[41] Shuang Gao, Chao Liu, et al. “THE BINARITY OF MILKY WAY F,G,K STARS AS A FUNCTION OF EFFECTIVE TEMPERATURE AND METALLICITY”. In: *The Astrophysical Journal* 788.2 (June 2014), p. L37.

[42] Shuang Gao, He Zhao, et al. “The binarity of Galactic dwarf stars along with effective temperature and metallicity”. In: *Monthly Notices of the Royal Astronomical Society* 469 (May 2017), pp. L68–L72.

[43] Ana E. García Pérez et al. “ASPCAP: THE APOGEE STELLAR PARAMETER AND CHEMICAL ABUNDANCES PIPELINE”. In: *The Astronomical Journal* 151.6 (May 2016), p. 144.

[44] Aaron M. Geller, Emily M. Leiner, Andrea Bellini, et al. “On the Origin of Subsubgiant Stars. I. Demographics”. In: *The Astrophysical Journal* 840.2 (May 2017), p. 66.

[45] Aaron M. Geller, Emily M. Leiner, Sourav Chatterjee, et al. “On the Origin of Subsubgiant Stars. III. Formation Frequencies”. In: *The Astrophysical Journal* 842.1 (June 2017), p. 1.

[46] Aaron M. Geller, Robert D. Mathieu, et al. “WIYN OPEN CLUSTER STUDY. XXXII. STELLAR RADIAL VELOCITIES IN THE OLD OPEN CLUSTER NGC 188”. In: *The Astronomical Journal* 135.6 (May 2008), pp. 2264–2278.

[47] Diego Godoy-Rivera and Julio Chanamé. “On the identification of wide binaries in the Kepler field”. In: *Monthly Notices of the Royal Astronomical Society* 479.4 (Oct. 2018), pp. 4440–4469.

[48] Diego Godoy-Rivera, Marc H. Pinsonneault, et al. “Stellar Rotation in the Gaia Era: Revised Open Clusters Sequences”. In: *e-prints(arXiv:2101.01183)*, arXiv:2101.01183 (Jan. 2021), arXiv:2101.01183.

[49] Daniel Grether et al. “The Metallicity of Stars with Close Companions”. In: *The Astrophysical Journal* 669.2 (Nov. 2007), pp. 1220–1234.

[50] James E. Gunn et al. “The 2.5 m Telescope of the Sloan Digital Sky Survey”. In: *The Astronomical Journal* 131.4 (Apr. 2006), pp. 2332–2359.

[51] Michael R. Hayden et al. “CHEMICAL CARTOGRAPHY WITH APOGEE: METALLICITY DISTRIBUTION FUNCTIONS AND THE CHEMICAL STRUCTURE OF THE MILKY WAY DISK”. In: *The Astrophysical Journal* 808.2 (July 2015), p. 132.

[52] S. Hekker et al. “Precise radial velocities of giant stars”. In: *Astronomy & Astrophysics* 480.1 (Jan. 2008), pp. 215–222.

[53] Jon A. Holtzman, Sten Hasselquist, et al. “APOGEE Data Releases 13 and 14: Data and Analysis”. In: *The Astronomical Journal* 156.3 (Aug. 2018), p. 125.

[54] Jon A. Holtzman, Matthew Shetrone, et al. “ABUNDANCES, STELLAR PARAMETERS, AND SPECTRA FROM THE SDSS-III/APOGEE SURVEY”. In: *The Astronomical Journal* 150.5 (Oct. 2015), p. 148.

[55] T.-O. Husser et al. “A new extensive library of PHOENIX stellar atmospheres and synthetic spectra”. In: *Astronomy & Astrophysics* 553 (Apr. 2013), A6.

[56] I. Iben Jr. et al. “The evolution of low-mass close binaries influenced by the radiation of gravitational waves and by a magnetic stellar wind”. In: *The Astrophysical Journal* 284 (Sept. 1984), p. 719.

[57] Luisa G. Jaime et al. “Habitable zones with stable orbits for planets around binary systems”. In: *Monthly Notices of the Royal Astronomical Society* 443.1 (July 2014), pp. 260–274.

[58] K. A. Janes. “Rotation Periods of Wide Binaries in the Kepler Field”. In: *The Astrophysical Journal* 835.1, 75 (Jan. 2017), p. 75.

[59] T Jayasinghe et al. “The ASAS-SN catalogue of variable stars IX: The spectroscopic properties of Galactic variable stars”. In: *Monthly Notices of the Royal Astronomical Society* 503.1 (Jan. 2021), pp. 200–235.

[60] Adam S Jermyn et al. “Differential rotation in convective envelopes: constraints from eclipsing binaries”. In: *Monthly Notices of the Royal Astronomical Society* 491.1 (Oct. 2020), pp. 690–707.

[61] V. Joergens. “Binary frequency of very young brown dwarfs at separations smaller than 3 AU”. In: *Astronomy & Astrophysics* 492.2 (Oct. 2008), pp. 545–555.

[62] Henrik Jönsson, Jon A. Holtzman, et al. "APOGEE Data and Spectral Analysis from SDSS Data Release 16: Seven Years of Observations Including First Results from APOGEE-South". In: *The Astronomical Journal* 160.3 (Aug. 2020), p. 120.

[63] Henrik Jönsson, Carlos Allende Prieto, et al. "APOGEE Data Releases 13 and 14: Stellar Parameter and Abundance Comparisons with Independent Analyses". In: *The Astronomical Journal* 156.3 (Aug. 2018), p. 126.

[64] A. B. Justesen et al. "The spin-orbit alignment of visual binaries". In: *Astronomy & Astrophysics* 642 (Oct. 2020), A212.

[65] Steven D. Kawaler. "Angular momentum in stars - The Kraft curve revisited". In: *Publications of the Astronomical Society of the Pacific* 99 (Dec. 1987), p. 1322.

[66] Chiaki Kobayashi et al. "Galactic Chemical Evolution: Carbon through Zinc". In: *The Astrophysical Journal* 653.2 (Dec. 2006), pp. 1145–1171.

[67] Marina Kounkel, Kevin Covey, et al. "Close Companions around Young Stars". In: *The Astronomical Journal* 157.5 (Apr. 2019), p. 196.

[68] Marina Kounkel, Kevin R. Covey, et al. "Double-lined spectroscopic binaries in the APOGEE DR16 and DR17 data". In: *preprint(arXiv:2107.10860)* (July 2021).

[69] Robert P. Kraft. "Studies of Stellar Rotation. V. The Dependence of Rotation on Age among Solar-Type Stars". In: *The Astrophysical Journal* 150 (Nov. 1967), p. 551.

[70] Robert P. Kraft. "Studies of Steller Rotation. I. Comparison of Rotational Velocities in the Hyades and Coma Clusters." In: *The Astrophysical Journal* 142 (Aug. 1965), p. 681.

[71] Kaitlin Kratter et al. "Gravitational Instabilities in Circumstellar Disks". In: *Annual Review of Astronomy and Astrophysics* 54.1 (Sept. 2016), pp. 271–311.

[72] Kaitlin M. Kratter and Christopher D. Matzner. "Fragmentation of massive protostellar discs". In: *Monthly Notices of the Royal Astronomical Society* 373.4 (Nov. 2006), pp. 1563–1576.

[73] Kaitlin M. Kratter, Christopher D. Matzner, et al. “ON THE ROLE OF DISKS IN THE FORMATION OF STELLAR SYSTEMS: A NUMERICAL PARAMETER STUDY OF RAPID ACCRETION”. In: *The Astrophysical Journal* 708.2 (Jan. 2010), pp. 1585–1597.

[74] Kaitlin M. Kratter, Ruth A. Murray-Clay, et al. “THE RUNTS OF THE LITTER: WHY PLANETS FORMED THROUGH GRAVITATIONAL INSTABILITY CAN ONLY BE FAILED BINARY STARS”. In: *The Astrophysical Journal* 710.2 (Jan. 2010), pp. 1375–1386.

[75] Pavel Kroupa et al. “The Stellar and Sub-Stellar Initial Mass Function of Simple and Composite Populations”. In: *Planets, Stars and Stellar Systems*. Springer Netherlands, 2013, pp. 115–242.

[76] Charles J. Lada. “Stellar Multiplicity and the Initial Mass Function: Most Stars Are Single”. In: *The Astrophysical Journal* 640.1 (Feb. 2006), pp. L63–L66.

[77] Aaron T. Lee et al. “The Formation and Evolution of Wide-orbit Stellar Multiples In Magnetized Clouds”. In: *The Astrophysical Journal* 887.2 (Dec. 2019), p. 232.

[78] Emily Leiner, Robert D. Mathieu, and Aaron M. Geller. “On the Origin of Subsubgiant Stars. II. Binary Mass Transfer, Envelope Stripping, and Magnetic Activity”. In: *The Astrophysical Journal* 840.2 (May 2017), p. 67.

[79] Emily Leiner, Robert D. Mathieu, Andrew Vanderburg, et al. “Blue Lurkers: Hidden Blue Stragglers on the M67 Main Sequence Identified from Their Kepler/K2 Rotation Periods”. In: *The Astrophysical Journal* 881.1 (Aug. 2019), p. 47.

[80] Chao Liu. “Smoking gun of the dynamical processing of solar-type field binary stars”. In: *Monthly Notices of the Royal Astronomical Society* 490.1 (Nov. 2019), pp. 550–565.

[81] John C. Lurie et al. “Tidal Synchronization and Differential Rotation ofKeplerEclipsing Binaries”. In: *The Astronomical Journal* 154.6 (Nov. 2017), p. 250.

[82] Masahiro N. Machida et al. “Binary formation with different metallicities: dependence on initial conditions”. In: *Monthly Notices of the Royal Astronomical Society* 399.3 (Nov. 2009), pp. 1255–1263.

[83] J Ted Mackereth et al. “Dynamical heating across the Milky Way disc using APOGEE and Gaia”. In: *Monthly Notices of the Royal Astronomical Society* 489.1 (Aug. 2019), pp. 176–195.

[84] J. Ted Mackereth et al. “The age–metallicity structure of the Milky Way disc using APOGEE”. In: *Monthly Notices of the Royal Astronomical Society* 471.3 (July 2017), pp. 3057–3078.

[85] Steven R. Majewski et al. “The Apache Point Observatory Galactic Evolution Experiment (APOGEE)”. In: *The Astronomical Journal* 154.3 (Aug. 2017), p. 94.

[86] Eric E. Mamajek et al. “Improved Age Estimation for Solar-Type Dwarfs Using Activity-Rotation Diagnostics”. In: *The Astrophysical Journal* 687.2 (Nov. 2008), pp. 1264–1293.

[87] Dan Maoz et al. “CHARACTERIZING THE GALACTIC WHITE DWARF BINARY POPULATION WITH SPARSELY SAMPLED RADIAL VELOCITY DATA”. In: *The Astrophysical Journal* 751.2 (May 2012), p. 143.

[88] G. Matijevič et al. “SINGLE-LINED SPECTROSCOPIC BINARY STAR CANDIDATES IN THE RAVE SURVEY”. In: *The Astronomical Journal* 141.6 (May 2011), p. 200.

[89] Sean P. Matt et al. “THE MASS-DEPENDENCE OF ANGULAR MOMENTUM EVOLUTION IN SUN-LIKE STARS”. In: *The Astrophysical Journal* 799.2 (Jan. 2015), p. L23.

[90] T. Mazeh. “Observational Evidence for Tidal Interaction in Close Binary Systems”. In: *EAS Publications Series* 29 (2008), pp. 1–65.

[91] Christine N Mazzola et al. “The Close Binary Fraction as a Function of Stellar Parameters in APOGEE: A Strong Anti-Correlation With α Abundances”. In: *Monthly Notices of the Royal Astronomical Society* (Sept. 2020).

[92] A. Miglio et al. “Age dissection of the Milky Way discs: Red giants in the Kepler field”. In: *Astronomy & Astrophysics* 645 (Jan. 2021), A85.

[93] Maxwell Moe. “Multiplicity statistics and properties across the HR diagram”. In: *Memorie della Societa Astronomica Italiana* 90 (Jan. 2019), p. 347.

[94] Maxwell Moe and Rosanne Di Stefano. "Mind Your Ps and Qs: The Interrelation between Period (P) and Mass-ratio (Q) Distributions of Binary Stars". In: *The Astrophysical Journal Supplement Series* 230.2 (June 2017), p. 15.

[95] Maxwell Moe and Kaitlin M Kratter. "Impact of binary stars on planet statistics – I. Planet occurrence rates and trends with stellar mass". In: *Monthly Notices of the Royal Astronomical Society* 507.3 (Aug. 2021), pp. 3593–3611.

[96] Maxwell Moe and Kaitlin M. Kratter. "Dynamical Formation of Close Binaries during the Pre-main-sequence Phase". In: *The Astrophysical Journal* 854.1 (Feb. 2018), p. 44.

[97] Maxwell Moe, Kaitlin M. Kratter, and Carles Badenes. "The Close Binary Fraction of Solar-type Stars Is Strongly Anticorrelated with Metallicity". In: *The Astrophysical Journal* 875.1 (Apr. 2019), p. 61.

[98] Daniel J. Mortlock et al. "Unbiased Hubble constant estimation from binary neutron star mergers". In: *Physical Review D* 100.10 (Nov. 2019), p. 103523.

[99] Simon J Murphy et al. "Finding binaries from phase modulation of pulsating stars with Kepler: V. Orbital parameters, with eccentricity and mass-ratio distributions of 341 new binaries". In: *Monthly Notices of the Royal Astronomical Society* 474.4 (Dec. 2018), pp. 4322–4346.

[100] M. Ness et al. "SPECTROSCOPIC DETERMINATION OF MASSES (AND IMPLIED AGES) FOR RED GIANTS". In: *The Astrophysical Journal* 823.2 (May 2016), p. 114.

[101] David L. Nidever et al. "THE DATA REDUCTION PIPELINE FOR THE APACHE POINT OBSERVATORY GALACTIC EVOLUTION EXPERIMENT". In: *The Astronomical Journal* 150.6 (Nov. 2015), p. 173.

[102] B. Paczynski. "Evolutionary Processes in Close Binary Systems". In: *Annual Review of Astronomy and Astrophysics* 9.1 (Sept. 1971), pp. 183–208.

[103] Michał Pawlak et al. "The ASAS-SN catalogue of variable stars – IV. Periodic variables in the APOGEE survey". In: *Monthly Notices of the Royal Astronomical Society* 487.4 (June 2019), pp. 5932–5945.

[104] Bill Paxton, Lars Bildsten, et al. “MODULES FOR EXPERIMENTS IN STELLAR ASTROPHYSICS (MESA)”. In: *The Astrophysical Journal Supplement Series* 192.1 (Jan. 2011), p. 3.

[105] Bill Paxton, Matteo Cantiello, et al. “MODULES FOR EXPERIMENTS IN STELLAR ASTROPHYSICS (MESA): PLANETS, OSCILLATIONS, ROTATION, AND MASSIVE STARS”. In: *The Astrophysical Journal Supplement Series* 208.1 (Aug. 2013), p. 4.

[106] Bill Paxton, Pablo Marchant, et al. “MODULES FOR EXPERIMENTS IN STELLAR ASTROPHYSICS (MESA): BINARIES, PULSATIONS, AND EXPLOSIONS”. In: *The Astrophysical Journal Supplement Series* 220.1 (Sept. 2015), p. 15.

[107] Mark J. Pecaut et al. “INTRINSIC COLORS, TEMPERATURES, AND BOLOMETRIC CORRECTIONS OF PRE-MAIN-SEQUENCE STARS”. In: *The Astrophysical Journal Supplement Series* 208.1 (Sept. 2013), p. 9.

[108] M. H. Pinsonneault et al. “Evolutionary models of the rotating sun”. In: *The Astrophysical Journal* 338 (Mar. 1989), p. 424.

[109] Marc H. Pinsonneault et al. “The Second APOKASC Catalog: The Empirical Approach”. In: *The Astrophysical Journal Supplement Series* 239.2 (Dec. 2018), p. 32.

[110] Natalie Price-Jones et al. “The dimensionality of stellar chemical space using spectra from the Apache Point Observatory Galactic Evolution Experiment”. In: *Monthly Notices of the Royal Astronomical Society* 475.1 (Dec. 2017), pp. 1410–1425.

[111] Adrian Price-Whelan et al. “Stellar multiplicity: an interdisciplinary nexus”. In: *Bulletin of the American Astronomical Society* 51.3, 206 (May 2019), p. 206.

[112] Adrian M. Price-Whelan and Jeremy Goodman. “Binary Companions of Evolved Stars in APOGEE DR14: Orbital Circularization”. In: *The Astrophysical Journal* 867.1 (Oct. 2018), p. 5.

[113] Adrian M. Price-Whelan, David W. Hogg, Hans-Walter Rix, Rachael L. Beaton, et al. “Close Binary Companions to APOGEE DR16 Stars: 20,000 Binary-star Systems Across the Color–Magnitude Diagram”. In: *The Astrophysical Journal* 895.1 (May 2020), p. 2.

[114] Adrian M. Price-Whelan, David W. Hogg, Hans-Walter Rix, Nathan De Lee, et al. "Binary Companions of Evolved Stars in APOGEE DR14: Search Method and Catalog of ∼5000 Companions". In: *The Astronomical Journal* 156.1 (June 2018), p. 18.

[115] Roman R. Rafikov. "Can Giant Planets Form by Direct Gravitational Instability?" In: *The Astrophysical Journal* 621.1 (Jan. 2005), pp. L69–L72.

[116] Deepak Raghavan et al. "A SURVEY OF STELLAR FAMILIES: MULTIPLICITY OF SOLAR-TYPE STARS". In: *The Astrophysical Journal Supplement Series* 190.1 (Aug. 2010), pp. 1–42.

[117] Timo Reinhold and Laurent Gizon. "Rotation, differential rotation, and gyrochronology of activeKeplerstars". In: *Astronomy & Astrophysics* 583 (Oct. 2015), A65.

[118] Timo Reinhold, Ansgar Reiners, et al. "Rotation and differential rotation of activeKeplerstars". In: *Astronomy & Astrophysics* 560 (Nov. 2013), A4.

[119] Jennifer L. van Saders et al. "Weakened magnetic braking as the origin of anomalously rapid rotation in old field stars". In: *Nature* 529.7585 (Jan. 2016), pp. 181–184.

[120] H. Sana et al. "Binary Interaction Dominates the Evolution of Massive Stars". In: *Science* 337.6093 (July 2012), pp. 444–446.

[121] Jason L Sanders et al. "Isochrone ages for ∼3 million stars with the second Gaia data release". In: *Monthly Notices of the Royal Astronomical Society* 481.3 (Sept. 2018), pp. 4093–4110.

[122] D. Semenov et al. "Rosseland and Planck mean opacities for protoplanetary discs". In: *Astronomy & Astrophysics* 410.2 (Nov. 2003), pp. 611–621.

[123] Avi Shporer et al. "RADIAL VELOCITY MONITORING OFKEPLERHEARTBEAT STARS". In: *The Astrophysical Journal* 829.1 (Sept. 2016), p. 34.

[124] Gregory V. A. Simonian, Marc H. Pinsonneault, and Donald M. Terndrup. "Rapid Rotation in the Kepler Field: Not a Single Star Phenomenon". In: *The Astrophysical Journal* 871.2 (Jan. 2019), p. 174.

[125] Gregory V. A. Simonian, Marc H. Pinsonneault, Donald M. Terndrup, and Jennifer L. van Saders. "Rapid Rotation of Kepler Field Dwarfs and Subgiants: Spectroscopic v sin i from APOGEE". In: *The Astrophysical Journal* 898.1 (July 2020), p. 76.

[126] A. Skumanich. "Time Scales for CA II Emission Decay, Rotational Braking, and Lithium Depletion". In: *The Astrophysical Journal* 171 (Feb. 1972), p. 565.

[127] David R. Soderblom. "The Ages of Stars". In: *Annual Review of Astronomy and Astrophysics* 48.1 (Aug. 2010), pp. 581–629.

[128] Diogo Souto, Katia Cunha, Verne V. Smith, C. Allende Prieto, Adam Burgasser, et al. "Stellar Characterization of M Dwarfs from the APOGEE Survey: A Calibrator Sample for M-dwarf Metallicities". In: *The Astrophysical Journal* 890.2 (Feb. 2020), p. 133.

[129] Diogo Souto, Katia Cunha, Verne V. Smith, C. Allende Prieto, Kevin Covey, et al. "Detailed Chemical Abundances for a Benchmark Sample of M Dwarfs from the APOGEE Survey". In: *The Astrophysical Journal* 927.1 (Mar. 2022), p. 123.

[130] Meghin E. Spencer et al. "The Binary Fraction of Stars in Dwarf Galaxies: The Case of Leo II". In: *The Astronomical Journal* 153.6 (May 2017), p. 254.

[131] E R Stanway et al. "Binary fraction indicators in resolved stellar populations and supernova-type ratios". In: *Monthly Notices of the Royal Astronomical Society* 497.2 (July 2020), pp. 2201–2212.

[132] John R. Stauffer et al. "The distribution of rotational velocities for low-mass stars in the Pleiades". In: *The Astrophysical Journal* 318 (July 1987), p. 337.

[133] Takuma Suda et al. "Transition of the stellar initial mass function explored using binary population synthesis". In: *Monthly Notices of the Royal Astronomical Society* 432.1 (Apr. 2013), pp. L46–L50.

[134] Kei E. I. Tanaka et al. "Gravitational instability in protostellar discs at low metallicities". In: *Monthly Notices of the Royal Astronomical Society* 439.2 (Feb. 2014), pp. 1884–1896.

[135] Jamie Tayar et al. "RAPID ROTATION OF LOW-MASS RED GIANTS USING APOKASC: A MEASURE OF INTERACTION RATES ON THE POST-MAIN-SEQUENCE". In: *The Astrophysical Journal* 807.1 (July 2015), p. 82.

[136] Yuan-Sen Ting et al. “The Payne: Self-consistent ab initio Fitting of Stellar Spectra”. In: *The Astrophysical Journal* 879.2 (July 2019), p. 69.

[137] Andrei Tokovinin. “Formation of wide binary stars from adjacent cores”. In: *Monthly Notices of the Royal Astronomical Society* 468.3 (Apr. 2017), pp. 3461–3467.

[138] Andrei Tokovinin and Maxwell Moe. “Formation of close binaries by disc fragmentation and migration, and its statistical modelling”. In: *Monthly Notices of the Royal Astronomical Society* 491.4 (Nov. 2020), pp. 5158–5171.

[139] Jennifer L. van Saders et al. “FAST STAR, SLOW STAR; OLD STAR, YOUNG STAR: SUBGIANT ROTATION AS A POPULATION AND STELLAR PHYSICS DIAGNOSTIC”. In: *The Astrophysical Journal* 776.2 (Sept. 2013), p. 67.

[140] Carlos Vera-Ciro et al. “THE EFFECT OF RADIAL MIGRATION ON GALACTIC DISKS”. In: *The Astrophysical Journal* 794.2 (Oct. 2014), p. 173.

[141] F. Verbunt et al. “Tidal circularization and the eccentricity of binaries containing giant stars”. In: *Astronomy & Astrophysics* 296 (1995), p. 709.

[142] S. N. Vogel et al. “Rotational velocities of pre-main-sequence stars”. In: *The Astrophysical Journal* 245 (May 1981), p. 960.

[143] David H. Weinberg et al. “Chemical Cartography with APOGEE: Multi-element Abundance Ratios”. In: *The Astrophysical Journal* 874.1 (Mar. 2019), p. 102.

[144] J. C. Wilson et al. “The Apache Point Observatory Galactic Evolution Experiment (APOGEE) Spectrographs”. In: *Publications of the Astronomical Society of the Pacific* 131.999 (Mar. 2019), p. 055001.

[145] Jennifer G. Winters et al. “The Solar Neighborhood. XLV. The Stellar Multiplicity Rate of M Dwarfs Within 25 pc”. In: *The Astronomical Journal* 157.6 (May 2019), p. 216.

[146] Sidney C. Wolff et al. “Activity in F stars”. In: *The Astrophysical Journal* 310 (Nov. 1986), p. 360.

[147] Haibo Yuan et al. “STELLAR LOCI II. A MODEL-FREE ESTIMATE OF THE BINARY FRACTION FOR FIELD FGK STARS”. In: *The Astrophysical Journal* 799.2 (Jan. 2015), p. 135.

[148] J.-P. Zahn. “Tidal dissipation in binary systems”. In: *EAS Publications Series* 29 (2008), pp. 67–90.

[149] G. Zasowski, R. E. Cohen, et al. “Target Selection for the SDSS-IV APOGEE-2 Survey”. In: *The Astronomical Journal* 154.5 (Oct. 2017), p. 198.

[150] G. Zasowski, Jennifer A. Johnson, et al. “TARGET SELECTION FOR THE APACHE POINT OBSERVATORY GALACTIC EVOLUTION EXPERIMENT (APOGEE)”. In: *The Astronomical Journal* 146.4 (Aug. 2013), p. 81.